THESIS FOR THE DEGREE OF DOCTOR OF PHILOSOPHY

# Mesoporous Materials for Fast Charging Electrochemical Energy Storage

GIULIO CALCAGNO

Department of Chemistry and Chemical Engineering

CHALMERS UNIVERSITY OF TECHNOLOGY

Gothenburg, Sweden 2020



i

**Mesoporous Materials for Fast Charging Electrochemical Energy Storage**

GIULIO CALCAGNO
ISBN 978-91-7905-378-9

Department of Chemistry and Chemical Engineering
Chalmers University of Technology
SE-412 96 Gothenburg
Sweden
Telephone + 46 (0)31-772 1000

Cover: Mesoporous Carbon and Mesoporous Anatase Beads as active materials for fast charging electrochemical energy storage

# Mesoporous Materials for Fast Charging Electrochemical Energy Storage

GIULIO CALCAGNO
Department of Chemistry and Chemical Engineering
CHALMERS UNIVERSITY OF TECHNOLOGY

## Abstract

High performing electrochemical energy storage (EES) devices are needed to cope with the increasing energy requirements of modern society. Electrode materials must store lots of energy, charge/discharge fast and be environmentally friendly. The present thesis discusses the advantages of using nanostructured porous materials as electrodes for fast-charging energy storage. High specific surface areas and short diffusion paths make this class of materials competitive for future EES applications. Structural, morphological and electrochemical characterizations were used to study the materials and their charge/discharge behaviours on both a fundamental and device level. Mesoporous titanium dioxide of different polymorphs can reversibly insert $Li^+$ ions inside its structure. Ordered amorphous mesoporous titanium dioxide, produced by low temperature spray deposition, showed a quasi-linear voltage - capacity profile in organic electrolytes, suggesting a pseudocapacitive behaviour of insertion type. A high initial capacity loss is associated with the irreversible formation of lithium rich phases at the surface of the material. On the other hand, mesoporous anatase beads, produced via a solvothermal approach, were characterized by extended plateaus in the voltage profile, a typical feature for a faradaic insertion mechanism. However, the anatase beads electrodes also showed high pseudocapacitive contributions and delivered higher capacities and rate performance compared with the mesoporous amorphous titanium oxide material. By doping the mesoporous beads with different niobium concentrations, the semiconducting anatase acquired a metallic-like conductivity. High concentration of doping negatively affected the lithium insertion process, while a low level of niobium doping was beneficial for improving the rate performance of mesoporous anatase beads electrodes. The anatase material showed initial irreversible capacities in organic electrolytes based on carbonates. Limiting the potential window was found to be a suitable strategy to avoid parasitic reactions, although this limits the amount of storable energy. Moreover, by using an ionic liquid as electrolyte, the electrode/electrolyte interface can be stabilized, limiting the capacity fading. Finally, the mesoporous anatase beads were studied in a hybrid configuration against a porous carbon electrode, delivering very stable performance over 10000 cycles. Ordered mesoporous carbons of the CMK-8 type also showed interesting performance for different EES systems. When doped with nitrogen, CMK-8 carbons were able to store high amounts of lithium ions, both at low and fast rates of charging. In addition, CMK-8 carbons were used in hybrid supercapacitors as conductive electrodes to support surface redox reactions of active molecules added in water-based electrolytes. A pentyl viologen/bromide redox-active pair was studied on CMK-8 carbon electrodes at different operating voltages. By detailed studies of the electrochemistry of the system, high and stable energy and power densities were achieved.

# List of Publications

I. **Electrochemical and Structural Characterization of Lithiation in Spray Deposited Ordered Mesoporous Titania as an Anode for Li ion Batteries**.
Gunnar Símonarson, Giulio Calcagno, Antiope Lotsari, Anders E.C. Palmqvist
*RSC Advances 2020, 10 (34), 20279–20287*

II. **Fast Charging Negative Electrodes Based on Anatase Titanium Dioxide Beads for Highly Stable Li-Ion Capacitors.**
Giulio Calcagno, Antiope Lotsari, Alan Dang, Simon Lindberg, Anders E.C. Palmqvist, Aleksandar Matic and Carmen Cavallo
*Materials Today Energy 2020, 16, 100424*

III. **Effect of the Niobium Doping Concentration on the Charge Storage Mechanism of Mesoporous Anatase Beads as Anode for Fast Rechargeable Li-ion Batteries.**
Carmen Cavallo, Giulio Calcagno, Rodrigo P. Carvalho, Matthew J. Sadd, Bruno Gonano, C. Moyses Araujo, Anders E.C. Palmqvist and Aleksandar Matic
*Manuscript - submitted for publication in ACS Applied Energy Materials*

IV. **Electrochemical Behaviour of Nb-Doped Anatase TiO2 Microbeads in an Ionic Liquid Electrolyte.**
Simon Lindberg, Carmen Cavallo, Giulio Calcagno, Adriana M. Navarro-Suárez, Patrik Johansson and Aleksandar Matic
*Batteries & Supercaps, First published in June 2020, Early View*

V. **Effect of Nitrogen Doping on the Performance of Mesoporous CMK-8 Carbon Anodes for Li-ion Batteries**
Giulio Calcagno, Marco Agostini, Shizhao Xiong, Aleksandar Matic, Anders E.C. Palmqvist, Carmen Cavallo
*Energies 2020, 13 (19), 4998*

VI. **Mechanistic Study of Aqueous Pentyl Viologen/Bromide Redox-Enhanced Electrochemical Capacitors Based on Mesoporous Carbons**
Giulio Calcagno, Brian Evanko, Galen D. Stucky, Elisabet Ahlberg, Seung Joon Yoo and Anders E.C. Palmqvist
*Manuscript*

# Contribution Report to the Listed Publications

I.      Lead author together with G.S. Performed all the electrochemical measurements and jointly the SAXS measurements. Jointly analysed the results and wrote the manuscript.

II.     Lead author together with C.C. Jointly synthesized the material, conducted the structural and morphological characterization, except the TEM analysis. Designed and performed most of the electrochemical measurements. Jointly analysed the results and wrote the manuscript.

III.    Lead author together with C.C. Jointly synthesized the material, conducted the structural and morphological characterization, except for the Raman spectroscopy and TEM analysis. Designed and performed most of the electrochemical measurements. Jointly analysed the results and wrote the manuscript.

IV.     Participated in the synthesis and the structural characterization of the material. Participated in analysing the results and writing the manuscript.

V.      Lead author together with C.C. Performed most of the experimental work except for the XPS analysis. Jointly analysed the results and wrote the manuscript.

VI.     Lead author. Performed all the experimental work. Jointly analysed the results and wrote the manuscript.

# Table of Contents

# 1.    Introduction and Motivation

Societal energy needs are growing at a fast rate, together with the intensive use of resources and the anthropological influence on Earth´s environment. There is no more scientific doubt that we must rethink our way of using energy and strive for a sustainable development.[1] Energy from renewable resources should sooner or later become the dominant contribution to the global energy mix. In this context, energy storage technologies are needed to provide stable renewable energy supply and firmer capacity during peak demand periods, improving the overall energy efficiency.[2] Energy storage is also necessary for applications like portable electronics and electric vehicles. In recent years, an increased interest in the large market of electrification has arisen, foreseeing a huge challenge for the electrochemical energy storage (EES) development.[3]

Chapter 2 provides a background on the EES systems covered in this work. Among them, Li-ion batteries (LiBs) have attracted worldwide attention, and a Nobel Prize, due to their immense impact on our society.[4] They can be used in a wide range of applications, both for portable devices and at a grid-scale. The relatively high gravimetric energy density (commercially between 150 to 300 Wh kg$^{-1}$) is obtained by the intercalation/insertion of Li$^+$ ions in their electrodes. Unfortunately, it is challenging to use them for applications requiring high power densities, due to their slow chemical processes, also called faradaic processes.[5] Conversely, supercapacitors (SCs) are devices capable of high-power delivery, great stability and lower energy density, with commercial devices providing ~5 Wh kg$^{-1}$. The energy storage process is based on the physical separation of charges at the surface of porous electrodes, forming an electrical double layer (EDL). To distinguish the storage mechanisms of these two systems, we talk about intercalation/insertion capacity for LiBs, while the term capacitance is used for SCs.[6] Recently, devices addressing performances in between the two have emerged. One example is the hybrid asymmetric supercapacitor (HASC) configuration, which combines battery and supercapacitor electrodes in tandem. In this class, Li-ion HASCs aim at achieving both high power and high energy densities by using a porous EDL material as positive electrode coupled with a Li ion intercalation material as negative electrode.[7]

Innovation at the material level is one of the necessary technological challenges for EES devices.[8] A compromise between cost, availability and performance must always be met. The choice of proper electrode materials might start from the abundance of the elements. Nickel and cobalt are at risk of shortage and possible cause of geopolitical issues, so alternatives should be considered. For example, research has focused on more abundant elements like carbon, titanium, iron and manganese. The processing of the raw material resources and the synthesis of the final material can also be very energy intensive. Greener chemistry using low temperatures and non-toxic compounds, should be favoured.[8]
Along with sustainability issues, new electrode materials must provide higher energy and power densities than commercial ones. Nanomaterials chemistry can provide a solution by developing materials with enhanced performance compared with their bulk counterparts.[9] Mesoporous nanostructured materials are particularly interesting because of their high surface area, offering a high number of active redox sites and good accommodation of strain.[10] According to IUPAC definition, mesoporous materials are porous materials with pore dimensions between 2 – 50 nm. Among this class, ordered mesoporous materials are characterized by an ordered network of pores acting as pathways for fast ion diffusion.[11]

The overall aim of this work was to study the charge storage mechanisms and the effect of structure/morphology on the electrochemical performance of mesoporous titanium dioxide and ordered mesoporous carbon materials, synthesized in our labs, for lithium ion storage and hybrid supercapacitors applications. Several structural, morphological and electrochemical techniques were used, and are shortly described in Chapter 3.

Chapter 4 is focused on the research conducted on mesoporous titanium dioxide of two different polymorphs as active material for Li-ion storage. Titanium oxide is a promising material candidate for EES devices because it is very abundant in Earth´s crust, it is chemically stable, characterized by low toxicity and its production has typically a low cost. However, the diffusion of $Li^+$ ions into bulk titanium dioxide is slow, limiting its applicability.[12] Nanostructuring $TiO_2$ can provide a higher surface to volume ratio and improve its kinetics. In addition, it has been demonstrated that nanosizing transition metal oxides with layered structure, like titanium oxide, can give rise to an extrinsic insertion pseudocapacitance.[13] The term pseudo- means "not actually but having the appearance of" and refers to fast charge transfer faradaic reactions proceeding at the surface of some materials, like ruthenium oxide, with an electrochemical signature similar to an electric double layer capacitance. The extrinsic insertion pseudocapacitance is shown when the material size is reduced to the nanometer level and the $Li^+$ ion insertion proceeds at the surface via fast charge - discharge kinetics.[14]

In the results discussion, paragraph 4.3, it will be shown that the mesoporous titanium oxide materials, synthesized via low temperature processes and characterized by high active surface areas, possess an interesting set of properties to be used for high power electrodes in future storage applications. The effect of niobium doping and the use of different electrolytes will be also addressed.

In Chapter 5 the charge storage mechanisms of ordered mesoporous carbons, synthesized by a templating method, are presented. Carbon materials have been extensively used in EES devices due to their low cost, high abundance, environmental friendliness, non-toxicity and relatively high electronic conductivity. Graphite is the material used in the anodes of LiBs, while activated porous carbon is the most used electrode material for electrochemical capacitors. Ordered mesoporous carbons (OMC) have gained interest due to their high active surface areas, large pore volumes, narrow pore size distribution and 3D network of ordered interconnections.[10] These materials are amorphous, versatile and conductive. OMCs intercalate $Li^+$ ions in between the graphitic layers of their structure, similarly to graphite. On the other hand, their large and conductive surface area can store charges in form of a double layer. Paragraph 5.3 presents the results and discussion regarding the effect of nitrogen doping on the performance of carbons when intercalating $Li^+$ ions. OMCs were also used as conductive supports to study the electrochemistry in aqueous solution of an added redox pair based on pentyl viologen and sodium bromide. A combination of fundamental and applied investigations is proven necessary to deeply understand the system and improve the final device performance.

## 2.    A Background to Batteries and Supercapacitors

### 2.1    Electrochemical Energy Storage

Devices for electrochemical energy storage and conversion include batteries, fuel cells, and supercapacitors.[2] Although the energy-providing processes take place at the electrode-electrolyte interface in all three systems, they are governed by different mechanisms and show different performance. In Figure 1 a Ragone plot is used to compare the three different systems in terms of energy density and power density. The sloping lines on the plot indicate the relative time taken to discharge the device.
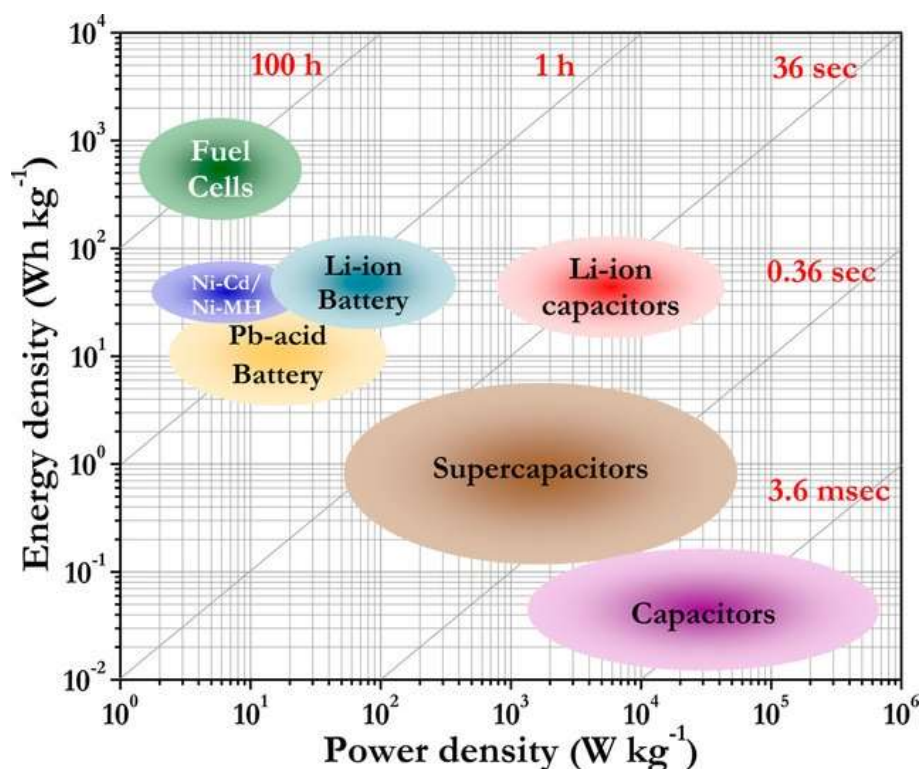


*Figure 1*: *Qualitative Ragone plot presenting the different energy storage and conversion systems in terms of performance areas and representative times for discharging. Reproduced with permission from*[7].

Fuel cells are promising devices for green energy conversion, because, in their cleanest form, they use hydrogen as energy source and are characterized by high energy densities. This thesis will, however, not cover these devices.

### 2.2    Batteries

Batteries have been in use for over two centuries, dating back to 1800 and Alessandro Volta in Como, Italy. There are three general classes: primary batteries that are discharged once and discarded; secondary rechargeable batteries that can be discharged and then restored to their original condition by reversing the current flow through the cell; and specialty batteries

that are designed to fulfil a specific purpose. Simply stated, a battery is composed of two electrodes, an electrolyte, a separator and current collectors. Electricity is generated by conversion of chemical energy via redox reactions at the anode and cathode electrodes. As the reaction at the anode usually takes place at lower electrode potentials than at the cathode, the terms negative and positive electrode are used. The negative electrode is a good reducing agent (electron donor) such as lithium, zinc or lead. The positive electrode is an electron acceptor such as lithium cobalt oxide, manganese dioxide, or lead oxide. The electrolyte is a pure ionic conductor that physically separates the anode from the cathode. The specific capacity of a battery, expressed in the following in mAh g$^{-1}$, is the total amount of electrical charge Q that can be drawn from the device before a specified cut-off voltage V is reached; the specific energy, expressed in mWh g$^{-1}$ or Wh kg$^{-1}$, is used to assess the energy content of the system, whereas the specific power, expressed in mW g$^{-1}$ or W kg$^{-1}$, is used to assess the rate capability of discharged energy.[15]

## 2.2.1 Li-ion Batteries

In the field of secondary batteries, lithium has long received much attention as an interesting anode material, due to its low electronegativity, lowest standard potential $E^0$ = -3.04 V *vs.* standard hydrogen electrode and light weight.[16] In 1970s Whittingham proposed the idea of rechargeable lithium batteries and developed a prototype that used a lithium-metal as anode.[17] The battery had a high energy density and the diffusion of lithium ions into the cathode was reversible, making the battery rechargeable. However, needle-like lithium crystals, called dendrites, grow on the anode upon cycling, leading to short-circuits and fires. In the late 1970s and early 1980s, Goodenough developed rechargeable batteries with cathodes made from layered oxides capable of storing lithium ions.[18] This greatly improved the energy density, and lithium cobalt oxide remains one of the most used cathode materials for commercially available lithium-ion batteries (LiBs). The breakthrough in the 1980s, which lead to the lithium-ion battery concept, was made by Yoshino who exploited an old concept of using carbonaceous materials as anode intercalation host.[19] In the charged state, lithium is now in ionic form, intercalated into graphite and not forming dendrites. For their discoveries and the fundamental contribution to the development of lithium ion batteries, the three scientists have been awarded the Nobel Prize for Chemistry in 2019.[4] Later, Dahn and co-workers published their report on the principle of lithium intercalation in graphitic anodes and the formation of a protective film due to electrolyte decomposition. They adopted a model developed earlier by Peled to describe the passivation on lithium metal and named this surface film on carbonaceous anodes as "solid electrolyte interface" (SEI).[20] It has been generally agreed that the electrolyte reduction products are the main components of an SEI and dictate the chemical as well as thermal properties of the electrode.[21] Graphite is a cheap and stable negative electrode material, but its specific capacity is not so high, with a theoretical limit of 372 mAh g$^{-1}$. Furthermore, the insertion of Li$^+$ ions inside the graphite structure is diffusion-limited and consequently relatively slow.[22] To improve the energy density and the cycling rate capability, many alternatives to graphite, like silicon, tin, germanium and transition metal oxides have been extensively explored in the past 20 years.[23–25] In general, the next-generation anodes and cathodes require: i) to effectively and reversibly host Li-ions providing high capacity, ii) having good electronic and ionic conductivity, iii) allowing for fast kinetics, and iv) showing high mechanical stability upon volume change during cycling. Research and engineering are also focused on developing

better binders, separators and current collectors. [26] Figure 2 reports a schematic depiction of a Li-ion battery.

Nowadays, the best performing Li-ion batteries in the market delivers ~300 Wh kg$^{-1}$. A recent report from EUCAR, the European Council for Automotive R&D, identifies the energy density goal of next-generation batteries for electric car to 450 Wh kg$^{-1}$, to be reached by 2030.[27] In terms of power density, LiBs dominate the field of applications requiring more than 15 min charging/discharging time.
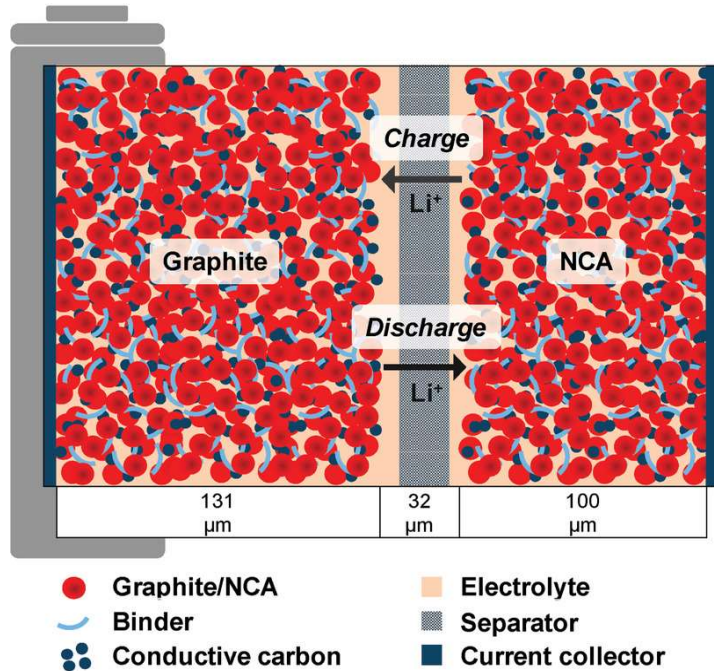


*Figure 2*: *Schematic depiction of a typical 18650-type cell for a LiB system with an NCA cathode (LiNi$_{0.8}$Co$_{0.15}$Al$_{0.05}$O$_2$), a graphite anode, and an organic carbonate solvent-based electrolyte (LiPF$_6$ in 1 : 1 ethyl-carbonate (EC): dimethyl-carbonate (DMC). Reproduced with permission from*[28].

## 2.3 Supercapacitors

The phenomenon of storing an electrical charge on surfaces was discovered when rubbing a cloth on amber or other glassy materials in ancient times. The principle that electrical energy can be stored between two metallic plates, separated by an insulator, is known since the late 18$^{th}$ century. A device able to store electricity in this way is called capacitor and it stores an energy $G = \frac{1}{2}CV^2$, with G being the Gibbs free energy and C the capacitance (expressed in Farad, F), due to a voltage difference V between two plates accommodating charge +q and -q. An electrochemical capacitor is composed of two electrodes and an electrolyte that works as an insulator. At the surface of the two electrodes, one of which is charged negatively with respect to the other, charge separation and storage occur. Historically, the electrochemical capacitors were called supercapacitors (SC) to differentiate them from capacitors, because of the much higher capacitance they were able to store. There

are two main classes of supercapacitors: electric double-layer capacitors (EDLC) and pseudocapacitors (PSCs).[29]

### 2.3.1 Electric Double Layer Capacitors (EDLC)

EDLCs are the most common and commercially available supercapacitors, therefore many reviews on EDLCs and materials can be found in literature.[30] The charge is stored through a physical process of adsorption of ions at the interface between electrodes and electrolyte, forming a double layer of charges, as depicted in Figure 3. The accepted theoretical model of the electric double layer is based on the works of Helmholtz, Gouy and Chapman, Stern and Grahame.[31–33] The model describes the double layer as composed of a diffuse layer, towards the solution, and a compact layer, next to the surface, where partial desolvation of ions occurs. The electrode materials in an EDLC possess a very high surface area, as the specific capacitance is directly proportional to the accessible surface area. Typically, the electrodes are made of carbon-based materials with high porosity and broad pore size distribution.[34] The commercially available supercapacitors usually comprise two electrodes both made of activated carbons and are defined symmetric for this reason. Electrolytes can be aqueous, with operating voltages limited by water decomposition, organic, the most common being acetonitrile, and more recently ionic liquids.[35] Recent findings have claimed the importance of micro-porosity (less than 2 nm in diameter according to IUPAC) to achieve high specific capacitance, which is why carbon nanomaterials of different form have been extensively studied.[36] Typical devices can store energy in the range of 5 Wh kg$^{-1}$ and reach powers of several kW kg$^{-1}$. EDLCs dominate the applications requiring a charging/discharging time in the time scale of seconds.
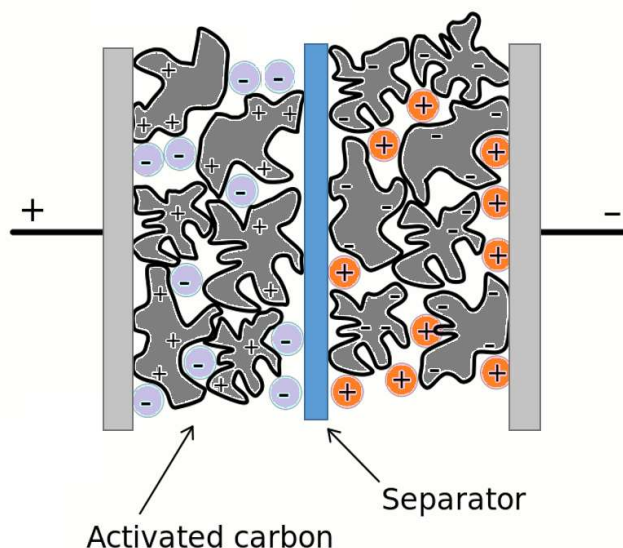


***Figure 3***: *Schematic depiction of a typical symmetric supercapacitor and the formation of an electric double layer of charges at the interface between electrolyte (containing the ions) and electrodes' surface. The separator avoids direct contact between the two electrodes.*

## 2.3.2 Pseudocapacitors

Pseudocapacitors (PSCs) represent the second class of supercapacitors. Pseudocapacitance refers to fast faradaic charge transfer reactions happening at the surface of some materials, like ruthenium oxide, with an electrochemical signature similar to a capacitance.

In his influential book on electrochemical capacitors, Conway stated: "Pseudocapacitance… is faradaic in origin, involving the passage of charge across the double layer, as in battery charging and discharging, but capacitance arises in account of the special relation that can originate for thermodynamic reasons between the extent of charge acceptance $\Delta q$ and the change in potential $\Delta V$, so that the derivative $d(\Delta q)/d(\Delta V)$, which is equivalent to a capacitance, can be formulated and experimentally measured by dc, ac or transient techniques".[29] To summarize, fast redox reactions exhibiting a linear dependence of the charge stored with the width of the potential window. Moreover, the pseudocapacitive mechanisms exhibit kinetic electrochemical signatures indicative of high reversibility, like a mirror image cyclic voltammogram, holding the promise of achieving battery level energy density with high efficiency.[13] The main drawback is that typical pseudocapacitive materials show poor long-term cycling stability.

Several are the electrode materials used in PSCs but two main classes can be defined: metal oxides and conducting polymers. Metal oxides like $RuO_2$, $MnO_2$, $V_2O_5$ and $Nb_2O_5$ have been extensively studied.[37–40] $RuO_2$ is a good performing material, but has a very high cost, while $MnO_2$ and $V_2O_5$ suffer from poor conductivity and/or cycling stability. $Nb_2O_5$ has recently shown promising performance and good stability, especially when used in combination with a carbon matrix. Conductive polymers, like polyaniline and polythiophene, generate capacitance by redox reactions.[41,42] Because of swelling and shrinking during cycling, the polymers suffer from low cycling stability.

Pseudocapacitance can also occur when nanosizing transition metal oxides with layered crystalline structure giving rise to another phenomenon, called intercalation pseudocapacitance.[43,44] Intercalation/insertion pseudocapacitance occurs when ions intercalate/insert into the layers or tunnels of the transition metal oxide and undergo charge transfer and change of metal valance, with no or limited crystallographic change. Limited phase change means that just a very small volume modification happens between the charged and discharged state. Being a surface limited process, the intercalation/insertion pseudocapacitance is very interesting for high rate capability applications, thanks to fast ion transport kinetics and long stability. The fast surface kinetics is the main characteristic differentiating this phenomenon with diffusion-limited battery intercalation. However, the distinction between the two phenomena is still blurred. Besides, two types of pseudocapacitive mechanism have been discovered: intrinsic pseudocapacitance, which is an inherent property of the material, so it is displayed in a wide range of particle sizes and morphologies, and extrinsic pseudocapacitance, which emerges when the material is nano-engineered and the surface/volume ratio is increased. Nanostructured $TiO_2$, $LiCoO_2$ and $Li_4Ti_5O_{12}$ are very good examples showing this phenomenon.[45,46]

## 2.4 Hybrid Systems

In recent years, new applications requiring performance in between Li-ion batteries and supercapacitors have arisen. These intermediate devices need to store tens of Wh kg$^{-1}$ with discharging time between several seconds up to 30 minutes. One way to address this

challenge is by combining the mechanisms of faradaic, pseudocapacitive and capacitive storage. In the literature different terminology has been used to define a series of devices characterized by combined storage mechanisms. In this thesis, the term "hybrid" will be used to describe the class of all these devices. Examples of hybrid supercapacitors are asymmetric supercapacitors, like Li-ion capacitors, and redox enhanced EDLCs, which contain additives in the electrolyte that undergo surface redox reactions on the carbon electrode surface.[47,48] Asymmetric supercapacitors use different positive and negative electrodes, typically one battery-type and one supercapacitor-type. The use of two different electrode materials can extend their operating voltage window by "slowing down" the hydrogen evolution and oxygen evolution reactions, depending on the catalytic activity of the electrode. For aqueous-based systems, separating the two electrodes and exposing them to different pH conditions allowed an operating voltage larger than 2.0 V.[49] The extension of the operating voltage can substantially increase the specific energy, which is proportional to the square of the voltage. It is also important to note that to guarantee a charge balance during operation and optimal performance, the mass ratio of the two electrodes should be adjusted, by considering the two different storage mechanisms. In addition, when evaluating the performance of these systems, it is important to state clearly which component is included in the calculation of the values of energy and power density. Energy densities expressed as a function of the active material are misleading and far from the device performance.[28,50]

## 2.4.1  Li-ion Capacitors

Among the different types of asymmetric supercapacitors, Li-ion HASCs have received a lot of attention. They consist of a Li-ion intercalation negative electrode coupled with an EDLC carbon electrode, both immersed in a non-aqueous Li-containing electrolyte.[51,52] The first prototype of this device was reported by Amatucci et al. in 2001, and it combined an activated carbon electrode with a lithium titanate electrode (nowadays used for power batteries as replacement of graphite) both immersed in LP30 (1 M $LiPF_6$ in EC:DMC) standard Li-ion battery electrolyte.[53] In **Paper II**, we present a slightly different version of this configuration, where the battery electrode store charge via a pseudocapacitance of insertion type mechanism. This type of Li-ion HASC is very promising because it combines the increase in specific energy of a hybrid device with the high rate capability of pseudocapacitance. Figure 4 illustrates a representative scheme of a symmetric supercapacitor, a Li-ion battery and a Li-ion HASC, which is a direct combination of the first two devices.
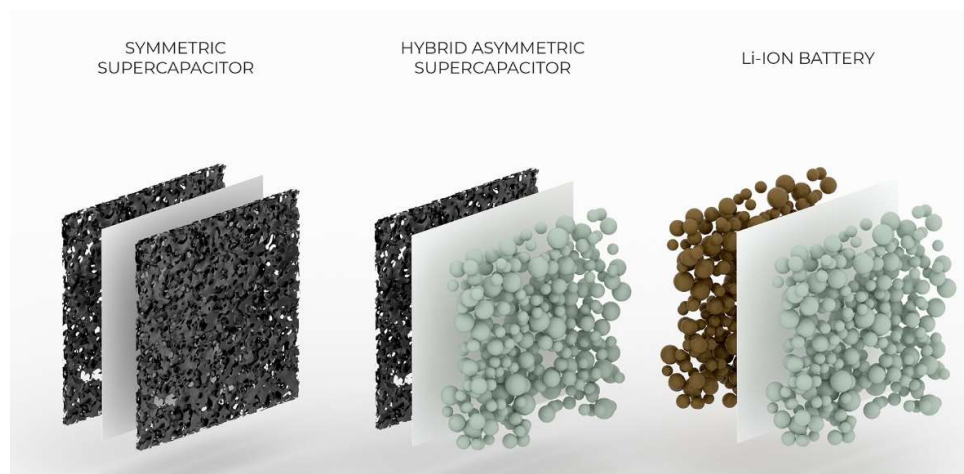
*Figure 4: From left to right: Symmetric Supercapacitor (SC), Hybrid Asymmetric Supercapacitor (HASC) and Li-ion Battery.*

### 2.4.2 Redox-enhanced Electrochemical Capacitors

Redox enhanced electrochemical capacitors (ECs) extend the concept of hybridization beyond the electrode/electrolyte interface by providing increased charge storage through the redox activity of the electrolyte.[48,54] The most studied design of these systems is similar to a symmetric EDLC with large-surface porous carbon electrodes, with the addition of redox-active molecules in the electrolyte.[55] The electrolyte can be aqueous or non-aqueous, however devices with water-based electrolytes have received most of the attention thanks to their higher safety and environmental friendliness.[56] Different redox species have been reported for this application, with notable examples being halide ions ($I^-$ and $Br^-$), small organic molecules like methylene blue, viologens, quinones and transition metal salts of Fe, Cu and Sn.[57–61] Depending on the state of charge of the redox ions, the systems can be classified as cationic, anionic or neutral.[62] Figure 5 depicts the energy storage mechanism in a redox enhanced EC during charge and discharge.

An important aspect in the design of redox enhanced ECs is the charge balance between positive and negative electrodes. To deal with this issue, dual redox systems have been explored.[63–65] The redox couple must be chosen so that one species undergoes the oxidation reaction in unison with the reduction of the other. In addition, to maximize the storable charge and the operating voltage, thereby the specific energy, the redox potentials must be carefully matched, considering also the influence of the pH on the onset of the hydrogen evolution (HE) and oxygen evolution (OE) reactions. Finally, the couple must be highly soluble to effectively increase the specific capacity, the kinetics should be fast and the self-discharge process needs to be minimized.[54]

Internal self-discharge is a major limiting factor, which develops from the cross-diffusion of the redox species.[66] The most commonly adopted solution is to use anion/cation-selective membranes, even though those membranes can be expensive and limit the practical application of the final devices. Another solution capitalizes on the confinement of the redox species inside the meso/micro-pores of activated carbon electrodes.[67–70]

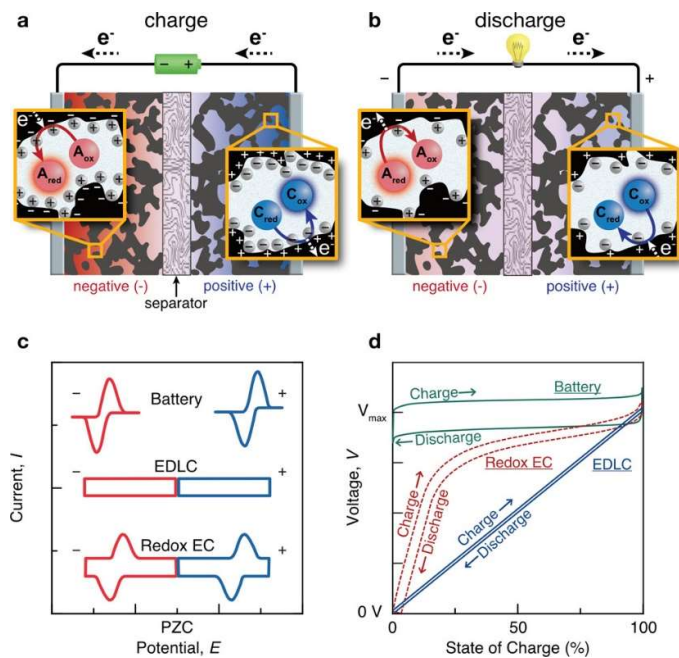**Figure 5**: *Charge (a) and discharge (b) storage mechanisms in redox enhanced electrochemical capacitors. Electrochemical signatures (c) and voltage profiles (d) for EDLC, Battery and Redox EC devices. Reprinted with permission from* [48].

# 3.  Analytical methods

## 3.1  Structural Characterization

The structural characterization of the materials was performed through scanning electron microscopy (SEM), transmission electron microscopy (TEM), X-ray absorption spectroscopy (XAS), X-ray diffraction (XRD) and nitrogen sorption (BET and BJH).

### 3.1.1  Scanning Electron Microscopy (SEM)

SEM is a non-destructive microscopy technique operated in ultra-high vacuum. The sample is scanned by an electron beam generated thermo-ionically by an electron gun. The irradiated sample emits secondary and back scattered electrons, which provide information about the surface topography and the surface composition, respectively. The SEM used in this work is a Jeol JSM 7800F Prime. In **Paper II**, SEM was used to study the morphology of mesoporous anatase $TiO_2$ beads and the surface of electrodes pre and post cycling. In **Paper III** and **IV**, the technique was used to evaluate the effect of different niobium doping on the morphology of mesoporous titania beads. In **Paper V**, micrographs of an electrode composed of nitrogen doped ordered mesoporous carbon are shown in the Appendix.

### 3.1.2  Transmission Electron Microscopy (TEM)

TEM is also a non-destructive microscopy technique. The electron beam, at high accelerating voltages, interacts with the sample and passes through it, forming a projection of the structural features on a detector placed underneath. Being a transmission technique, it requires very thin samples, with thicknesses in the order of 50 to 100 nm. Bright-field (BR) and high-resolution (HR) TEM was used in this work. To obtain compositional maps of the samples, energy-filtered (EF) experiments can be performed. In **Paper I**, TEM samples were prepared by a TEM lamella lift-out technique in a FIB/SEM. The lamella was attached to a copper half grid and was ion thinned to transparency in the FIB/SEM. The TEM observations were performed on a FEI Tecnai G2 operating at 200 kV and on a FEI Titan operating at 300 kV. Energy filtered EFTEM experiments were performed on the Titan. In **Paper II**, the TEM samples were prepared by scratching the electrode surface, disperse it in absolute ethanol and one drop placed on a lacey carbon Cu TEM grid. The FEI Tecnai was used for these experiments.

### 3.1.3  X-ray Powder Diffraction (XRD)

X-ray diffraction is the most used technique to study crystalline materials. When a crystalline material is irradiated with a monochromatic X-ray beam of wavelength $\lambda$, part of the X-rays will be diffracted following Bragg´s law: $n\lambda = 2d\sin\vartheta$, where d is the distance between the crystalline planes and $2\vartheta$ is the angle between the incoming and the outgoing beams. The resulting diffraction pattern, characterized by the so-called Bragg peaks, is specific for a crystal structure.

In **Paper II** and **IV**, the crystallinity of the mesoporous anatase beads was studied with powder X-ray diffraction (XRD) and an X'Pert Pro diffractometer (Cu K$\alpha$ radiation, $\lambda =$

0.154184 nm) equipped with an X'Celerator ultrafast RTMS detector. The angular range was 10-90° (in 2ϑ) and the angular resolution (in 2ϑ) was 0.001°. A 0.04 rad soller slit, a 1° divergence slit, and a 20 mm mask were used on the incident beam path, while a 6.6 mm anti-scatter slit and a 0.04 rad collimator were used on the diffracted beam path. By using the MAUD software package, Rietveld analysis of the obtained patterns was performed.[71] In **Paper III**, XRD measurements were performed on a D8-Advanced Bruker AXS diffractometer in the scanning range of 10-80°, using CuKα1 radiation having a wavelength of 0.15406 nm. The angular range covered was 10-90° (2ϑ) and the angular resolution was 0.001°. A 0.04 rad Soller slit, a 1° divergence slit, and a 20 mm mask were used on the incident beam path, while a 6.6 mm anti-scatter slit and a 0.04 rad collimator were used on the diffracted beam path. In **Paper V**, the crystallinity of ordered mesoporous carbons was similarly investigated with the D8-Advance Bruker.

### 3.1.4   X-ray Absorption Spectroscopy (XAS)

When a sample is exposed to X-ray radiation, the electric field of the radiation will interact with the bound electrons of the material. At specific energies, this interaction will be of absorption type and result in a photoexcitation process. By studying the energy of the ejected photoelectrons, X-ray absorption spectroscopy is used for determining the local geometric and/or electronic structure of matter. It is specifically useful to study amorphous materials, which cannot easily be studied via diffractive techniques. In **Paper I**, X-ray absorption measurements on pristine, cycled and reference samples were performed at the Balder XAS beamline of the MAX IV synchrotron in Lund, Sweden.[72] The measurements were carried out in transmission mode and titanium foil was used as a reference for energy calibration of the spectra.

XAS measurements were performed on electrode samples that had been cycled to specifically defined cut-off voltages. After 50 cycles of charge/discharge the cycling was interrupted at 2.9 V which corresponds to the total deintercalation of the reversibly stored Li. Additionally, a sample was prepared by interrupting the cycling at 0.7 V after 50 cycles, corresponding to the highest intercalated state studied here. To prevent the samples from reacting to oxygen or other species in the environment before the measurement, the samples were prepared in an argon-filled glovebox with $H_2O$ and oxygen concentration < 1 ppm. First, the cell was opened, and the electrode was rinsed with dimethyl carbonate (DMC) (~300 μL) and let to dry. To remove the sample from the copper current collector a piece of Kapton tape was applied on top of the electrode and removed, leaving the sample attached to the tape. Subsequently, the tape was folded to isolate the sample before it was moved out of the glovebox.

### 3.1.5   Small-angle X-ray Scattering (SAXS)

SAXS is a technique used to study the scattering of X-rays occurring in the small 2ϑ angle region around a transmitted direct X-ray beam. Depending on the angular range, it provides symmetry information at the nanoscale, around 1-100 nm. The technique was used to evaluate the space group symmetries of ordered mesoporous carbons studied in **Paper V** and **VI**. The measurements were performed on a Mat:Nordic instrument from SAXSLAB.

### 3.1.6  Nitrogen Sorption

Nitrogen sorption is a technique used to evaluate the specific surface area, the pore size, pore volume and pore size distribution of a material, through the adsorption of nitrogen on the surface. The nitrogen adsorption begins with the adsorption of a monolayer which allows, by using the theory of Brunauer – Emmett – Teller (BET), to calculate the specific surface area. By increasing the nitrogen partial pressure exposing the sample, the phenomenon of capillary condensation occurs inside the pores of the material, which leads to a rapid increase in the amount of nitrogen adsorbed. This area of the nitrogen sorption isotherm is used to measure the pore size/volume and pore size distribution following the method of Barret - Joyner - Halenda (BJH). In **Paper I, II, III, V** and **VI** $N_2$ adsorption and desorption isotherms were recorded at -196 °C using a Micromeritics Tristar instrument. The pore volume and size distribution were determined from the adsorption isotherm and the BJH method and the specific surface area was calculated by the BET multipoint method.

### 3.1.7  X-ray Photoelectron Spectroscopy (XPS)

X-ray photoelectron spectroscopy (XPS), also known as electron spectroscopy for chemical analysis (ESCA), is a technique used for the analysis of the surface chemistry of a material. The obtainable information is the elemental composition, the empirical formula, the chemical and electronic states of the elements within a material. The spectra are obtained by irradiating a solid surface with a beam of X-rays while simultaneously measuring the kinetic energy of electrons emitted from the top ~10 nm of the material. A photoelectron spectrum is recorded by counting through a detector the ejected electrons over a range of electron kinetic energies. Peaks appear in the spectrum from atoms emitting electrons of characteristic energies. Both the energies and intensities of the peaks enable the identification and quantification of the surface elements (except hydrogen). In **Paper IV,** XPS was used to analyse the surface of an electrode composed of niobium doped mesoporous titania beads, after being cycled in contact with an ionic liquid electrolyte. In **Paper V,** the technique was used to study the effect of nitrogen doping on the surface chemical structure of ordered mesoporous carbons. In both papers, the XPS measurements were performed with a PHI 5000 Versa Probe III Scanning XPS Microprobe, ULVAC-PHI, Inc., using a monochromatic AL X-ray source (E = 1486.6 eV) with a beam diameter of 100 μm and an energy resolution of 0.646 eV.

## 3.2  Electrochemical Characterization

### 3.2.1  Galvanostatic Charging with Potential Limitations (GCPL/GCD)

Galvanostatic charge discharge (GCD), also called galvanostatic charging with potential limitation (GCPL) is a constant current based technique used to measure the variation of the potential with time.[73] This technique is useful to gain basic information on the electrochemical processes of the material under study, but it is also very suited to evaluate the cycling stability of single electrodes and devices. In **Paper I**, GCD tests on ordered mesoporous titania electrodes were performed between 0.7 V to 2.9 V in a Scribner 580 battery cycler. In **Paper II**, GCD tests on mesoporous anatase beads negative electrodes

were performed between 0 V / 1 V to 2.9 V in a Scribner 580 battery cycler and in a Biologic VMP-3 potentiostat. In **Paper III**, GCD tests on niobium doped mesoporous titania beads were performed between 1 V to 2.9 V in a Scribner 580 battery cycler. In the case of **Paper IV**, the Biologic VMP-3 potentiostat was used instead. Ordered mesoporous carbons in **Paper V** were tested by GCD between 0.01 V and 2.9 V in the Scribner 580 battery cycler. Finally, in **Paper VI**, GCPL analysis was conducted on a Scribner 580 battery cycler, on a Biologic VMP-3 Potentiostat and on a Gamry Reference 600 Potentiostat. The measurements were done both on two and three-electrode configurations and were aimed at analysing the electrochemical signature of a redox enhanced electrochemical capacitor and its electrodes' contributions. Figure 6 reports the voltage *vs.* time curves for the different types of electrochemical mechanisms presented in the thesis: capacitive, pseudocapacitive and faradaic.

### 3.2.2 Cyclic Voltammetry (CV)

Cyclic voltammetry is one of the linear sweep voltammetry techniques.[73] The experiment is based on sweeping the potential linearly with time and recording the current *vs.* voltage. This allows studying the redox processes of the electrodes in detail, being the current proportional to the concentration, the square root of diffusion coefficient and sweep rate. The charge transfer kinetics can also be evaluated, for example by measuring the differences in the peak separation as a function of sweep rate for quasi-reversible electron transfer reactions. In a typical setup, the cell is composed of a working electrode, being the focus of the experiment, a counter electrode, to control the current, and a reference electrode, which acts as a voltage reference.

In this work, CV was used to determine the electrochemical signature of the mesoporous titania, always acting as working electrodes. In **Paper I**, CV measurements were performed with a three-electrode T-cell setup to which lithium foil was used as counter and reference electrode. The working electrode, consisting of ordered mesoporous titania, and the counter electrode were pressed together with a separator between them. The cell was filled to the brim with electrolyte before the reference electrode was inserted. The cell was carefully closed and sealed with Parafilm ® laboratory film and aluminium foil to prevent leakage and evaporation of the electrolyte out of the cell and oxygen/moisture from entering the cell. The CV measurements were carried out at voltages from 0.7, 1.0, 1.3, or 1.7 to 2.9 V, respectively, in a Bio-Logic VMP-3 potentiostat. In **Paper II**, CV measurements were performed on a half-cell configuration in a Bio-Logic VMP-3 potentiostat at different scan rates to study the electrochemical response of mesoporous anatase beads electrodes. Moreover, CV measurements were performed on a three-electrode T-cell setup to which silver foil was used as reference electrode and Kuraray YP 50F activated carbon as counter electrode. The CV measurements were carried out in a Bio-Logic VMP-3 potentiostat at different scan rates. Figure 6 reports the current *vs.* voltage curves typical for the different types of electrochemical mechanisms presented in the thesis: capacitive, pseudocapacitive and faradaic. In **Paper IV,** the electrochemical signature of Nb-doped mesoporous titania beads in an ionic liquid was studied via CV at 10 mV s$^{-1}$ in the potential window 0 to -2.1 V *vs.* Ag/Ag$^+$. In **Paper VI,** the CV measurements were conducted both in a Bio-Logic VMP-3 potentiostat and on a Gamry Reference 600 potentiostat. The CV was used to study the electrochemistry of a redox enhanced electrochemical capacitor in a three-electrode configuration *vs.* Ag/AgCl.
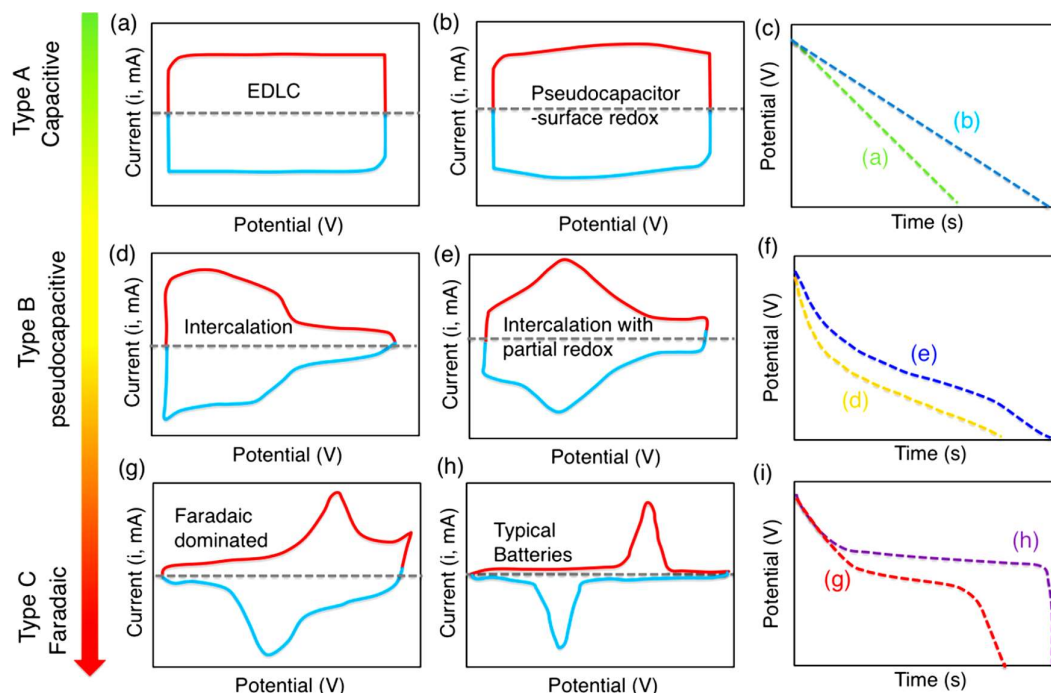
**Figure 6**: *(a, b, d, e, g, h) Schematic cyclic voltammograms and (c, f, i) corresponding galvanostatic discharge curves for various kinds of energy-storage materials. A pseudocapacitive material will generally have the electrochemical characteristics of one, or a combination, of the following categories: (b) surface redox materials (d) intercalation-type materials, or (e) intercalation-type materials showing broad but electrochemically reversible redox peaks. Electrochemical responses in (g−i) correspond to battery-like materials. Reproduced with permission from* [14].

### 3.2.3 Electrochemical Impedance Spectroscopy (EIS)

Electrochemical Impedance Spectroscopy (EIS) is focused on the impedance characteristics of an electrochemical system over a range of frequencies when an AC potential is applied.[73] Its interpretation is typically complex and requires the use of an equivalent circuit to model the different components of the electrochemical system under analysis. In **Paper I**, EIS was used to investigate the impedance signature of ordered mesoporous titania. The spectra were recorded with a Bio-Logic VMP-3 potentiostat between 1 MHz and 100 mHz in a three-electrode configuration with Li foil as pseudo-reference electrode. In **Paper II**, EIS was used to investigate the impedance signature of mesoporous anatase beads. The spectra were recorded with a Bio-Logic VMP-3 potentiostat between 1 MHz and 100 mHz in a two-electrode cell. In **Paper III**, EIS was used to evaluate the effect of niobium doping on the charge transfer resistance of electrodes based on mesoporous anatase beads. The spectra were recorded with a Bio-Logic VMP-3 potentiostat between 1 MHz and 100 mHz. In **Paper IV**, EIS was used to investigate possible changes during cycling in the electron transfer processes of Nb-doped mesoporous titania beads in an ionic liquid electrolyte. The measurements were performed in two different frequency intervals, 10 MHz to 10 mHz for the measurements before cycling and 10 MHz to 1 Hz for the in-situ measurement to reduce the acquisition time.

# 4.  Mesoporous Titania for High Rate Lithium-ion Storage

## 4.1  Background

This chapter deals with the use of $TiO_2$ as an active material for lithium-ion storage. First, an introduction to the material and a summary of the recent literature regarding the charge storage mechanism and performance of titania are given. In this work, some of the drawbacks of titania as anode for lithium storage are addressed by synthesizing different mesoporous morphologies and doping them with hetero-atoms. Finally, the synthesis schemes, characterizations results and understanding are presented. The results reported are the topic of **Paper I, II, III** and **IV.**

### 4.1.1  Titanium dioxide (TiO₂)

Titanium dioxide, commonly called titania, is an abundant and environmentally friendly material. Around 80 % of the total global production is devoted to pigments for paint, plastics, and papers. Other applications are found in the cosmetics sector, in the production of ceramic materials and in the textile industry. Being a semiconductor with photocatalytic activity, nanostructured titania has been extensively studied for various energy-related applications, including solar cells and electrochemical storage, and applied for green uses as in self-cleaning surfaces and water/air purification.[12,74] $TiO_2$ presents three natural crystalline polymorphs: anatase (tetragonal), brookite (orthorhombic) and rutile (tetragonal). The rutile phase is the thermodynamically stable phase under normal conditions. The unit-cell structures are presented in Figure 7. $TiO_2$ (B), as for bronze, is a monoclinic phase produced typically via hydrolysis of $K_2Ti_4O_5$ and heating. Low-temperature synthesis allows for the productions of amorphous titania, showing a defective anatase structure.
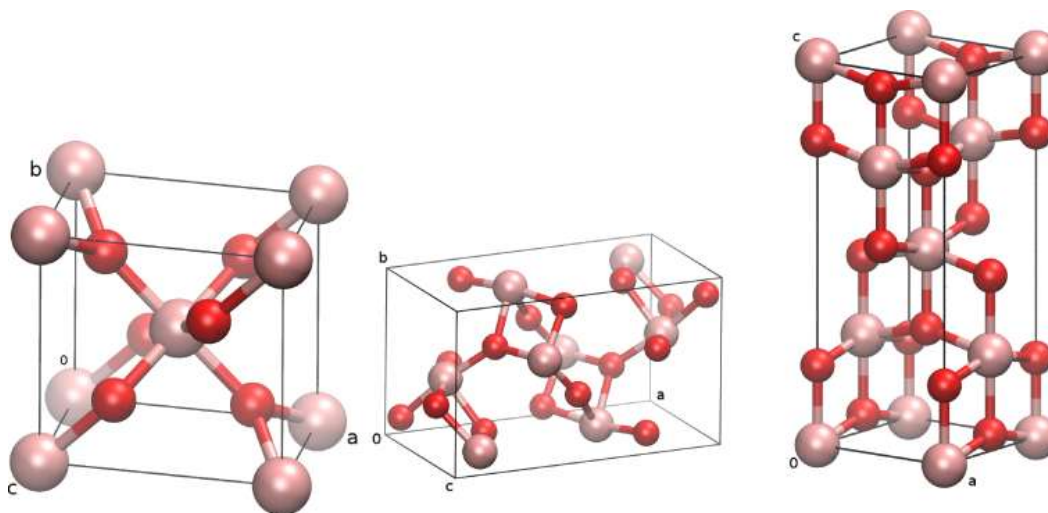


***Figure 7****: crystal structure of rutile, brookite and anatase (from left to right).*[75]

Anatase contains 12 atoms per unit-cell octahedrally coordinated, with each Ti atom to six O atoms and each O atom to three Ti atoms. The $TiO_6$ octahedron is partly distorted, with two Ti-O bonds slightly larger than the others and a deviation from 90° of some O-Ti-O bond angles.

## 4.1.2   Titanium dioxide as Anode for Lithium-ion Storage

Titanium dioxide has been extensively studied as possible alternative of graphite as anode for lithium-ion batteries. The material is appreciated for its abundance, safety, stability during cycling and good rate performance.[76] Even though all the natural crystalline polymorphs have been analysed in connection to lithium storage, anatase has attracted the most focus thanks to a structure more open for lithium accommodation.[77] In this paragraph, some fundamentals of lithium insertion into the anatase phase and an introduction to the strategies typically used for the optimization of titania anodes are presented.

Anatase has a theoretical lithium specific capacity of 335 mAh g$^{-1}$, which corresponds to the formation of a $LiTiO_2$ phase. However, bulk anatase does not reach experimentally the theoretical limit because of the slow Li-ion diffusivity into the crystal structure.[78] Nanosizing the active material is a preferred strategy to overcome diffusion-limitations because by size reduction it is possible to decrease the diffusion distances by increasing the surface to volume ratio. Consequently, many different nanostructured titania morphologies, including nanotubes, nanoparticles and thin films, have been studied.[79–81]

The process of lithium insertion into anatase can be distinguished in three main sub-processes depending on the voltage window.[82,83] As an illustrative case, half-cell potential *vs.* capacity curves, cycling at 165 mA g$^{-1}$ in a standard LP30 organic electrolyte, for anatase nanoparticles (average diameter of ~15 nm) are shown in Figure 8. The process of lithium insertion corresponds to the discharge curve. The first region of the curve, above 1.8 V and at low lithium concentrations, is characterized by the formation of a solid solution and its length depends on the particle size.[84] The region corresponding to the plateau is associated with a phase separation and formation of the orthorhombic $Li_{0.5}TiO_2$, when half of the octahedral sites are filled.[85] In the next region, after the plateau, the remaining sites are filled to form tetragonal $Li_1TiO_2$, following a phase separation mechanism, even though a plateau is not visible.[86] The lithiation process is fully reversible so that during discharge the lithium ions diffuse away and the anatase structure is restored.
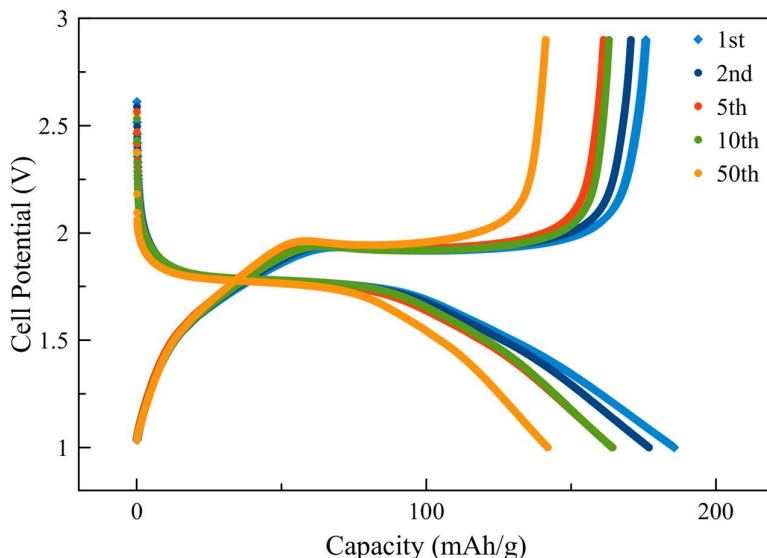


**Figure 8**: *Chronopotentiometry curves of an anatase nanoparticles electrode at 0.5 C.*

Different observations suggest that the extent of the first plateau and the hindrance of the second plateau are caused by the slow lithium ion diffusivity and a lithiation rate effect.[87] The rate effect is in turn deeply associated with the low diffusion rate. Experimentally, a full lithiation is achievable only at very low rates, like 0.01C (1C is the rate at which the material would achieve its theoretical capacity in 1 h, whereas at 0.01C the corresponding capacity is achieved in 100 h). At 0.5C, as in Figure 8, only the surface of the active materials can be fully lithiated. The formation of $Li_1TiO_2$ on the surface eventually limits the lithium-ion transport inside the particle.[88] It follows that the particle size has a fundamental impact on the achievable specific capacity. In the case of large particles, > 10 nm, only the surface, few nm, can reach the theoretical capacity. However, when the particle size is reduced to 5 nm, also the inner part can reach the fully lithiated $Li_1TiO_2$. The size reduction not only affects the diffusion distance, but also the lithium solubility is increased, and the phase transformation is suppressed, avoiding the formation of a fully lithiated blocking layer.[89] Mesoporous materials with interpenetrating nanopores and thin walls can provide high surface areas for the lithium ions to diffuse into the material and avoid phase separation.

Figure 8 gives also other information about the cycling process. In the first five cycles, the coulombic efficiency is lower, and the capacity decreases fast. These phenomena are caused by side reactions happening at the electrode/electrolyte interface. Different studies suggest that the initial irreversibility is caused by $Li^+$ ions trapping followed by the reaction of the electrolyte with adsorbed water on the $TiO_2$ surface.[90] The nature of a solid electrolyte interface (SEI) on the titania surface is still under debate. The high insertion potential seems to avoid the formation of a traditional passivating SEI, as for carbon materials, happening at potentials inferior to 1 V.[91] However, a recent study reported the formation of an "apparent/conductive" SEI not passivating the electrode surface, which remains electrochemically reactive.[92] By using an ionic liquid as electrolyte, it seems possible to stabilize the surface of the active material and reduce the irreversible capacity loss.[93]

Nanostructured titania materials with high surface areas store charge by three different electrochemical mechanisms: a faradaic contribution due to the diffusion-limited Li insertion process; a capacitive contribution due to the formation of an electric double layer; and a pseudocapacitive contribution of insertion type (see Chapter 2, section 2.3) due to fast surface redox processes, responsible for the full lithiation of the first few nm of material surface.[94] The limit between bulk redox reactions and pseudocapacitive processes is yet not fully elucidated. It has been demonstrated that pseudocapacitive contributions, and consequently rate capabilities, are favoured by a higher intrinsic conductivity.[95]

The development of strategies to improve the electronic and ionic conductivity has been probably the most recent research topic regarding lithium storage in titania materials. Typically, titania electrodes contain carbon additives to guarantee continuous electronic paths to the current collectors. A lot of interest has been given to the design of composite titania/carbon electrodes showing higher rate capabilities and increased specific performance, by for example encapsulating $TiO_2$ nanoparticles into porous carbons or properly mixing titania sheets with highly conductive carbon morphologies.[96–98] Studying new titania polymorphs has also attracted a lot of interest. For example, the nanostructured $TiO_2$ (B) polymorph shows fast lithium insertion kinetics and high rate capabilities.[99] Also, amorphous titania, has shown good performance at high charge/discharge rates, thanks to its defective surface structure.[100] However, it is also characterized by a high initial irreversible capacity, which is not very suitable for practical applications.[101] The process behind the onset of irreversible capacity is not yet fully clear. Some studies reported that

lithiation induces the formation of an inactive phase composed of crystalline lithium titanate. Other researchers suggest that the lithium ions react with OH and water adsorbed on the surface, leading to the formation of lithium oxide.[102]

A very effective way to increase the conductivity of titania is by doping with hetero-atoms.[103] One possibility is by doping with $Nb^{5+}$ ions through a donor-type process.[104] Undoped anatase has a natural n-type character which leads to the natural formation of oxygen vacancies. The Nb doping seems to increase the n-type character of anatase, improving its electronic and ionic diffusivity.[105] Moreover, the charge compensation of the niobium substitution is achieved by two different mechanisms: the reduction of one $Ti^{4+}$ to $Ti^{3+}$ ion per $Nb^{5+}$ ion introduced or the formation of one Ti vacancy per four niobium ions incorporated.[106] The former introduces shallow donor levels below the conduction band providing improved electronic conductivity, while the latter might positively influence the ionic diffusivity. It has been shown that the increase in electronic conductivity is correlated to an increase of the pseudocapacitive contributions to the charge storage. This effect might be attributed to the formation of a space charge layer, arising from surface states with a different Fermi level than that in the bulk. The space charge layer induces a depletion of electrons at the surface and an accumulation of $Li^+$ ions, leading to higher pseudocapacitive contributions.[107]

## 4.2   Mesoporous TiO$_2$ Synthesis, Electrode Preparation and Use in Devices

### 4.2.1   Synthesis of Ordered Mesoporous Amorphous TiO$_2$

In **Paper I**, ordered mesoporous titania was prepared by a spray deposition method. All the chemicals used in the synthesis were bought from Sigma Aldrich. 3 g ethanol (99.5%, Solveco), 2.25 g block copolymer Pluronic$^{TM}$ F127 and 1.5 g 5 M HCl were mixed in closed propylene bottles under stirring until the F127 was completely dissolved. Subsequently, 1.5 g titanium butoxide (97%) was added to the solution and the solution was stirred for 10 minutes, to dissolve the precursor. The final molar composition was 1 : 14.8 : 1.57 : 0.041 of titanium butoxide : ethanol : HCl : water : F127. The solution was kept at 40 °C for three hours in closed propylene bottles. The reaction solution was then spray deposited, for 15 s, on glass slides (VWR 631-1551, 76 x 26 mm) using an Aztek A470 Airbrush, with a 0.30 mm general-purpose nozzle. After deposition, the film was aged for 72 hours in a closed climate chamber at 75% relative humidity (RH). Finally, the films were exposed to UV irradiation for 24 hours to photocatalytically remove the F127 polymer template.

### 4.2.2   Synthesis of Mesoporous TiO$_2$ Anatase Beads

In **Paper II, III** and **IV**, mesoporous anatase beads were produced by a soft templating method.[108] Titanium (IV) isopropoxide (TIP) (> 97%), ammonium hydroxide solution (30-33%), potassium chloride (KCl) (99.99%) and 1-hexadecylamine (HAD) (90%), were purchased from Sigma Aldrich. The synthesis follows a controlled hydrolysis of TIP in hydroalcoholic medium, absolute ethanol (99.7%), for 18 h with HAD as a structure-directing agent and KCl to regulate ionic strength. The process is followed by autoclaving at 160 °C in hydroalcoholic ammonia, NH$_4$OH in MilliQ water and absolute ethanol for 16 h. Final calcination is performed at 500 °C for 2h in air. The mesoporous anatase beads

doped with $Nb^{5+}$ were prepared following the same path. The niobium is introduced by substituting the appropriate amount of TIP with niobium (V) ethoxide during synthesis. The amount of doping (0.1% at., 1% at. and 10% at.) was dispersed by ultra-sonication in 1 mL of absolute ethanol and mixed with the TIP before being added to the hydroalcoholic HAD-KCl medium.

### 4.2.3 Preparation of Electrodes and Devices

The fabrication of electrodes has a strong influence on its electrochemical performance. Different parameters, namely the choice of current collector and binder, the slurry composition and the active materials processing, were investigated. The optimized preparation scheme for both the ordered amorphous titania and the mesoporous anatase beads is as follows:

The titania active material was pre-treated by gentle ball milling at 10 Hz for 10 min in a $ZrO_2$ coated cup with $ZrO_2$ balls in a Retsch MM400 ball mill. The material was then mixed in a glass vial with carbon black, Super-P™ (Alfa Aesar), and Kynar® PVDF binder (Arkema) 5 % (w/w) solution in NMP (N-methyl-2-pyrrolydone, anhydrous, 99.5 %, Sigma Aldrich). The solution was stirred overnight in a capped vial, forming a slurry having a weight ratio of 8:1:1 ($TiO_2$ : Super-P : PVDF). The slurry was coated onto a copper foil through a TQC AB3400 motorized automatic film applicator. A stainless-steel doctor blade (Wellcos Co.) was used to obtain a 150 μm thick coating of the slurry. The electrode sheets were dried for one day at ambient conditions in a fume hood, followed by drying in a vacuum oven at 80 °C for 2 h. The electrodes (~10 mm diameter, 2 mg cm$^{-2}$ active material) were transferred to a glove box, under argon atmosphere with $O_2$ and $H_2O$ content less than 1 ppm and dried under vacuum at 80 °C in a Buchi oven.

Two-electrode coin cells, used in all the four papers, were assembled in argon-filled glovebox using CR2032 housings. Glass microfiber (Sigma Aldrich) was used as separator, soaked with 30/40 μL of commercial LP30 (1 M $LiPF_6$ in EC: DMC, 1:1) (Sigma Aldrich), and lithium metal disk was used as counter electrode (~11 mm, 4 mg cm$^{-2}$). In **Paper I**, three-electrode T-cells were assembled with lithium foil used as counter and reference electrode. The working electrode and the counter were pressed together with a separator between them. The cell was filled to the brim with electrolyte before the reference electrode was inserted. The cell was carefully closed and sealed with Parafilm® film and aluminium foil to prevent leaking and evaporation of the electrolyte out of the cell and oxygen/moisture from entering the cell. In **Paper II**, a hybrid Li-ion capacitor was built using the mesoporous anatase beads electrode as negative electrode and Kuraray YP 50F activated carbon as positive electrode. The activated carbon electrodes (~10 mm diameter, ~300 μm, ~12 mg cm$^{-2}$) were prepared following a procedure reported in literature.[109] In **Paper III** and **IV,** three-electrode Swagelok T-cells were assembled with the mesoporous anatase beads electrode as negative electrode and the Kuraray YP 50F carbon electrode as positive electrode. A silver disk was used as pseudo-reference electrode. The cell was filled to the brim with electrolyte. In Figure 9, a schematic of the three-electrode Swagelok T cell is presented. The electrometers disposition is chosen to measure simultaneously all the three voltage components while controlling the current between working and counter, in accordance with the operating conditions of a final device.
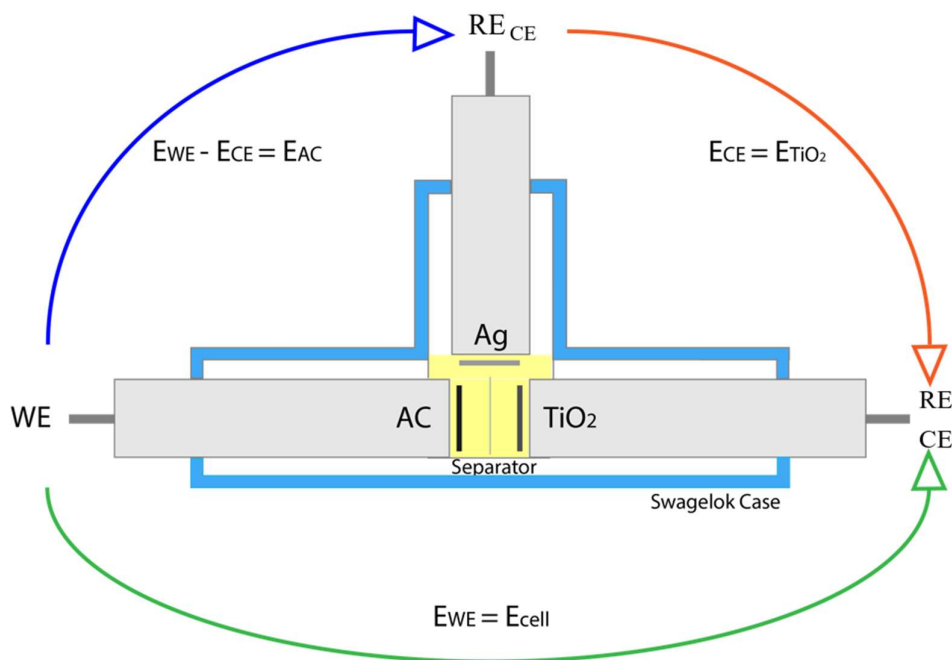
*Figure 9: Schematic representation of a three-electrode Swagelok T-cell setup.*[110]

## 4.3 Insertion Mechanism and Performance of Mesoporous TiO$_2$ Electrodes

In section 4.1.2, different challenges to the practical application of TiO$_2$ as anode for lithium storage were presented. The goals of our research regarding mesoporous titania electrodes were to address some of these challenges and uncover the process of Li storage:

- To deal with the low diffusion coefficient of bulk materials and the drawbacks of some nanostructures, we decided to use mesoporous materials with morphologies designed in our laboratories. In **Paper I**, we studied the lithiation of ordered mesoporous amorphous titania, while **Paper II** deals with the lithiation of mesoporous anatase beads. The two materials store electrochemical energy through Li$^+$ ion insertion and extraction, however, the fundamental mechanisms are different and consequently also the associated electrochemical signatures. These differences arise due to the specific structural features of the two materials. Thereby, it was important to combine electrochemical and structural characterization to gain a better picture of the processes involved.

- To increase the electronic and ionic conductivity, therefore enhancing the redox kinetics, we doped the mesoporous beads morphology with Nb. In **Paper III** we studied the effect of the niobium doping on the lithiation process and the rate performance.

- To avoid high irreversible capacities and degrading performance we followed two paths. In **Paper IV** we present the use of an ionic liquid (IL) as electrolyte, following the concept that the presence of the IL might stabilize the surface of the active materials. On the other hand, in **Paper II**, we show that by limiting the voltage window, the high initial irreversibility can be avoided also when using an organic electrolyte. A Li-ion capacitor can be consequently designed to efficiently exploit the change in voltage window.

### 4.3.1 Lithiation of Ordered Mesoporous Amorphous TiO₂

In **Paper I**, we studied the lithiation of mesoporous amorphous titania to understand how the amorphous phase and the ordered array of mesopores would influence the transport and insertion of Li ions.

The material was characterized by X-ray absorption spectroscopy (XAS), to study the local environment of the titanium atoms, as shown in Figure 10 with an anatase reference. The theory of XAS correlates the edge position to the oxidation state of the element, and in our case the two titania polymorphs show similar energies, associated with the oxidation state $Ti^{4+}$. Important information regarding the coordination and symmetry of the element can be extrapolated from the pre-edge region. By studying the A1, A2 and A3 peaks positions and intensity, it was concluded that the mesoporous titania contains a combination of [5]Ti and [6]Ti, as previously defined and reported for amorphous titania.[111–113] Amorphous titania nanoparticles seem to be composed of an anatase-like core with structural defects near the surface. Besides, the absence of a shoulder in the absorption edge of the mesoporous titania further depicts a difference in symmetry of the titanium atom compared with the anatase material.
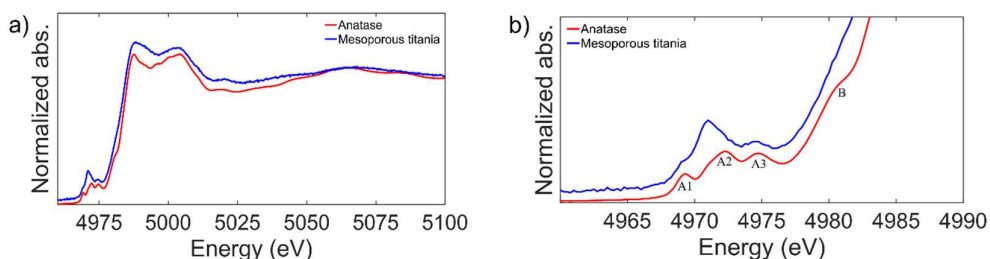


**Figure 10**: XAFS spectra of the anatase and the pristine mesoporous titania samples. The pre-edge features are highlighted (b). The absorption spectra are shifted in intensity for clarity.[114]

The mesoporous titania electrodes were electrochemically characterized by GCD and CV in a half cell configuration, as shown in Figure 11. In the GCD curve, the material exhibits a quasi-linear dependence of the stored charge with the potential. A very high capacity of ~680 mAh g⁻¹ is observed for the first discharge cycle, and then the capacity decreases rapidly in the following cycles, with the second retaining only 40 % of the initial capacity (~280 mAh g⁻¹). Furthermore, the CV test, at the scan rate of 0.3 mV s⁻¹, reports a pseudocapacitive behaviour of insertion type, extrinsic due to the mesoporous morphology and intrinsic due to the amorphous structure. The under-coordinated Ti atoms in the mesoporous material may give rise to the intrinsic pseudocapacitance.
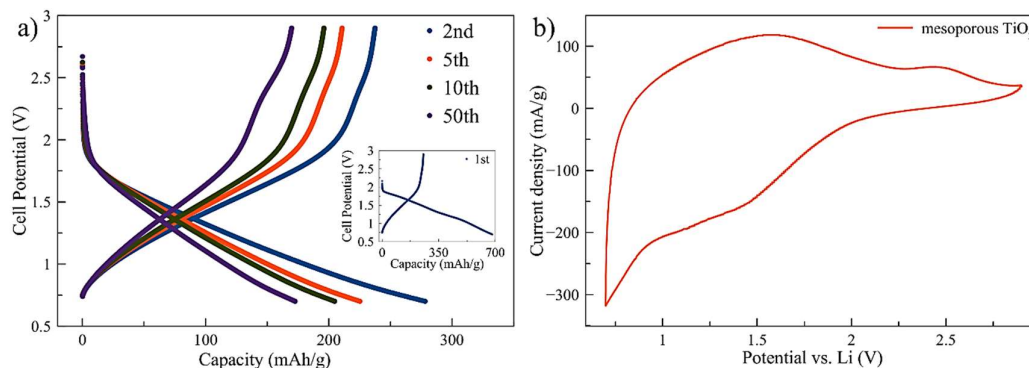
***Figure 11***: *a) Charge/discharge curves of mesoporous titania electrodes between 2.9 V and 0.7 V cycled at 0.5 C. b) cyclic voltammetry curves (10th cycle) scanned between 2.9 V and 0.7 V for mesoporous titania at a scan rate of 0.3 mV s$^{-1}$.*[114]

Stability and rate capability tests are reported in Figure 12. The initial large irreversibility is concentrated to the first 20 cycles. Thereafter, the capacity fading is slower, and the electrode shows 80 % capacity retention for almost 200 cycles. In the rate performance test, the electrodes deliver 83 mAh g$^{-1}$ at 10 C and high recovery of capacity when cycled again at lower rates.
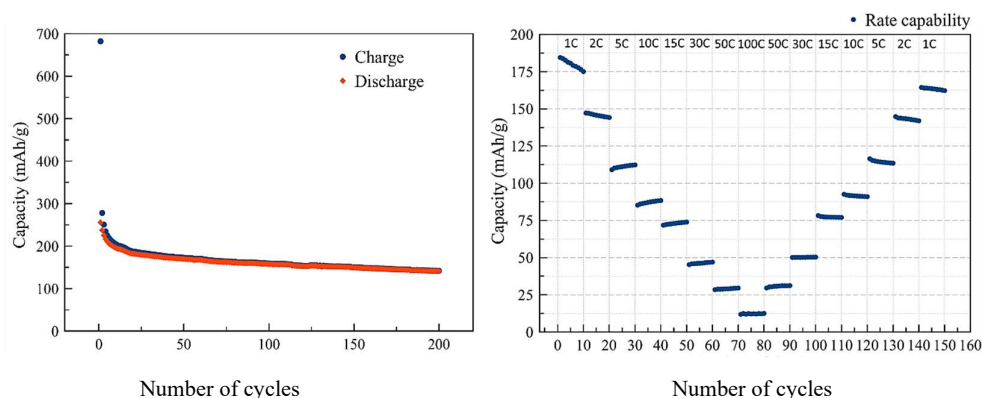


***Figure 12:*** *Charge and discharge capacity vs. number of cycles (a) and the performance at higher rates (b) of the mesoporous titania electrodes.*[114]

The mesoporous amorphous titania was expected to perform better at high rates thanks to its pseudocapacitive behaviour of both extrinsic and intrinsic character. We believe that the large irreversibility exhibited in the initial cycles might be the reason for this modest performance. A combination of CV, XAS and TEM have been used to study the origin of the irreversibility and the associated structural changes in the material. Figure 13 shows CV tests at different cut-off voltages (1.7 V, 1.3 V, 1.0 V and 0.7 V) of electrodes cycled for 50 cycles.
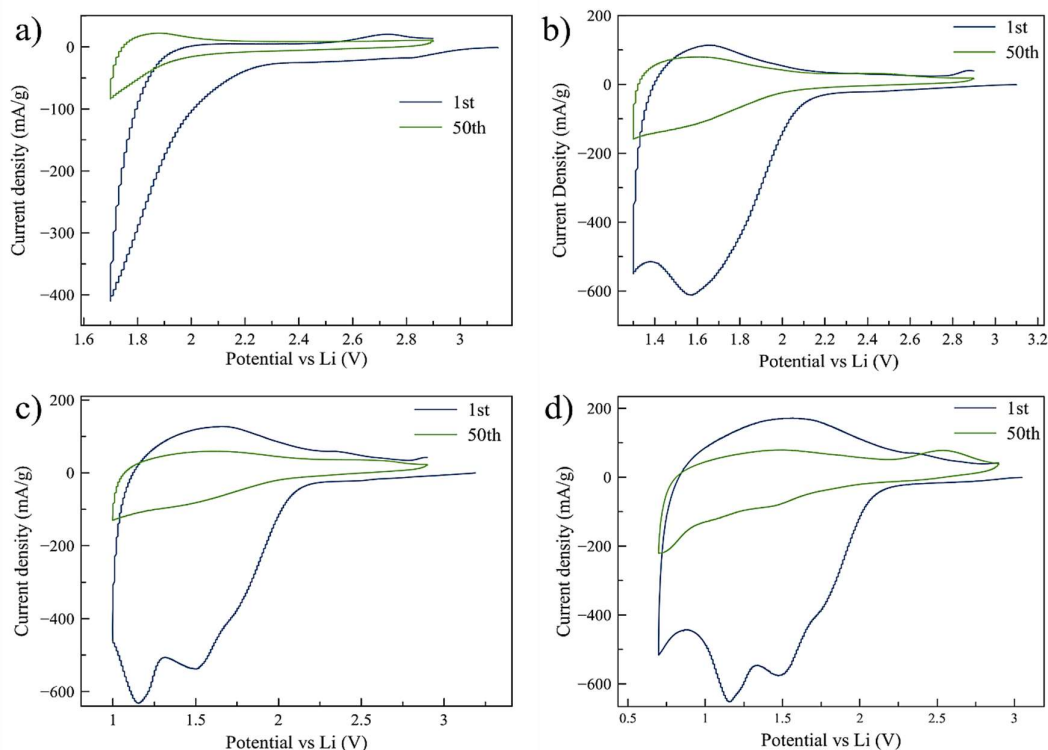
***Figure 13***: *Cyclic voltammetry scans performed with a three-electrode setup at 0.3 mV s$^{-1}$ between 2.9 V and 1.7 V (a), 2.9 and 1.3 V (b), 2.9 and 1.0 V (c), and 2.9 and 0.7 V (d). The first and fiftieth cycle of each CV are shown in the graphs.*[114]

A large irreversibility is observed even at 1.7 V, where the concentration of Li ions inserted in the titania structure is typically low with x < 0.5 in $Li_xTiO_2$. Figure 13 (d) depicts two well defined reduction peaks, a shoulder peak and an increase in current at 0.7 V. We believe that the peaks are associated with the formation of electrochemically irreversible phases. The increase in current at 0.7 V is generally believed to be originated from the formation of a solid electrolyte interface (SEI).[92,115]

To investigate the structural changes connected to the other peaks, XAS and TEM were used. XAS measurements in Figure 14 were performed in both the intercalated (0.7 V) and deintercalated (2.9 V) states. The post-edge region, also identified as NEXAFS region, contains spectral features associated with multiple scattering phenomena and provides information on the structural changes induced by the lithiation process.[116–118]
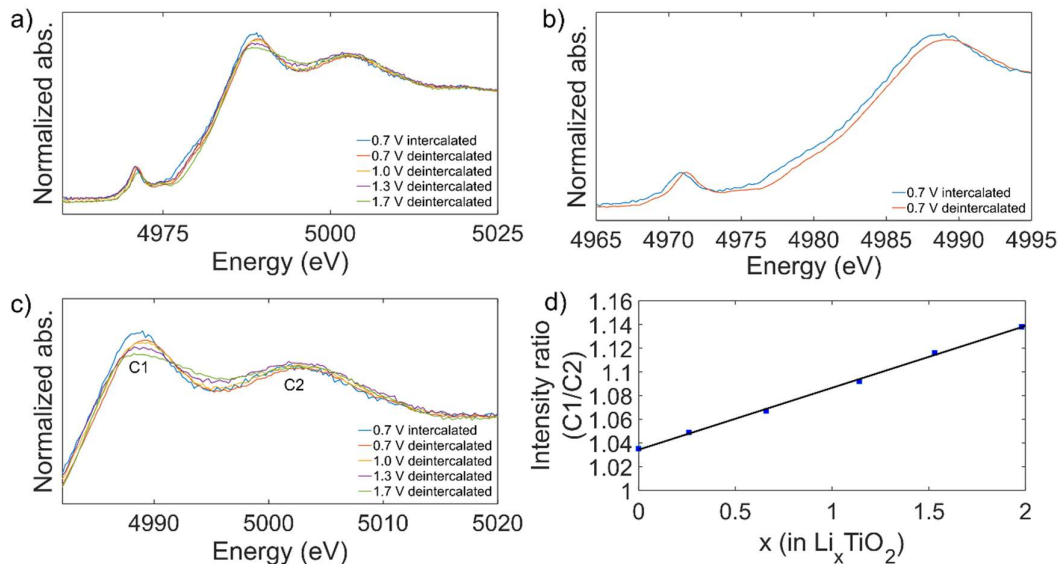
**Figure 14**: *XAS spectra of the cycled samples (a) and a comparison of the intercalated and the deintercalated state of the samples cycled to 0.7 V, showing a shift in the edge position (b). The post-edge region of the XAS spectra of pristine and cycled mesoporous titania is highlighted (c) and the effect of the lithium concentration on the peak intensity ratio C1/C2 (d). The point at x=0 is for the pristine sample.*[114]

In Figure 14 (c) the peak intensity C1/C2 increases with lowering the cut-off voltage and at 0.7 V the sample in the intercalated state has a higher peak ratio than the sample in the deintercalated state. It appears that the presence of irreversibly bound lithium affects the multiple scattering processes. The concentration of irreversibly bound lithium conceivably increases with lower cut-off potential and consequently has a larger impact on the multiple scattering processes, leading to the shift in the intensity ratio of the C1/C2 peaks in Figure 14 (e). The graph depicts a linear correlation between the lithium concentration and the C1/C2 intensity ratio. The linear relationship is valid for electrodes in the deintercalated state and electrodes in the intercalated state, which contains also reversibly bound lithium. The local environment of the titanium atom is, therefore, affected similarly by the different lithium intercalation phenomena occurring during cycling, further indicating that the distance between the inserted lithium and the titanium atom is very similar regardless whether the lithium is reversibly or irreversibly bound. Because of this indistinguishable effect on the multiple scattering, we conclude that lithium is positioned in the proximity of the titanium atom forming $Li_xTiO_2$ species. Also, this implies that formation of the lithium-containing species outside the near environment of the titania structure, such as lithium oxide, is improbable in our conditions.

To further verify the formation of $Li_xTiO_2$ species, we used TEM imaging. In a previous publication, it was shown that the titania material is mesoporous and contains small crystallites of anatase.[119] Bright-field (BF) and high-resolution (HR) TEM images of the electrode cycled to 1.7 V and interrupted in the deintercalated state, are shown in Figure 15. The image in panel d shows a crystal of ~15nm, with lattice fringes that corresponds to the {400} planes of $LiTiO_2$. The crystalline lithium titanate formation can be linked to the shoulder peak at 1.7 V, seen during the CV measurements (Figure 13). It appears that the

formation of lithium titanate is caused by local crystallization phenomena at average Li concentration that are below x = 1 in $Li_xTiO_2$, and responsible in part for the irreversible capacity.
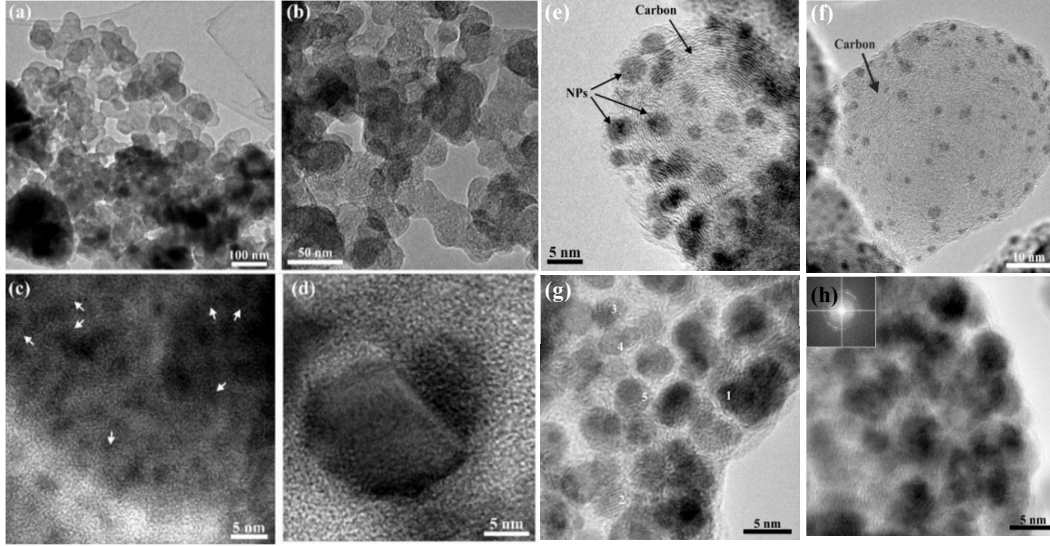


*Figure 15: Bright field TEM images of the electrode cycled to 1.7 V showing the overall morphology of the sample (a, b) and HR-TEM images showing the nanocrystalline anatase (c) and $LiTiO_2$ (d). BFTEM images of the electrode cycled to 1.0 V, which consists of carbon particles incorporating smaller crystalline nanoparticles (e, f). HRTEM images used for d-spacing measurements (g). The inset shows the FFT diffractogram that corresponds to the whole image (h).*[114]

Figure 15 (e-h) shows TEM images of the electrode cycled to 1.0 V and interrupted in the de-intercalated state. To establish the nature of the crystalline nanoparticles, the d-spacing was determined using a combination of lattice fringes analysis and measurements based on the reflections present in the FFT from the nanoparticle area. The phases investigated as possible structures were anatase, lithium oxide ($Li_2O$) and lithium titanate ($LiTiO_2$). The observed linear relationship between the C1/C2 intensity ratio and the lithium concentration (Figure 14d) supports the hypothesis that $Li_xTiO_2$ phases were formed in the electrode. The mesoporous titania material contains a large amount of amorphous phase, which is not readily detected in the TEM images, and consequently the lithium-containing phases are, presumably, partly amorphous.

To get more insight on the irreversibly bound lithium distribution, energy filtered (EF) TEM experiments were performed on the electrode cycled to 1.0 V and interrupted in the de-intercalated state. The areas were energy filtered so that the maps of Li, Ti and O elemental distributions were obtained. As can be seen in Figure 16, Li appears to be located mainly at the surface while Ti and O are distributed over the whole area. Considering the nature of the amorphous titania phase, which contains a large number of defects near the surface, and the lithium-titanium elemental map, it appears that the irreversible phases are mainly located at the surfaces. The high quantity of lithium observed in the energy filtered images is in line with the large irreversibility observed in the CV curve of the electrode. The

composite elemental maps show that lithium is located near both titanium and oxygen, which is an observation that is in line with our hypothesis that irreversible $Li_xTiO_2$ species are formed while cycling the electrodes.
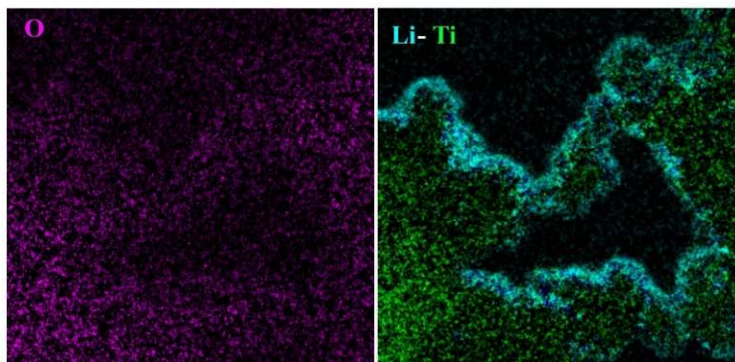


*Figure 16*: *Energy filtered images and composite elemental maps of the mesoporous titania cycled to 1.0 V. From the composite elemental maps, it can be seen that Li appears to be located mainly at the surface while Ti and O are distributed over the whole area.*[114]

We suggest that the formation of irreversible phases on the surface of the material can contribute to the lower than expected rate capability of the mesoporous amorphous titania. The irreversible phases possibly reduce the diffusion rate of Li ions inside the titania structure. Further studies need to be done to verify this hypothesis.

### 4.3.2   Lithiation of Mesoporous TiO₂ Anatase Beads

In addition to the ordered mesoporous amorphous titania, we synthesized micro-metre-sized mesoporous beads of 100% anatase phase. Micro-metre-sized sphere like materials are optimal for the preparation of electrodes, thanks to their high packing densities. Moreover, together with the high accessible surface area given by the mesoporosity, highly crystalline materials are typically showing increased pseudocapacitive contribution. In **Paper II** we studied the lithiation process into mesoporous titania beads synthesized by soft templating approach.

The TiO₂ beads crystal structure, morphology and porosity were studied through XRD, N₂ adsorption and SEM. Figure 17 clearly shows that the material consists of hierarchically organized micrometre-sized beads, each composed of an agglomerate of nanoparticles. The material is highly crystalline and monophasic, showing only the tetragonal anatase polymorph and an average crystallites size of ~25 nm. The calculated BET specific surface area is ~90 $m^2\,g^{-1}$ and the BJH pore volume was determined to be 0.355 $cm^3\,g^{-1}$, with a narrow mesopore size distribution around ~15 nm.
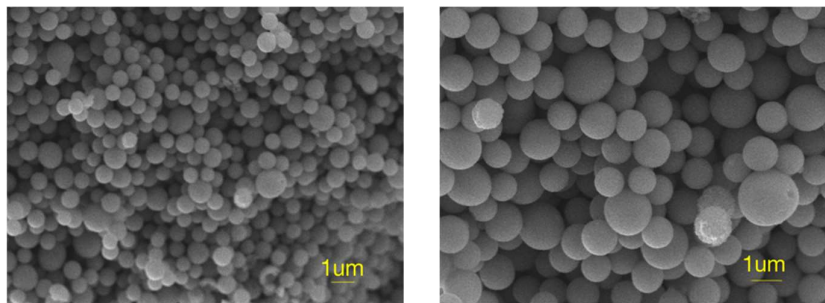
***Figure 17***: *SEM micrographs of the TiO₂ beads in two magnifications. The 2nd image clearly shows the aggregation of the nanoparticles in a spherical minimized surface energy structure.*[110]
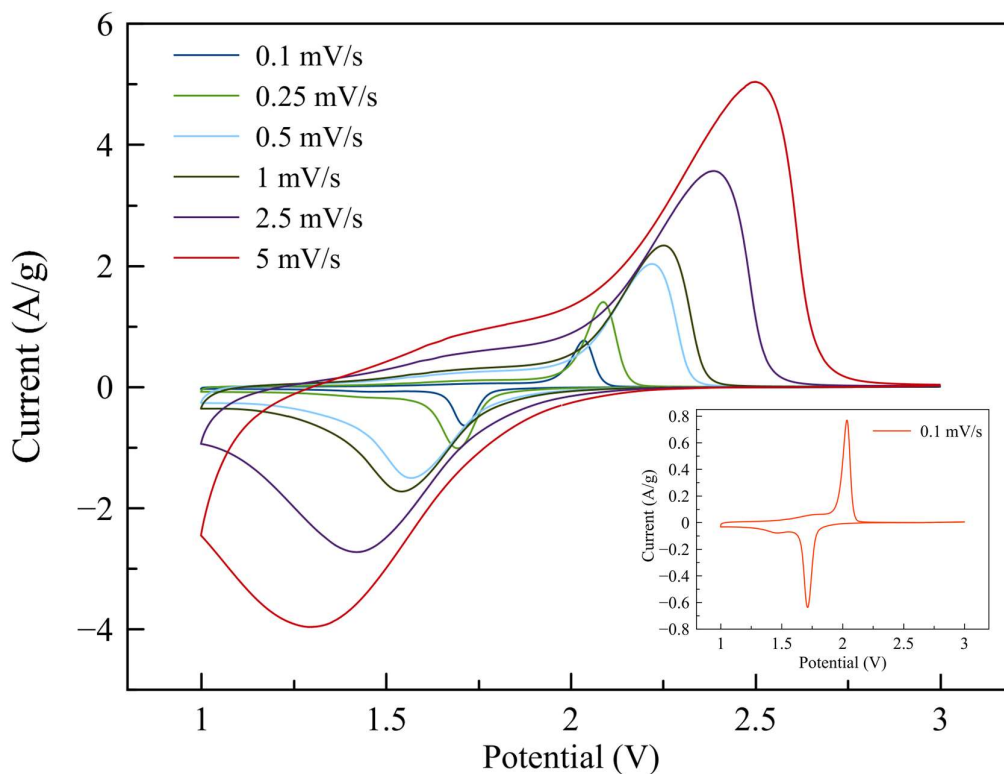


***Figure 18***: *Cyclic voltammetry curves of the anatase beads vs. Li at different scan rates of 0.1, 0.25, 0.5, 1, 2.5 and 5 mV/s. The inset reports a curve at 0.1 mV/s.*[110]

The electrochemical performance of the mesoporous beads electrodes was studied via half-cell configuration. Figure 18 reports the CV curves at scan rates from 0.1 to 5 mV s$^{-1}$, which exhibits typical and well-defined peaks. The hierarchical mesoporous structure allows for a complex storage of charges. Influenced by the specific surface area and the nanosized crystallites, three storage mechanisms can simultaneously take place: the formation of a double layer of charges associated to capacitance; the redox Li insertion process, limited by diffusion; and fast surface redox processes giving rise to a pseudocapacitance of insertion type.[94] To differentiate between the different contributions to the total charge storage, the data from the CV curves performed at different rates are used. The relation between the

measured current $i$ and the scan rate $v$ provides an understanding of the mechanisms involved.

Following the so-called "isopotentials" treatment, presented in **Paper II**, the relative capacitive contribution at the scan rate of 0.5 mV s$^{-1}$ was calculated to be 30 % of the total charge storage, as can be seen in Figure 19. At the scan rate of 5 mV s$^{-1}$ the capacitive current is more significant and contributes to almost 60 % of the total charge due to the rapid cycling. The double-layer capacitance, which is proportional to the relatively low specific surface area, contributes little to the total capacitance.

It follows that most of the capacitive current is pseudocapacitive in nature. This result further proves that the hierarchical morphology allows for the mesoporous beads to be easily accessed by the electrolyte and undergo fast surface redox reactions.
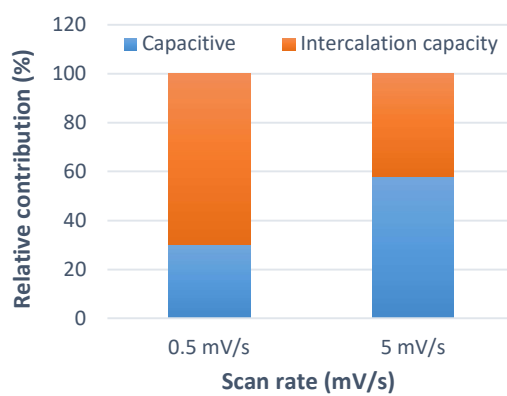


**Figure 19**: *Relative contribution of the pseudocapacitive charge storage at 0.5 and 5 mV/s for the mesoporous anatase beads electrode.*[110]

To further evaluate the cycling stability of the electrodes, GCD measurements were performed at the rate of 0.5C, which corresponds to 165 mAh g$^{-1}$. Figure 20 shows the GCD curves at different cycles and the discharge capacity *vs.* number of cycles. The potential *vs.* capacity curves in panel (a) show three different regions and extended voltage plateaus corresponding to the anodic and cathodic peaks of the CV curves. The material is affected by irreversible capacity only for the first few cycles, showing stable performance afterwards with more than 95% capacity retention after 150 cycles. The mesoporous bead morphology demonstrates insertion/extraction reversibly for high amounts of lithium in applicable operating conditions.
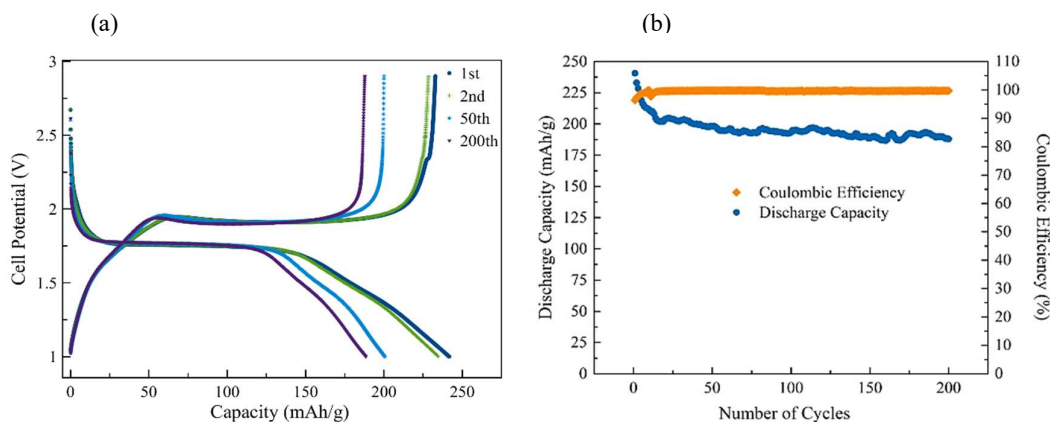
**Figure 20**: (a) GCD curves of mesoporous anatase beads electrode for the 1st, 2nd, 50th and 200th cycles at 0.5C. (b) discharge capacity and coulombic efficiency vs. number of cycles.[110]

Figure 21 reports the discharge capacities *vs.* number of cycles at different C rates of mesoporous anatase bead electrodes. The electrodes show very good rate performance, delivering 100 mAh g$^{-1}$ at 10C, which means it is possible to charge the electrode in only 6 minutes, corresponding to 50% of the capacity storable in 2 hours. This high rate storage is possible thanks to the high pseudocapacitance shown by the material. Moreover, the high rate of cycling is not damaging the mesoporous beads and, therefore, has a limited effect on the electrochemical performance. When the cycling step is reversed, the electrodes store a similar capacity when cycled at low rates. Figure 22 shows SEM images of a titania bead anode both in the pre-cycling and post-cycling conditions. The morphology of the beads in the post fast-cycling condition looks practically identical to the pristine state. This result further proves the high stability of the mesoporous anatase beads morphology.
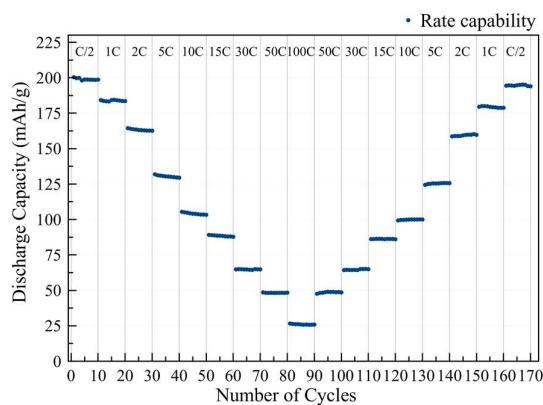


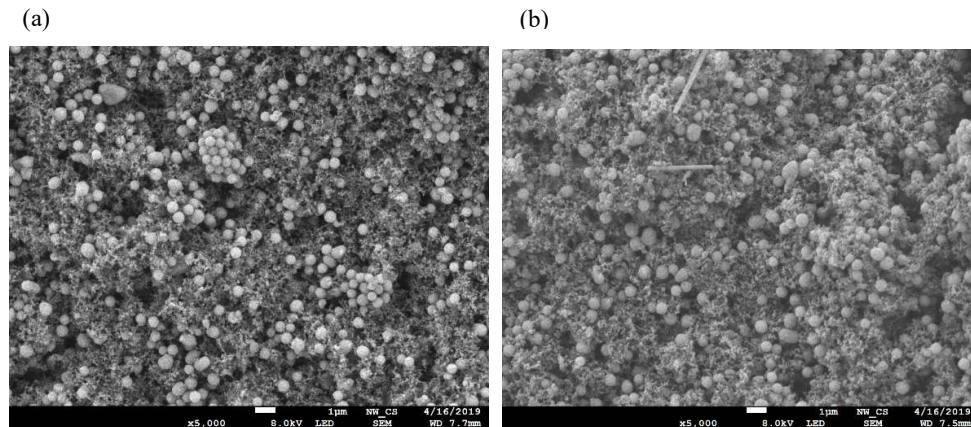**Figure 21**: Rate performance in terms of specific discharge capacity for mesoporous anatase beads electrodes.[110]

31

(a)                                                    (b)



**Figure 22**: *SEM images of a titania bead anode surface at a) pre-cycling and b) post-cycling.*[110]


### 4.3.3  Effect of Nb-doping on the Performance of Mesoporous $TiO_2$ Anatase Beads

Thus far, we have shown that an accessible mesoporous beads morphology, characterized by high surface area and high crystallinity, is well suited for high rate Li-ion storage thanks to high pseudocapacitive contributions. To further improve the rate performance of the materials, we can combine the hierarchical porous structure with an increased electronic and ionic conductivity of the semiconducting $TiO_2$. This can be achieved through the insertion of $Nb^{5+}$ ions into the anatase structure through a donor-type doping process. In **Paper III** we studied the effect of the niobium doping concentrations (0.1 %, 1 % and 10 %) on the charge storage mechanism of the mesoporous anatase beads.
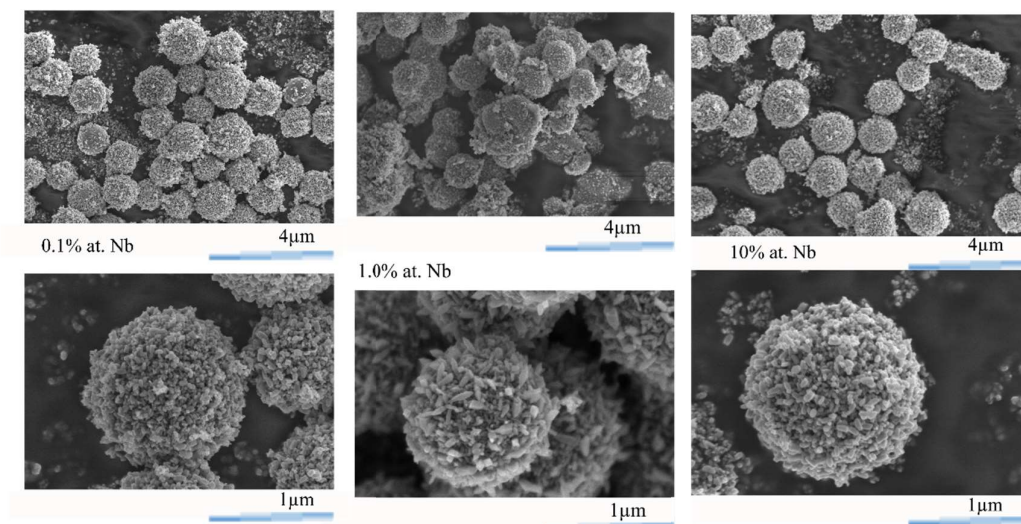


**Figure 23**: *SEM images of mesoporous anatase beads electrodes prepared with different concentrations of niobium.*


Figure 23 illustrates that all the materials exhibit micrometre-sized spherical morphology as a result of the template-assisted sol-gel synthesis. The morphology is not affected by the

nature and amount of doping. However, the particle size slightly increases with the amount of doping as reported in the TEM images for 0.1 and 10 at. % Nb-doped TiO2, Figure 24.
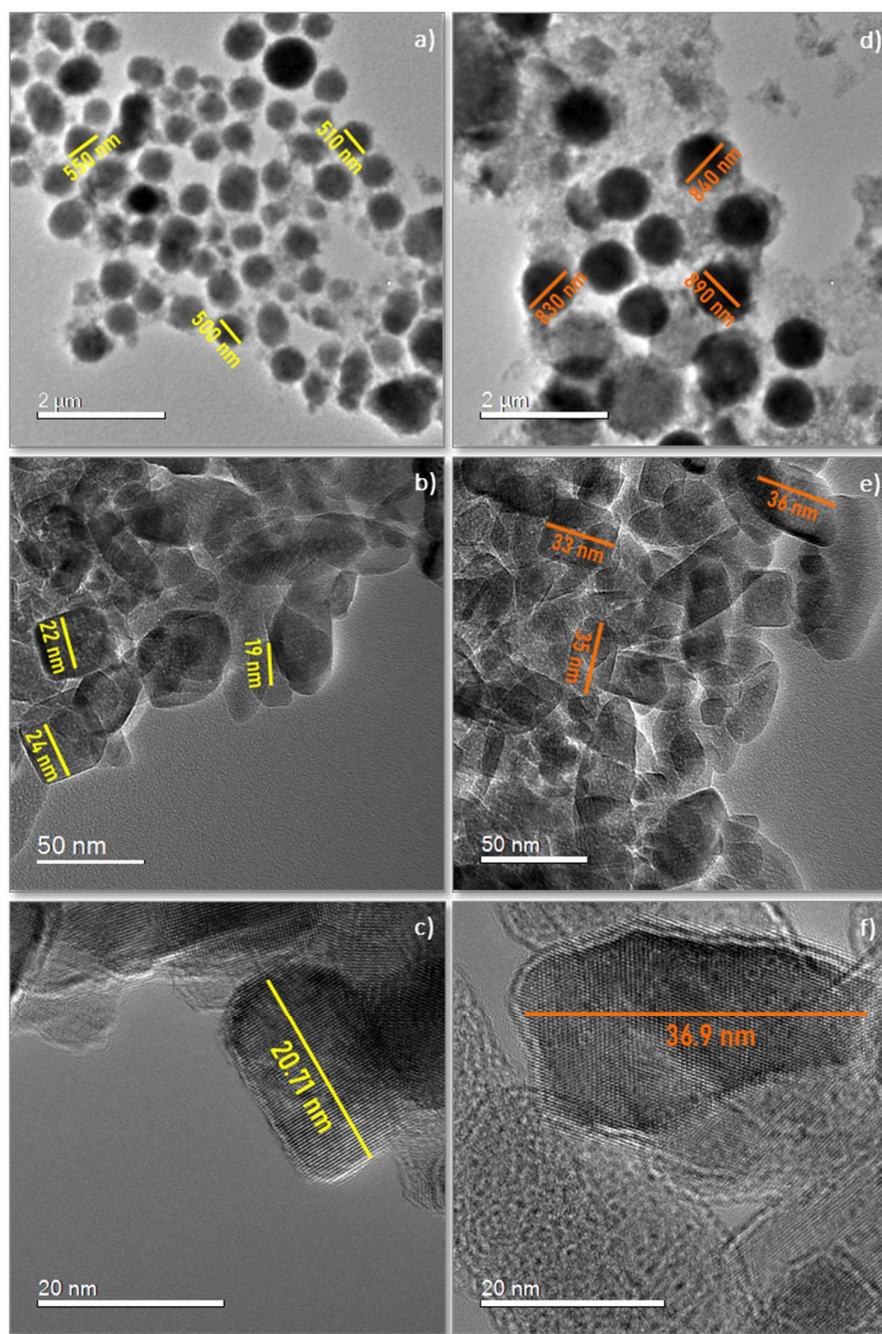


**Figure 24.** *High-Resolution Transmission Electron Microscopy (HRTEM) images recorded at various magnifications (x20k, x140k, x600k) for two compositions (left and right columns refer to 0.1 and 10 at. % of Nb, respectively). Sizes of the beads and nanoparticles are evidenced by yellow and orange lines for 0.1 and 10 at. % of Nb, respectively.*

HRTEM images recorded at low magnification (x20k) (Figure 24a and d) show a spherical organization of the nanoparticles, achieved to minimize the surface energy. Depending on the composition, a diameter variation of the spheres is evidenced. Specifically, Figure 24a indicates an average diameter of 500 µm for the lowest doping concentration (0.1 at.% Nb) compared to a larger 850 µm for 10 at.% Nb (Figure 24d). HRTEM images at medium magnifications (Figure 24b and e) reveal a distribution of randomly oriented rice-grain or cube-shaped nanoparticles. A statistical analysis of Figure 3b exhibits an average particle size close to 23 nm, while larger ($\approx$ 35 nm) nanoparticles are observed for the 10 at.% doped $TiO_2$ (Figure 24e). The two images (Figure 24c and f) acquired at high magnification (x600k) confirm this result.

Figure 25 reports the X-ray diffractograms for the three niobium-doped materials and the sizes of the nanoparticles, as calculated from the Rietveld analysis. The patterns confirm that all of the samples are monophasic with reflections ascribed only to the anatase phase. The diffraction peaks related to the (101) planes gradually shifts to lower 2 $\Theta$ values with Nb-doping, due to the enlargement of the unit cell caused by the substitution of $Ti^{4+}$ with $Nb^{5+}$. Considering the similarity in ionic radii ($Nb^{5+}$ is only 5.8 % larger than $Ti^{4+}$) and the extent of lattice expansion (0.012 % between 0.1 % Nb and 10 % Nb), it is reasonable to assume that $Nb^{5+}$ occupies $Ti^{4+}$ sites. The results of the Rietveld analysis further confirm the substitutional character of the doping. The nanoparticles' size increase linearly with the Nb doping, with an increase of a and c axes and thus of the overall volume of the anatase crystal cell. These observations are in good agreement with the TEM analysis. The Raman spectra reported in **Paper III** gives another confirmation of the substitutional nature of the solid solution of Nb-doped anatase.



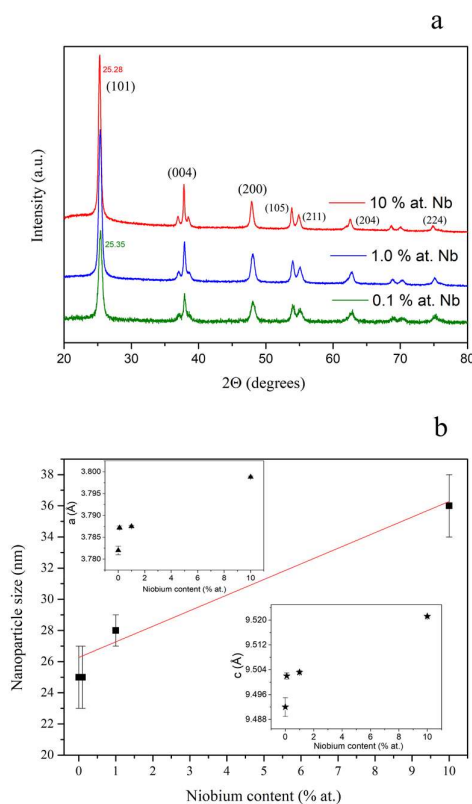*Figure 25: a) X-ray diffractograms of Nb-doped mesoporous anatase beads at different concentrations. The (101) peak is shifted from 25.35° 2$\Theta$ at 0.1 at.% to 25.28° at 10 at.%; b) nanoparticle size determined from the Rietveld analysis and unit cell parameters size.*

DFT calculations were performed to model the influence of the niobium introduction on the electronic properties. Specifically, it is interesting to look at the electronic density of states (DOS) projected for each atomic species and normalized by their respective number of atoms in the supercell. Figure 26 shows the DOS for the undoped, 1.0 at.% and 10 at.% Nb concentrations. The $TiO_2$ anatase was modelled considering a 5 x 5 x 2 supercell with 100 Ti atoms and 200 O atoms. It was therefore not possible to model the 0.1 at.% Nb, which would have required a supercell of at least 1000 atoms. With the introduction of Nb, starting from the 1 at.% case, the Fermi energy level (the zero-energy vertical line in the plot) is shifted to the bottom of the conduction band, which in turns provides the compound with a metallic-like character. The topology of the band structure is unaffected by the doping process, even when reaching 10 at.% Nb concentrations. In the latter case, the occupation of the conduction band states is further increased.



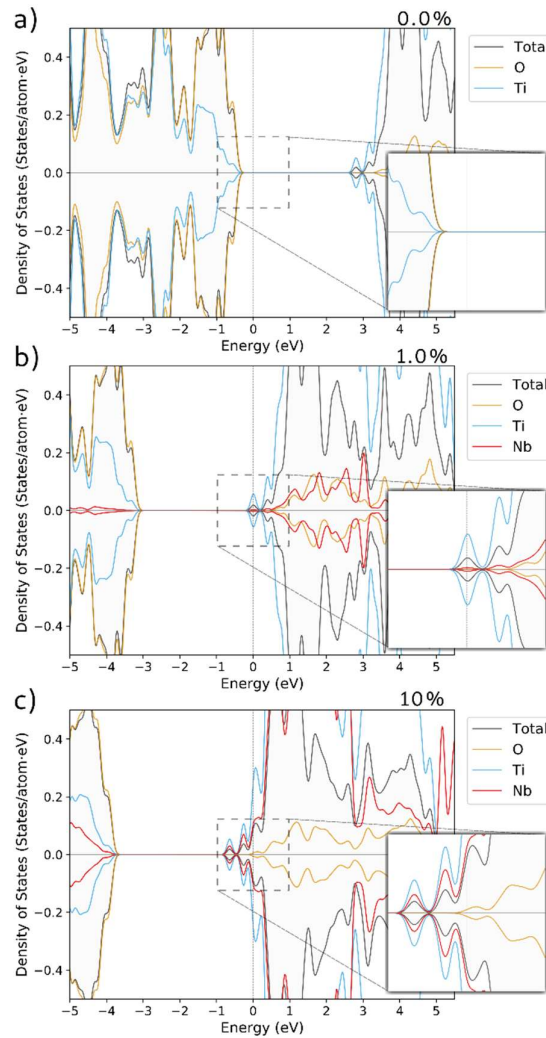*Figure 26*: *Electronic density of states projected for each atomic species and normalized by their respective number of atoms in the supercell for the (a) 0.0 at.%, (b) 1.0 at.%, (c) 10 at.% Nb-doped anatase $TiO_2$. The Fermi energy level is represented by the zero-energy vertical line. The Ti states are higher than the total states because of normalization, as we divide by their respective number of atoms in the unit cell.*

Upon lithiation, $Ti^{4+}$ is reduced to $Ti^{3+}$, accommodating the incoming electron. The Ti empty states are located in the conduction band, which is partially occupied by the n-doping. It follows that fewer Ti states are available for reduction due to lithiation. This effect is further accentuated in the 10 at.% sample, where the conduction band is even more populated. The higher doping concentration results in a greater contribution of Nb empty states for the conduction band, suggesting a possible redox activity of Nb ions. These calculations suggest that the addition of small amounts of Nb could improve the overall performance of the materials by enhancing its metallic-like character while offering a limited effect on its electrochemical properties.
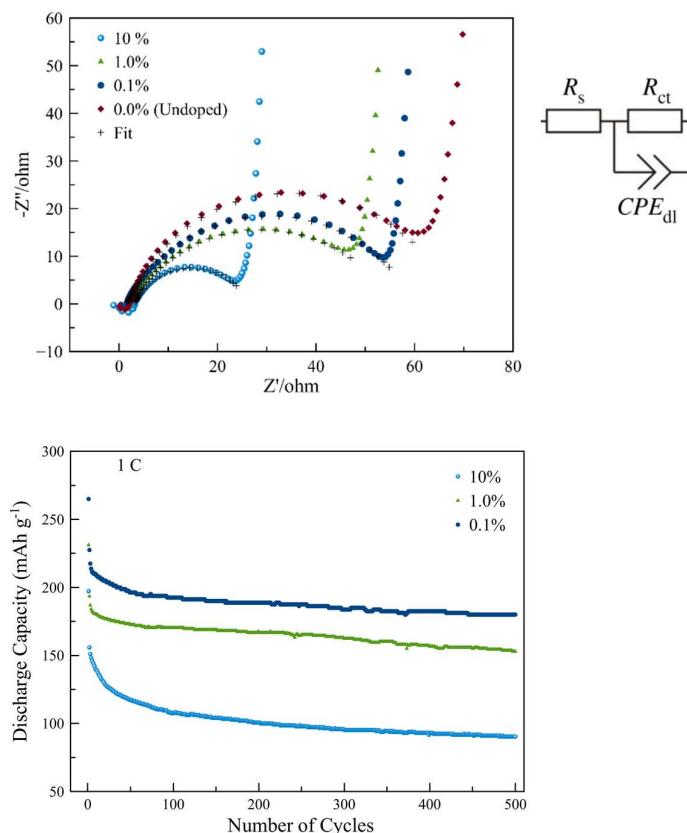


*Figure 27: a) EIS spectra for the mesoporous anatase beads and related fit of the first semi-circles. The equivalent circuit used is on the right; b) Specific capacity at 1C for the doped mesoporous anatase beads electrodes.*

In addition to the DFT calculations, the electrochemical impedance spectroscopy (EIS) data suggest an increase in conductivity, which could be connected to the shift of the Fermi level into the conduction band. Figure 27a reports EIS of the Nb-doped anatase electrodes in two electrodes configuration. On the right, the equivalent circuit has 3 main parameters: $R_s$, $R_{ct}$ and $CPE_{dl}$. At high frequencies, the intercept at Z' corresponds to $R_s$ and represents a combination of the electrolyte resistance, intrinsic resistance of substrate, and contact resistance at the composite electrode/current collector interface. The $CPE_{dl}$ (constant phase element) is associated with the double-layer capacitance of the active material. All the electrodes show similar values for both parameters. The differences appear in the semicircle

in the high-frequency range, which corresponds to the charge-transfer resistance ($R_{ct}$) caused by the Faradaic reactions. As expected, the increase in doping amount is reflected in a decrease of the semi-circle radius and the $R_{ct}$ decreases from 66 Ω of the undoped material to 58 Ω, 53 Ω and 23 Ω for the 0.1 at.%, 1 at.% and 10 at.%, respectively. This suggests an improvement in electronic conductivity.

Figure 27 reports also the specific discharge capacity *vs.* number of cycles for the three doped samples at 330 mA g$^{-1}$ (1C). As already discussed, the initial irreversible capacity is a drawback of this class of materials, and it is also affecting the Nb-doped anatase. However, after the initial irreversibility, the electrodes show stable performance for 500 cycles with 0.1 at.% showing the highest discharge capacities. The coulombic efficiency is also very high (> 99.5 %) during the entire cycling.

Figure 28 reports the galvanostatic charge/discharge curves at 1C rate for the Nb-doped titania electrodes. The initial low coulombic efficiency is associated with the irreversible phenomena happening at the electrode-electrolyte interface. The curves indicate that the doping process does not only affect the conductivity but also the lithium insertion. Starting from the 0.1 at.% doping, the Li insertion capacity is the highest and the voltage profile is characterized by a very broad insertion plateau. The low doping concentration seems to have no measurable effect on the reduction of the available $Ti^{4+}$ sites, necessary for the Li insertion reaction, as already suggested by the DFT calculations. With increasing dopant concentration, the specific capacity decreases and at 10 at.% a change in the potential profile is also seen. We believe that the reduction in capacity can be explained by the substitution of the available $Ti^{4+}$ reduction sites, in agreement with the calculations. The change in shape for the 10 at.% sample, with less extended plateaus, might be caused by the significant contribution of Nb atoms in terms of redox activity. Another explanation might be connected to the high number of donor electronic states introduced with the increasing level of doping and change in the Li accumulation at the surface
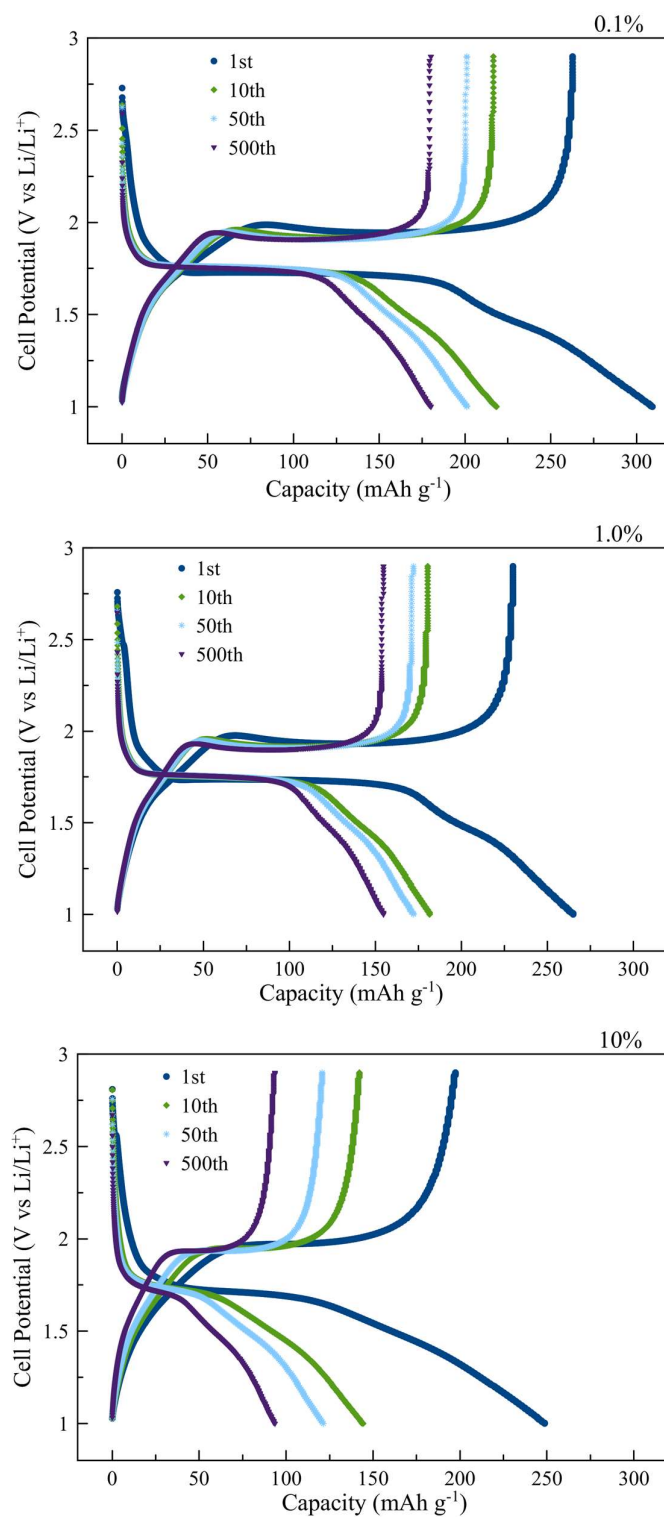
***Figure 28****: Galvanostatic charge/discharge curves at 1C for 0.1 at.%, 1 at.%, and 10 at.%
niobium doping. Theoretical capacity: 335 mAh g$^{-1}$.*

.

Finally, Figure 29 shows the rate capabilities for the three doping concentrations. The 0.1 at.% is the best performing, delivering 120 mAh g$^{-1}$ at 10C (the undoped sample delivered 100 mAh g$^{-1}$) and 53 mAh g$^{-1}$ at 100C (the undoped delivered 25 mAh g$^{-1}$). These results confirm that a small doping level is a suitable strategy to increase the conductivity of the active material without altering the Li insertion process and allow an improvement in charge transfer kinetics in connection to the fast Li-ion diffusion into the mesoporous beads morphology.
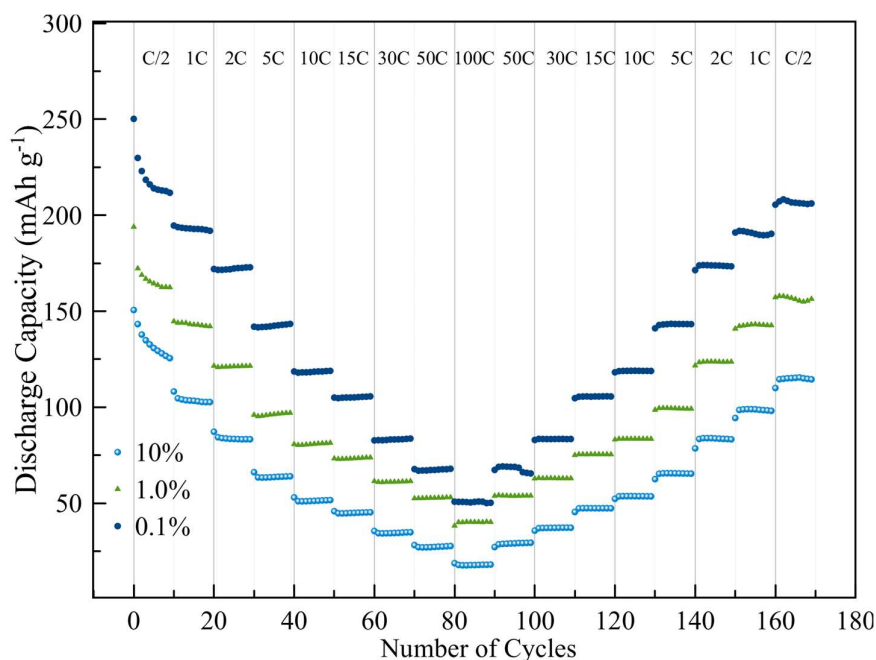


*Figure 29*: Discharge rate performance of the niobium-doped mesoporous anatase beads from 0.5C to 100C and back to 0.5C.

### 4.3.4 Li-ion Insertion into Nb-doped TiO$_2$ Beads in an Ionic Liquid Electrolyte

In the previous sections we approached the design of titania electrodes with the aim of improving the electronic and ionic conductivities. As already reported, a drawback limiting the final applicability of this material is the initial irreversible capacity loss. In the next two paragraphs we aimed at overcoming this issue by following two different strategies.

One way to mitigate this problem is to develop different electrolyte formulation, with one of the possibilities being the use of ionic liquid electrolyte. In **Paper IV**, it is demonstrated that the initial irreversibility is reduced when cycling the mesoporous anatase beads in 0.5 M of lithium bis(trifluoromethylsulfonyl)imide (LiTFSI) in 1-Ethyl-3-methylimidazolium (EMIM) TFSI. The initial capacity loss is also affected by the Nb doping, with the loss decreasing with increasing doping concentration. Therefore, it is interesting to investigate through electrochemical impedance spectroscopy (EIS) the cycling effect on the electron transfer processes when using an LP30 or an ionic liquid electrolyte.

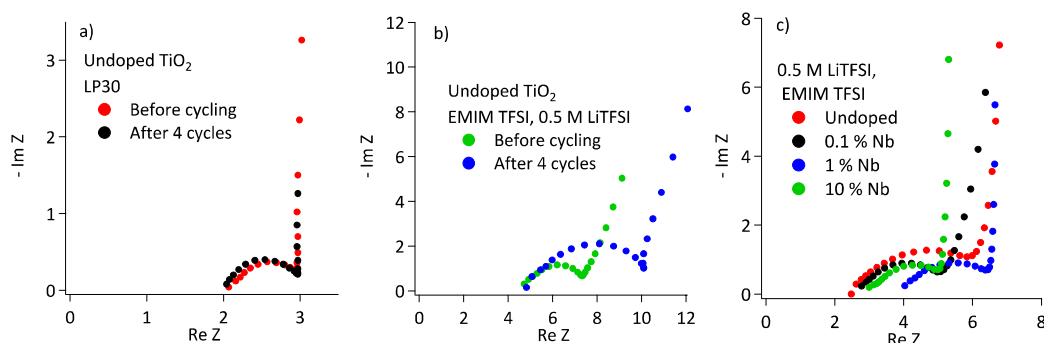***Figure 30****: EIS spectra of: mesoporous anatase electrodes in a) LiPF$_6$ in EC:DMC (LP30) and b) 0.5 M LiTFSI in EMIMTFSI, and of Nb-doped mesoporous anatase electrodes in c) 0.5 M LiTFSI in EMIMTFSI.*[120]

As shown in Figure 30a, only a small change in the frequency response is visible for the undoped material in LP30. Indeed, the SEI formed on this material is defined as apparent because it does not show effects on the electroactivity of the material surface. In contrast, when using an IL-based electrolyte, there is an increase in the semi-circle radius after four cycles. This behaviour is common for materials forming an effective SEI, reflecting an increase in the charge transfer resistance. The increase of niobium-doping results in a decrease in the semi-circle radius, similarly to the results shown in the previous paragraph. To investigate how the charge transfer resistance changes with cycling, EIS was performed in situ at different potentials of charge-discharge vs. Ag/Ag$^+$, as shown in Figure 31. The charge transfer resistance is reduced when the potential is lowered, and the lithium is inserted. When the electrode is delithiated to 0 V at the end of the first cycles, the charge transfer resistance is higher compared to the pristine electrode. During the second cycle the reduction of charge transfer resistance upon Li-ion insertion is smaller. At -0.9 V in the second cycle, the semi-circle is almost the same as at 0 V, meaning that few Li ions have been inserted. This effect can be explained by the peak shift on insertion peak visible in the CV curves. In the 2$^{nd}$ cycle, a second smaller semicircle is appearing at the left of the main one, which indicates the ongoing formation of a second phase with different charge transfer resistance.
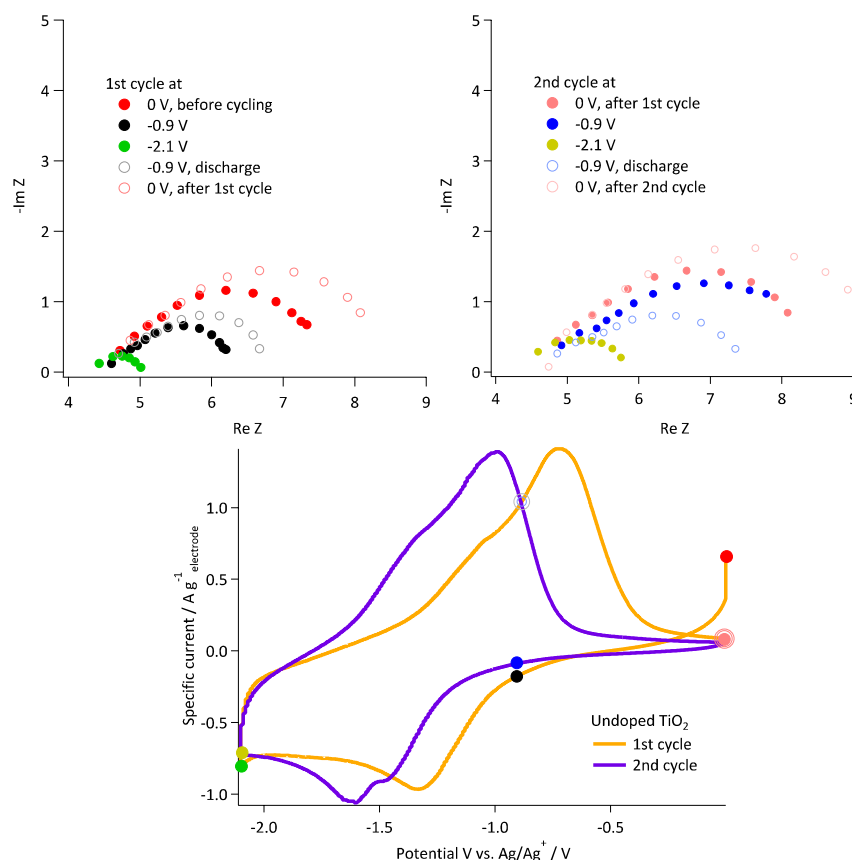
*Figure 31*: EIS spectra of the undoped mesoporous anatase beads electrode at different potentials in the 1$^{st}$ (left) and 2$^{nd}$ (right) cycles with 0.5 M LiTFSI in EMIMTFSI. Investigated potentials are indicated in the CVs from the first and second cycles (bottom).[120]

To further investigate the second phase forming on the beads surface, XPS measurements were performed on the 1 at.% Nb doped sample, in pristine and after cycling conditions. As expected, Figure 32 shows a change of the XPS spectra with the cycling. In the pristine electrode Ti, Nb, O and C can be detected. After cycling, surface groups containing oxygen, sulfur and nitrogen appear. The presence of nitrogen is explained by the decomposition of both TFSI anions and EMIM cations, while sulphur originates from the decomposition of TFSI anions.[121,122] The peaks are present from the first cycles, indicating the formation of a interphase layer of decomposed electrolyte. The decrease in intensity of the Ti2p peaks strengthens the hypothesis of a stable interphase layer covering the active material. The Ti2p of the pristine electrode, assigned to Ti$^{4+}$ species, shows slightly higher binding energy, which can be explained by the charge compensation induced by the Nb atoms substitution.[123]
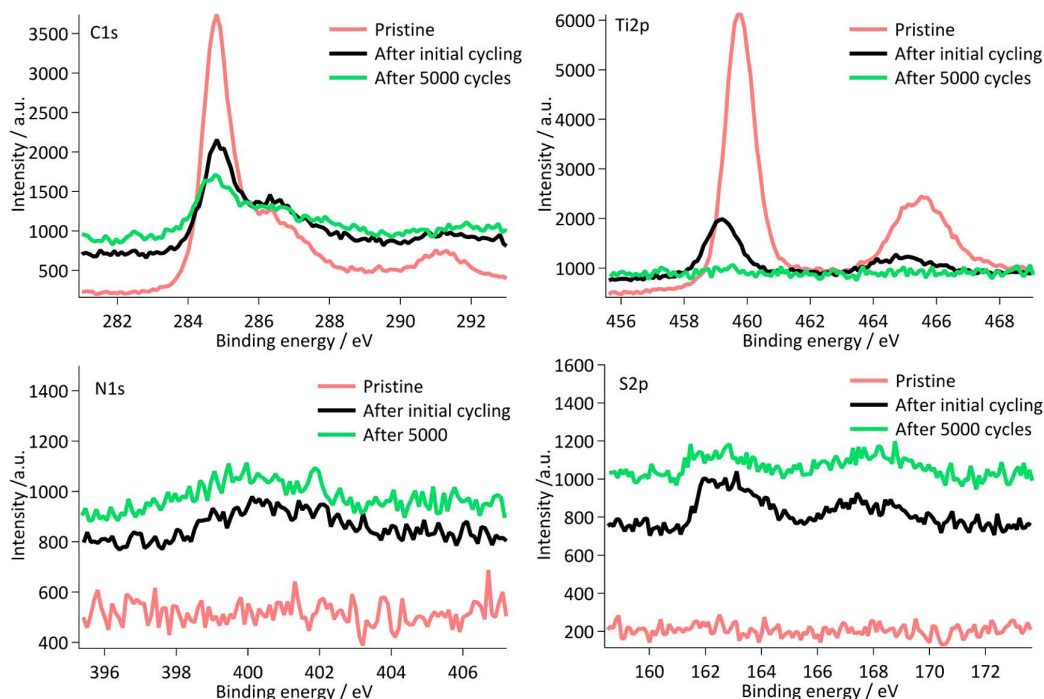
***Figure 32****: The XPS spectra of the C1s, Ti2p, N1s and S2p peaks of a 1 at.% Nb-doped mesoporous anatase beads electrode, before and after cycling.*[120]

### 4.3.5    Mesoporous TiO₂ Beads as Negative Electrode for Li-ion Capacitor

When using commercial organic electrolytes, the initial capacity fade can be avoided by limiting the cut-off voltage during charge. The voltage limiting reduces the risk of irreversible side reactions and Li-ions accumulation/trapping. In Figure 33, the electrodes were cycled to 1.6 V and show no initial capacity loss and good stability over 500 cycles.
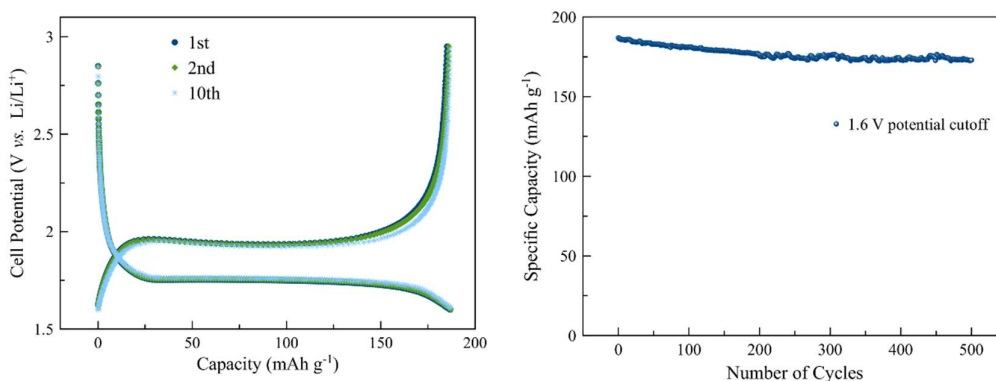


***Figure 33****: a) Galvanostatic charge/discharge curves for the 1ˢᵗ, 2ⁿᵈ and 10ᵗʰ cycles at 0.5C and b) discharge capacity as a function of the number of cycles for a mesoporous anatase beads electrode cycled to 1.6 V.*[110]

To exploit this stability and efficiently use the cut-off potential effect, the mesoporous anatase beads material was used as a negative electrode in a Li-ion capacitor configuration, with commercial activated carbon as material for the positive electrode. Figure 34a reports CV graphs conducted at different sweep rates, showing a mixed behaviour between faradic and capacitive. The anatase titania electrode stores energy through $Li^+$ ions intercalation into its structure. Whereas, the porous carbon stores charges through the adsorption of anions ($PF_6^-$) on its high specific surface area (~1800 $m^2$/g), forming a double layer of charges.[124] The formation of the double layer is shown as a linear plot of the voltage *vs.* time. To achieve charge balance, the positive electrode had a mass 6 times bigger than the negative electrode. To distinguish the contributions of the single electrodes to the overall cell voltage, a three-electrode cell was built with Ag as reference electrode. A GCD measurement conducted at 2.5 A $g^{-1}$ and reporting the waveform for the cell and the electrodes contributions is presented in Figure 34b.
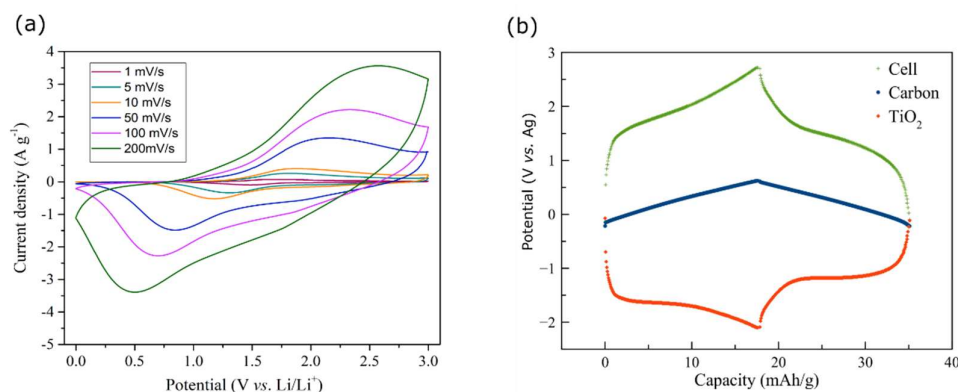


*Figure 34*: a) Cyclic voltammetry curves obtained using different sweep rates and b) galvanostatic charge/discharge curve at 2.5 A $g^{-1}$ vs. Ag, for a Li-ion capacitor.[110]

The long-term cycling ability of the device is shown in Figure 35. In panel a, we can see an initial decrease in capacity for the first 50 cycles, which can be associated with initial irreversibility. This irreversibility does not affect the remarkable stability of the device that shows 93% of capacity retention over 10000 cycles. Furthermore, as reported in panel b, an average specific energy of ~27 mWh $g^{-1}$ is maintained without any loss over the 10000 cycles, with a gradually improving energy efficiency (~80%). This remarkable stability is one of the best performances reported in literature for hybrid Li-ion capacitors.[7,125–127]. The high energy stability is connected to a gradual shift of the plateau to higher potentials during cycling, as shown in Figure 35c. It seems that a balancing effect is taking place, where the progressive reduction of the specific capacity, as electrode degradation proceeds, is balanced by the translation of both cathodic and anodic plateaus to higher potentials. The change was still present when the cell was tested after one month resting. It should be noted that, to maintain stable performance, pre-lithiation of the negative electrode is typically necessary.[128] Thanks to the balancing effect, our system does not need the pre-lithiation step.

*Figure 35: GCD performance of Li-ion capacitors: (a) capacity and coulombic efficiency vs. number of cycles; (b) energy and energy efficiency vs. number of cycles; (c) GCD potential vs. capacity reported for the $1^{st}$, $50^{th}$, $500^{t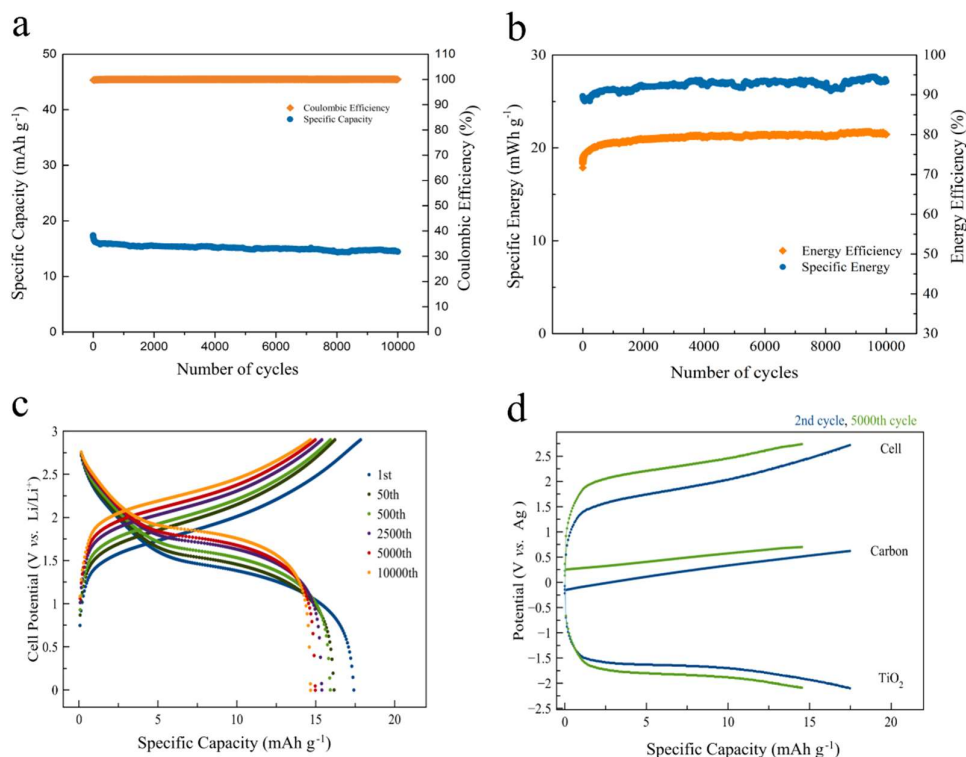h}$, $2500^{th}$, $5000^{th}$, $10000^{th}$ cycles; (d) potential shift between the $2^{nd}$ and $5000^{th}$ cycle evaluated in a three-electrode configuration vs. Ag.*[110]

Further analysis with GCD in the three-electrode configuration, see Figure 35d, reveals that both the carbon electrode and the titania electrode are characterized by higher overpotentials during cycling. The TEM micrographs in Figure 36 helps elucidating the change happening at the titania electrode. During cycling, cubic $LiTiO_2$ nanocrystals form at the surface of the mesoporous beads with dimension less than 5 nm. This phase is different from the tetragonal $LiTiO_2$ formed during the reversible insertion of Li ions in titania. Rock salt $LiTiO_2$ has been reported for amorphous, as in section 4.3.1, and for the rutile phase, but never for anatase. The formation of the cubic lithium titanate seems to affect the kinetics of the reversible lithium insertion, inducing a higher overpotential. This effect is similar to the overpotential shift shown when charging titania at a high rate, due to the formation of the tetragonal lithium titanate on the surface of the material and subsequent hindrance of the lithium diffusion toward the inner parts of the material. Moreover, the onset of the lithium-rich titanate is probably the main responsible for the capacity decrease during cycling, as both titanium and lithium atoms become unavailable for the reversible redox processes. This is in agreement with the synergic development of both the plateau shifts and capacity decrease.
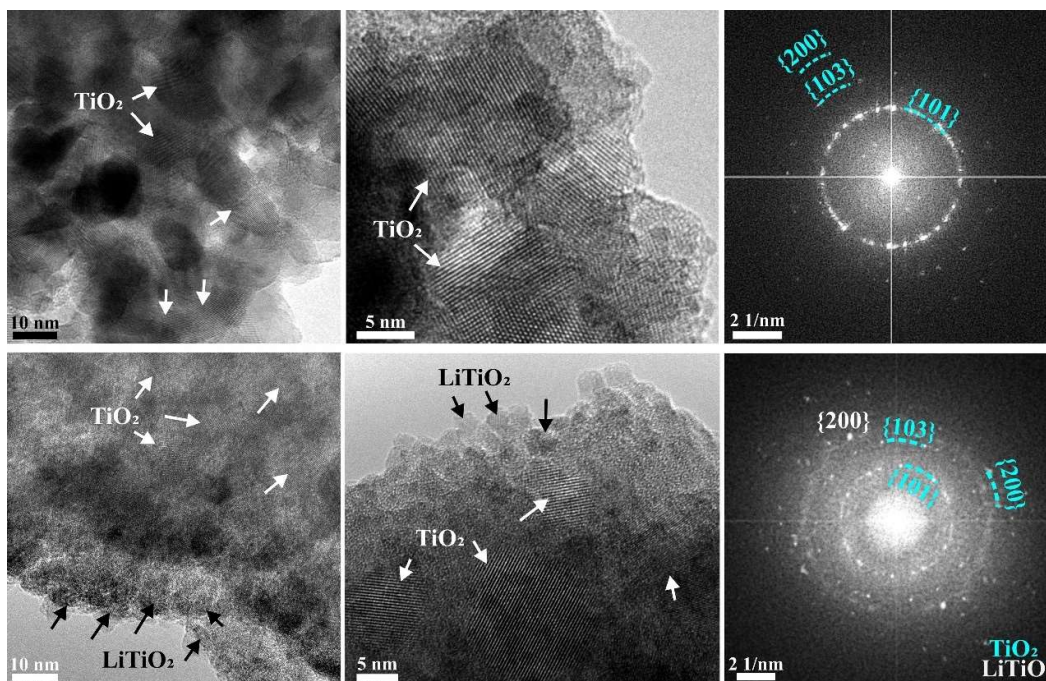
***Figure 36****: TEM images of the titania electrodes in the Li-ion capacitor with the relevant lattice fringes. The first row represents the TiO₂ material before cycling, while the second row shows the formation of LiTiO₂ nanocrystals on the TiO₂ surface for the post-mortem electrode.*[110]

The cycling at different rates and the energy density *vs.* the power density performance (Ragone Plot) are shown in Figure 37. The plot reports the gravimetric densities, measured with respect to the total mass of the electrodes. Our supercapacitor delivers 37 Wh kg$^{-1}$ at 0.5 A g$^{-1}$ (100 W kg$^{-1}$) and it is still providing ~10 Wh kg$^{-1}$ at the very high current of 20 A g$^{-1}$ (3 kW kg$^{-1}$).
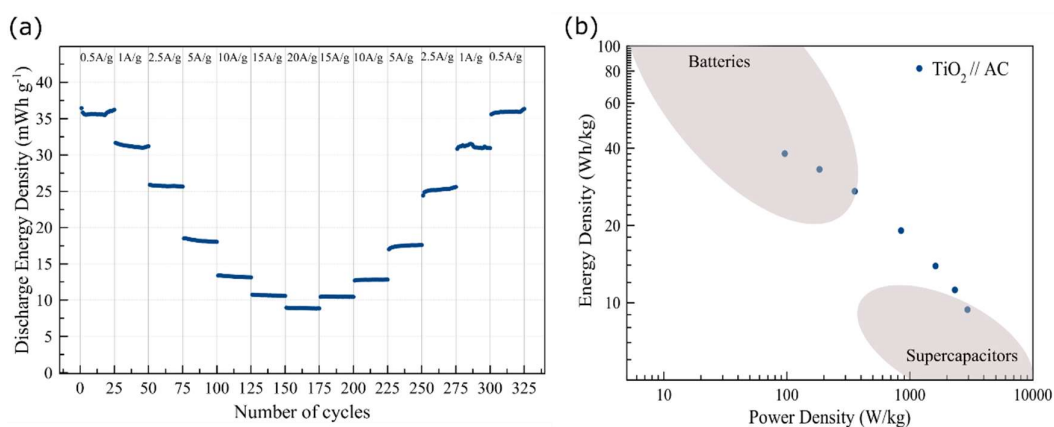


***Figure 37****: (a) Rate performance of the asymmetric supercapacitor and (b) Ragone plot reported in terms of the mass of the electrodes.*[110]

# 5.    Mesoporous Carbons for High Rate Energy Storage

## 5.1    Background

In this chapter, ordered mesoporous carbons are investigated as active materials for electrochemical energy storage. The findings reported here are connected to **Paper V** and **Paper VI**. The first paragraph introduces carbon and its peculiar properties, followed by a brief account on the use of carbon materials for energy storage. In paragraph 5.2, the synthesis, electrode and device preparations utilized in this work are presented. Finally, paragraph 5.3 deals with experimental results and interpretations.

### *5.1.1    Carbon: a Unique Element*

Carbon has been known to humanity since ancient times when it was used as charcoal to produce heat. In modern times, scientists realized that carbon is the fundamental ingredient of life, the main constituent of all living organisms. This incredible role comes from the unique ability of this element to form bonds with itself and many other elements. Depending on the type of bonding, different allotropes can be found, ranging from the friable opaque graphite to the hard and transparent diamond. Because of the huge variety of binding partners and interactions, researchers allocated an entire scientific branch to it, the organic chemistry. Figure 38 shows some of the most famous carbon allotropes.[129]
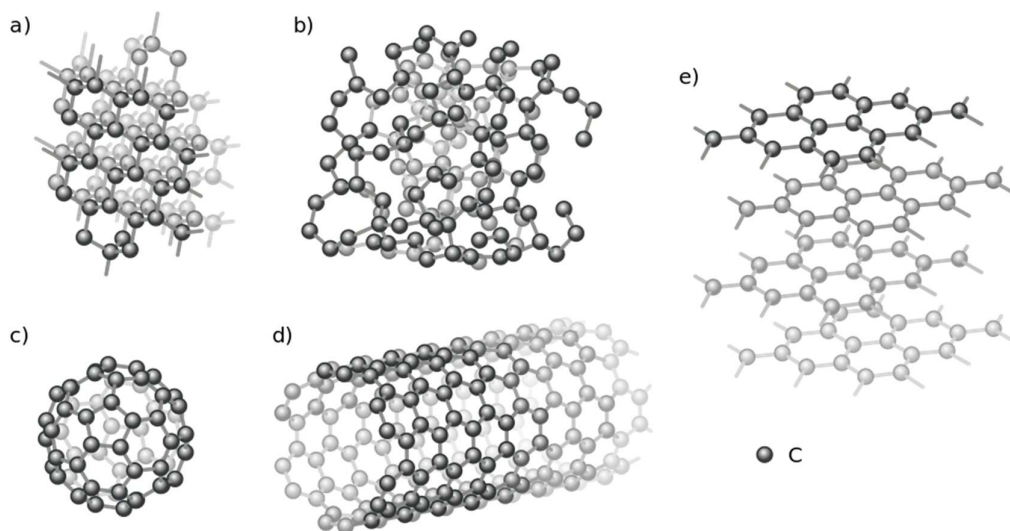


*Figure 38: Carbon allotropes a) diamond, b) amorphous carbon, c) fullerene, d) carbon nanotube, e) graphite (a single layer is called graphene).*

Carbon can be bound to up to four other atoms. When it forms four single bonds (no electron lone pairs), then it is said to be $sp^3$ hybridized, with tetrahedral symmetry. When the carbon atom is bound to three atoms (two single bonds, one double bond), the hybridization is $sp^2$, with a flat trigonal or triangular arrangement with angles ~120° between the carbon atom and two binding partners. Finally, the sp hybridization is obtained when a carbon atom is bound to two atoms (two double bonds or one single bond + one triple bond). Six $sp^2$ carbon atoms organized in a ring are so-called aromatic and have a very important role in both

organic and inorganic matter. Carbon can form structures with $sp^2$ or a combination of $sp^3$ and $sp^2$ hybridizations, showing electron delocalization. Thanks to the delocalization of the electrons, honeycomb-like carbon structures are characterized by electrical conductivity. For example, graphene, a single atom thick layer of $sp^2$ hybridized carbon atoms, shows a crystal structure with the highest measured electrical conductivity and Young modulus. Amorphous carbon, instead, is characterized by a mixture of $sp^2$ and $sp^3$ hybridized carbon atoms, showing almost no crystal order and relatively lower electrical conductivity. Its tunable properties make it a candidate for extensive research in the energy field.[130]

### 5.1.2 Carbon Materials for Electrochemical Energy Storage (EES)

Carbon materials have attracted the interest of EES researchers due to the low cost, high abundance, environmental friendliness, non-toxicity and relatively high electronic conductivity. As reported in section 2.2.1, graphite is the material of choice as anode for lithium-ion batteries. It intercalates lithium-ions in between its graphitic planes to reach the stoichiometry $LiC_6$, corresponding to a theoretical capacity of 372 mAh $g^{-1}$.[131] To increase the specific capacity and rate performance of the anodes, other allotropes of carbon have been studied, like carbon nanofibers and nanotubes, graphene and carbon nanospheres.[132–135] Functionalization/doping of carbon materials, like nitrogen doping, has been used to improve their electrochemical performance. Specifically, nitrogen doping contributes with electrons to the graphitic carbon layer, inducing donor states near the Fermi level.[136] Moreover, the nitrogen defects introduced with doping have low energy barrier for Li insertion and adsorption, allowing for higher specific capacities.[137]

On the other hand, carbon materials in different forms have been used also for supercapacitor applications. They are widely used because of their low cost and versatile forms such as powders, fibres, foils, composites and monoliths. As described in section 2.3.1, to maximize the storable charge in the form of a double layer, the materials require high surface areas and pore dimensions similar to the size of ions.[138] Activated carbons, with high surface areas, are the most used electrode materials. In addition, the capacitance can be enhanced by the presence of heteroatoms in the carbon network, most commonly oxygen and nitrogen. It has been shown that they give rise to stable pseudo-Faradaic reactions.[34] Other interesting materials for supercapacitors are carbon nanotubes and graphene.[139]

### 5.1.3 Mesoporous Carbons and Their Use in Electrochemical Energy Storage

In the past 20 years, mesoporous carbon-based electrodes have gained interest as alternative anodes in lithium-ion batteries. Among these materials, ordered mesoporous carbons (OMCs), prepared via a hard-templating method, show high surface areas, large pore volumes, uniform pore size distribution and ordered interconnections. Thanks to these properties, OMCs, some of which are called CMK-n depending on the template used in the synthesis, are characterized by short pathways for Li-ion diffusion, providing high capacities and good rate performance.[140]

CMK-3 carbons, synthesized from the hexagonal ordered SBA-15 silica, are the most studied materials of this class. On the other hand, CMK-8 carbons, prepared from cubic ordered KIT-6 silica, has received less attention, even though their interpenetrating 3D

network of channels is a desirable feature for fast Li-ions diffusion.[141] Figure 39 reports the voltage profile as a function of capacity for a CMK-8 carbon and the capacity stability with cycling in half cell measurements *vs.* Li.
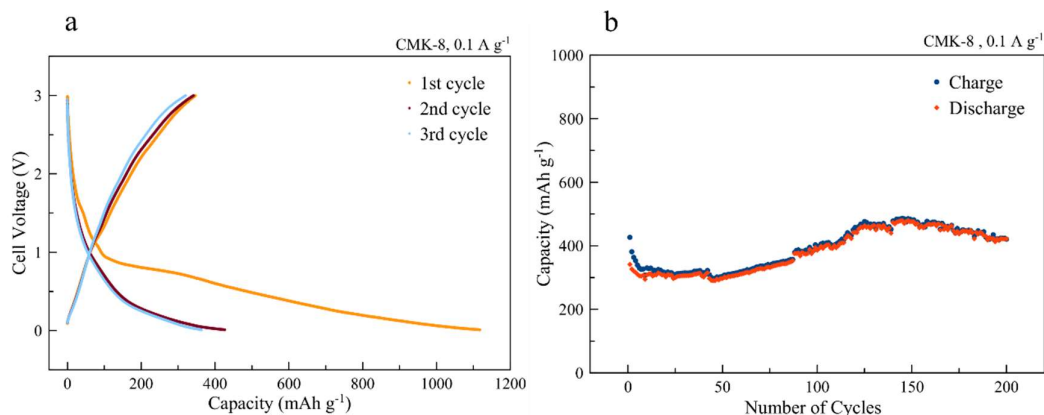


***Figure 39***: *a) Galvanostatic charging/discharging curves and b) specific capacity vs. number of cycles for a CMK-8 (a) (see synthesis in section 5.2.1) electrode studied in half cell vs. Li.*[142]

Figure 39a depicts a very high irreversible charging capacity between the first and second cycle. This irreversibility is connected to the extended plateau starting at around 1V in the first cycle, which is associated to the electrolyte decomposition at the surface of the active material and formation of a solid electrolyte interface (SEI). The presence of edges and defects in high surface area materials provides many sites for the electrolyte decomposition, which explains the large capacity loss. However, the surface defects act also as lithium insertion sites, increasing the theoretical specific capacity to a higher value than the graphite (372 mAh g$^{-1}$). In Figure 39b the increase in capacity, after the initial 10 cycles of irreversibility, has been suggested to be related to the infiltration of electrolyte inside the mesopores of the material as cycling proceeds. The use of mesoporous carbons as anode in lithium ion batteries is the topic of **Paper V**.

Porous activated carbons are the most used materials in electrochemical capacitors. The pore size of these carbon materials can be controlled, by changing the precursor and activation method used during preparation. The parameters of the activation process such as temperature, time, type of activating agent, affect significantly the microporosity of the resulting carbons.[143] However, the most suitable method for controlling the pore size and porosity of the carbons is the template method.[144] Even though it is a relatively expensive technique, it has resulted in great progress in the development of capacitor performance. Notably, it confirms the role of small mesopores and their interconnectivity for fast charge propagation, and also shows the significant effect of micropores for the accumulation of charges.[145,146] Figure 40 shows the typical rectangular shape of a CV curve for a CMK-8 carbon electrode in 0.5 M NaSO$_4$, similar to the ones used in **Paper VI**.
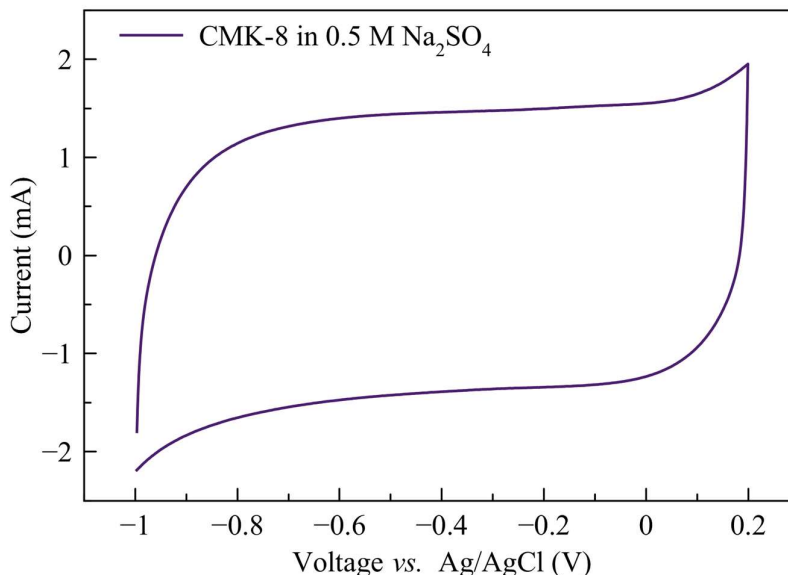
***Figure 40****: Cyclic voltammetry curve for a CMK-8 electrode in 0.5 M Na₂SO₄ at 5 mV s⁻¹.*

When dealing with redox enhanced ECs, mesoporous carbons with high surface areas are chosen because they provide a high number of active sites for the electron transfer reactions. Moreover, by confining the redox species in their pores, the porous carbons can help mitigate the self-discharge issues without using expensive ionic membranes. For example, research has focused on the adsorption of halide ions like iodide and bromide inside the micropores of activated carbons.[69] Bromide-based electrolytes have been extensively studied thanks to their low cost, high solubility and redox activity.[68,147] Stucky et al. have demonstrated a reduced self-discharge in devices based on the pentyl viologen (PV) and bromide couple thanks to the reversible counterion-induced solid complexation inside the pores of their activated carbon electrodes.[109,148] They proposed a reaction scheme for the two redox species, also including the formation of adsorbed complexes. At the positive electrode, the Br⁻ follows the scheme:

$2\ Br^- \leftrightarrow Br_2 + 2\ e^-$

$Br_2 + Br^- \leftrightarrow Br_3^-$

$2\ Br_3^- + PV^{2+} \leftrightarrow [PV^{2+} \cdot 2\ Br_3^-]_{ads}$
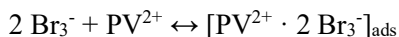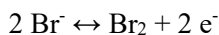
While at the negative electrode the pentyl viologen undergoes the reactions:

$PV^{2+} + e^- \leftrightarrow PV^{+\cdot}$

$PV^{+\cdot} + Br^- \leftrightarrow [PV^{+\cdot} \cdot Br^-]_{ads}$
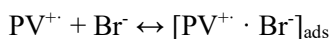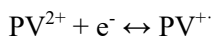
The pentyl viologen / bromide system was studied more in depth with the use of ordered mesoporous carbons in **Paper VI**.

## 5.2 Mesoporous Carbon Synthesis, Electrode Preparation and Use in Devices

### 5.2.1 Synthesis of Ordered Mesoporous Carbon via Hard-templating Method

In **Paper V** and **VI**, ordered mesoporous carbons of type CMK-8 were produced using ordered mesoporous KIT-6 silica as a hard template. KIT-6 was produced in an acidic aqueous solution using a mixture of the triblock copolymer Pluronic™ P123 ($EO_{20}PO_{70}EO_{20}$, $M_W$: 5800 g/mol), butanol and tetraethoxysilane (TEOS). All chemicals were purchased from Sigma Aldrich. P123 (36 g) was mixed in 1302 mL of MilliQ water and 60 mL hydrochloric acid (HCl) under stirring at 35 °C. When the solution became completely transparent, 44.4 mL of butanol was added. After 1 h, 77.4 g of TEOS was added and the solution was first left under stirring for 24 h and subsequently in closed propylene bottles at 35 °C or 100 °C for 24 h under static conditions. The temperature of the hydrothermal step influences the pore size distribution, with the lower temperature resulting in the smallest pores. After filtration, the product was calcined at 550 °C for 10 h to remove organic compounds. The resulting materials were named KIT-6 35°C and KIT-6 100°C, depending on the temperature of the hydrothermal step.

Furfuryl alcohol (Sigma Aldrich) was used as a carbon precursor for the synthesis of CMK-8. Silica (KIT-6, 2g) was impregnated with 2 mL of precursor (the exact quantity depends on the mesopore volume of the KIT-6 determined with the BJH (Barret-Joyner-Halenda) method. First, a polymerization process was carried out in air atmosphere at 100 °C for 2 h. The resulting material was further impregnated with half the amount of precursor and polymerized under air at 160 °C for 2 h. Pyrolysis was then performed under $N_2$ flow at 950 °C for 2 h. Finally, the silica template was removed by washing in 1:1 MilliQ water and ethanol solution containing 2 M NaOH.

The different temperatures used in the production of the silica affect the mesophase order of the final carbon material. In Figure 41, the SAXS pattern for a CMK-8 from KIT-6 35°C (a) and a CMK-8 carbon from KIT-6 100°C (b) are presented. The CMK-8 (b) carbon shows peaks indexed as reflections from (211), (220), (321), (400), (420) and (332) planes, consistent with the cubic space group Ia-3d. The pattern confirms the formation of highly ordered mesoporous carbon as a negative replica of cubic Ia-3d mesoporous silica (KIT-6).[144] The CMK-8 (a) carbon instead shows a somewhat different pattern, with peaks indexed as reflections from (110), (211), (220), (222), (321) and (400) planes. The appearance of the (110) and the small (222) peaks suggests the existence of a large fraction of displaced or uncoupled gyroidal sub-frameworks, and a lower level of symmetry, consistent with the tetragonal space group I41/a. This mesophase transition is associated with a process of strain relaxation upon silica removal.[149–151] The absence of a significant (110) peak in the CMK-8 (b) pattern shows that the material is dominated by the undisplaced double gyroidal frameworks with Ia-3d symmetry, but the minute (110) peak visible indicates the presence of a small fraction of a lower symmetry mesophase. The CMK-8 (b) keeps the Ia-3d symmetry thanks to the presence of complementary pores in the KIT-6 silica produced at 373 K, which connect the enantiomeric pair of 3D mesoporous channel systems. Upon pyrolysis of the carbon precursor, rigidly interconnecting carbon bridges avoid the structure displacement during silica removal. For CMK-8 (a), the starting KIT-6 silica was synthesized at 308 K, where no complementary pores are typically formed. For this reason, the two carbon sub-frameworks produced during pyrolysis with this silica are displaced upon silica removal and the structure transforms from the body-centered cubic Ia-3d to the body-centered tetragonal I41/a.
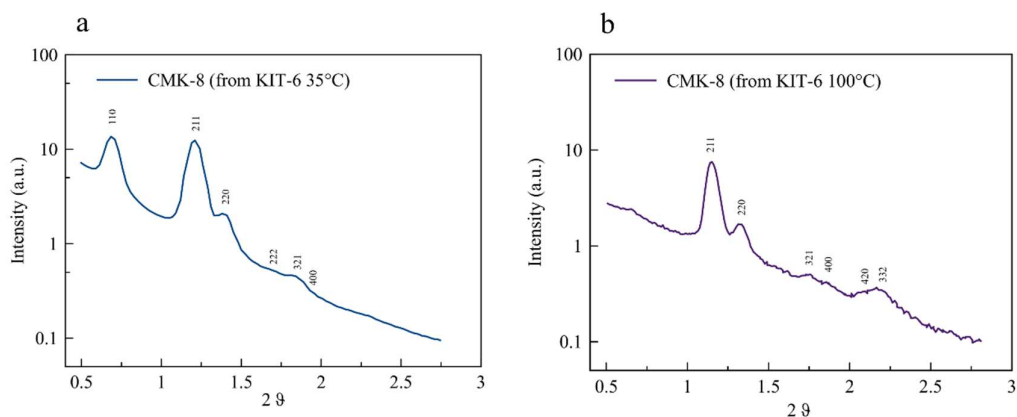
*Figure 41: SAXS patterns and Miller indices for (a) CMK-8 from KIT-6 35 °C and (b) CMK-8 from KIT-6 100 °C.*

### 5.2.2 Preparation of Electrodes and Devices for Li-ion Batteries

In **Paper V**, electrodes were prepared by mixing mesoporous CMK-8 or N-CMK-8 with carbon black, Super P™ (Alfa Aesar), and Kynar® PVDF binder (Arkema) in NMP (N-methyl-2-pyrrolidone, anhydrous, 99.5%, Sigma Aldrich). The mixture was transferred to a glass vial and Super-P™ and Kynar® 5% (w/w) solution in NMP were added. The solution was stirred overnight in a capped vial, forming a slurry having a weight ratio of (CMK-8/N-CMK-8: Super-P: PVDF) of (8:1:1). The slurry was coated onto a copper foil with a TQC AB3400 motorized automatic film applicator. A stainless-steel doctor blade (Wellcos Co.) was used to obtain a 250 μm thick coating of the slurry. The electrode sheets were dried for one day at ambient conditions in a fume hood, followed by drying in a vacuum oven at 80 °C and 20 mbar for 2 h.

The electrochemical response of the CMK-8 and N-CMK-8 materials was tested as an anode in a Li-ion half-cell. The electrodes (~10 mm diameter, 2.5 mg cm$^{-2}$ active material) were transferred to a glove box ($H_2O$ and $O_2$ less than 1 ppm) and dried under vacuum at 80 °C in a Buchi oven. Coin cells were assembled in an argon-filled glovebox using CR2032 housings. Glass microfiber (Sigma Aldrich) was used as the separator, soaked with 30 μL of commercial electrolyte LP30 (Sigma Aldrich) while a lithium metal disc was used as anode (diameter 11 mm, areal density 4 mg cm$^{-2}$). Galvanostatic charge-discharge tests were performed between 0.01 V to 2.9 V using a Scribner 580 battery cycler. The full cells were prepared using the N-CMK-8 anode with a commercial LFP ($LiFePO_4$) cathode material. The lithium-ion cell was assembled and properly balanced by a positive/negative capacity ratio of 1:1. The mass loading of the carbon electrodes was about 1.5 mg cm$^{-2}$.

### 5.2.3 Preparation of Electrodes and Devices for Redox-enhanced Electrochemical Capacitors

In **Paper VI**, free standing carbon electrodes were produced following a previously published recipe.[109] 56 mg of polytetrafluoroethylene (PTFE) binder (60 wt.% aqueous dispersion), 33 mg of acetylene black conductive additive (Vulcan® XC72R), and 4 mL isopropanol were mixed in a 10 mL cup for 2 minutes on a vortex mixer followed by 5

minutes in a Silent Crusher mixer at 2000 rpm. Next, 600 mg of activated carbon was added to the resulting slurry and the mixing steps were repeated. The resulting material was rolled with a PTFE rolling pin and folded over itself 5-10 times until a single freestanding film was formed. This film was dried overnight at 160 °C in air, ground into a powder through a mesh sieve, and then dried again under high vacuum at room temperature. The resulting electrode material contained activated carbon, carbon black conductive additive, and PTFE binder in a 90:5:5 mass ratio, respectively. Freestanding 10 mg electrode pellets were pressed from the powder in a die (MTI Corporation) on a hydraulic press (International Crystal Laboratories) under an applied uniaxial force of 2 tons, applied 3 times. Electrodes were 10 mm in diameter and $300 \pm 5$ µm thick and had an area mass loading of 12.7 mg/cm$^2$.

Cell bodies were formed by boring out the centre of Swagelok PFA Unions. Current collectors were formed by bonding 3-mm-thick type 1 glassy carbon discs (Alfa Aesar) to the ends of 12 mm diameter stainless steel rods with silver epoxy (CW2400 - Chemtronics), and encapsulating the sides of the disc and rod in electrically insulating and chemically protective epoxy (Stycast 1266 – Emmerson and Cumming). For the two-electrode cells, the cell-stack was placed between the two glassy-carbon capped current collectors inside the cell body. To build each cell-stack, two carbon electrodes were placed in a glass cup and immersed in 1.5 mL of electrolyte, composed of 1 M PVBr$_2$ and 3 M NaBr. To infiltrate the electrodes with the electrolyte, first 30 minutes of vacuum in dry condition was applied, then the electrolyte was added, and vacuum and nitrogen were alternately applied for 5 minutes intervals, several times. Electrodes were removed from the excess electrolyte and assembled into a cell stack by placing them on either side of an electrolyte-wetted 12 mm diameter filter paper (Whatman #1). For the three-electrode configuration tests, a T-shaped Swagelok PFA union was used with an Ag/AgCl reference electrode (Metrohm) with excess electrolyte added to submerge the reference electrode frit. Two different sets of three-electrode tests were conducted. For the study regarding the performance of the cell with half-cell contributions, the electrolyte used was 1 M PVBr$_2$ and 3 M NaBr. The cell-stack was the same as in the two-electrode cells. For the fundamental studies on the viologen reaction, the electrolyte was PVBr$_2$ in different concentrations (10 mM, 100 mM and 1 M) with 0.5 M Na$_2$SO$_4$ as supporting electrolyte. The cell-stack was composed of a working electrode of 10 mm in diameter and an oversized counter electrode (12 mm diameter and 15 mg) to avoid charge limitations from this side of the cell.

## 5.3   CMK-8 Mesoporous Carbons for High Rate Energy Storage

In section 5.1.3, the charge storage mechanisms of mesoporous carbons of CMK-8 type in both lithium-ion batteries and hybrid supercapacitors conditions were presented. Our research interest focused on:

- Studying the effect of nitrogen doping of CMK-8 carbons on the lithium-ion storage and the rate capability (**Paper V**).
- Using the ordered porous carbons as test materials to better understand the dual redox processes in redox enhanced electrochemical capacitors (**Paper VI**).

### 5.3.1 Nitrogen-doped Ordered Mesoporous Carbons for Lithium-ion Storage

N-doped CMK-8 was synthesised via hard templating method using silica KIT-6 100 °C, as described in section 5.2.1. Before testing the electrochemical performance, the material was structurally investigated. Figure 42 reports the BJH pore size distribution, the SAXS pattern and the XPS spectra. The carbon has a BET specific surface area of 970 $m^2$/g and is characterized by a trimodal porosity with three distribution peaks, the first at 4.2 nm, the second at 6.2 nm and the third at 9.2 nm. The SAXS pattern shows the presence of the (110) peak, suggesting the existence of a large fraction of displaced subdomains with a lower level of symmetry (I41/a, with respect to the cubic Ia-3d), as explained in section 5.2.1. The trimodal porosity seems to be associated with the symmetry modification. The first peak (4.2 nm) is related to the undisplaced Ia-3d domain. The structural displacements upon silica removal likely induce a distortion of the pores and the appearance of the second and third peak (6.2 nm and 9.2 nm).

XPS was used to analyse the binding character of the nitrogen heteroatoms in the N-CMK-8 material and the XPS spectra for the N-CMK-8 are reported in Figure 42c to f. The three main peaks of the survey spectrum correspond to C 1s, O 1s and N 1s, with a relative surface elemental composition of 81.2%, 12.2% and 6.4%, respectively. The C 1s peak can be deconvoluted in three different components. The main peak at 284.4 eV is associated with $sp^2$ hybridized carbon or graphitic carbon. The peak at 285.7 eV is related to the bonding between carbon and nitrogen, indicating an N-$sp^2$ C bond. The third broad peak centred at 286.8 eV is not as readily identifiable, as it can have contributions from both N-$sp^3$ C bonds and C-O bonds. Three sub-peaks for C-O can be suggested, one at 286.3 eV for C-OH, one at 287.5 eV for C=O and the last at 288.5 eV associated with carboxylic groups.[152] Therefore, the carbon atoms constitute a honeycomb structure, which is modified by the nitrogen and oxygen incorporation. The high-resolution N 1s peak allows a better understanding of how the nitrogen is incorporated into the structure. The peak can be deconvoluted into three main sub-peaks at 398.4 eV, 399.4 eV and 400.8 eV.[153] The first peak corresponds to pyridinic nitrogen, which substitutes a carbon atom on a C6 ring at the edge of the layer and it is bound to two $sp^2$ carbons. The second peak is associated with pyrrolic nitrogen, which substitutes a carbon atom on the C5 ring with more $sp^3$ character. These two types of nitrogen contribute with electrons to the graphitic carbon layer, inducing donor states near the Fermi level.[136] The last peak at 400.8 eV corresponds to graphitic nitrogen, substituting a graphitic carbon and forming bonds with three $sp^2$ carbons. The high-resolution O 1s peak is more complicated to describe, considering all the different contributions. We suggest a deconvolution with four sub-peaks: the first at 530.5 eV is associated to C=O in quinone; the second at 531.8 eV to oxygen in hydroxyls, ethers, C=O in esters, amides and anhydrides; the third at 533.4 eV to C-O in esters and anhydrides and contributions from carboxylic groups; and the fourth at 535.6 eV is attributed to adsorbed water.[154]
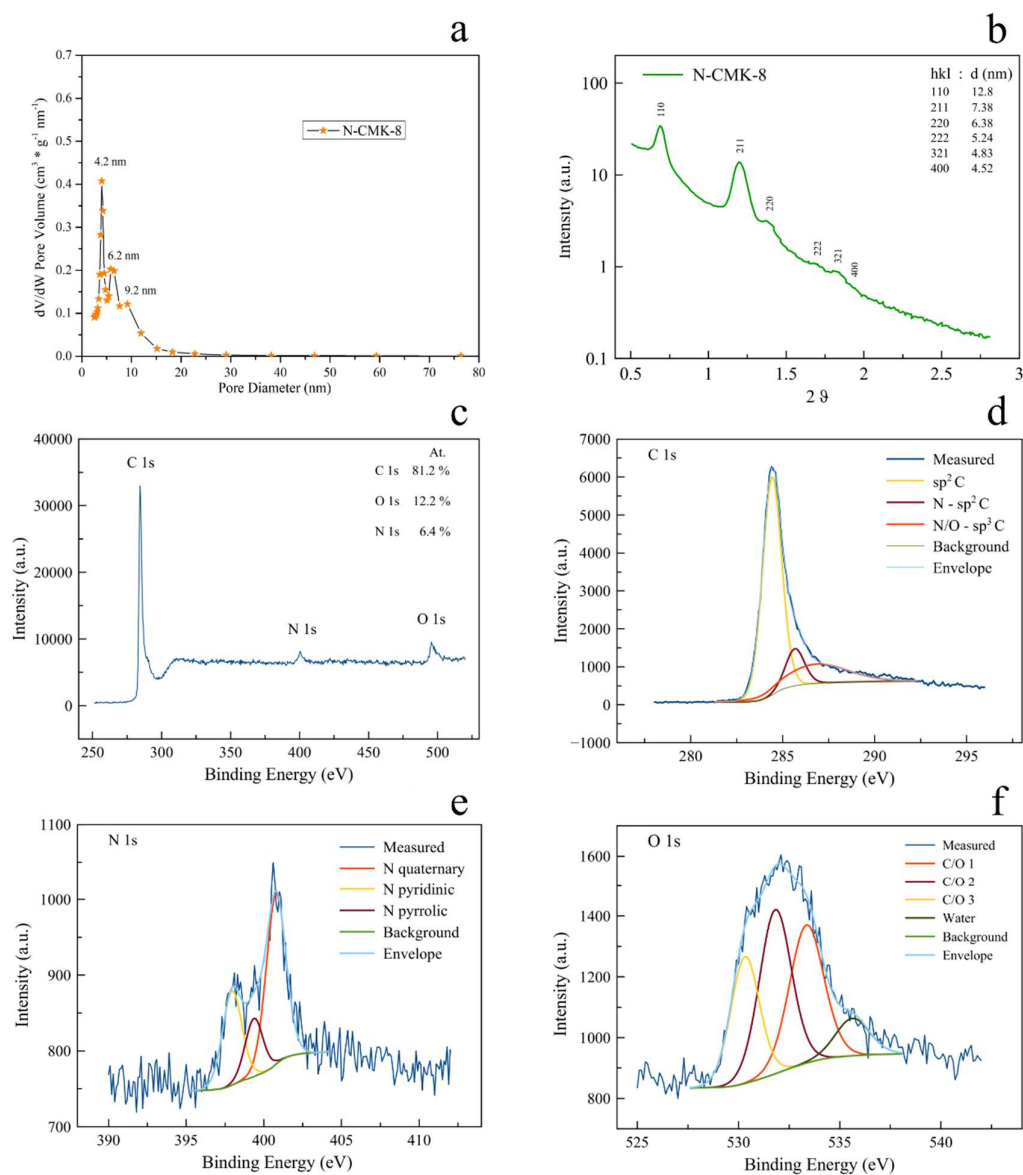
***Figure 42****: N-CMK-8 structural characterization: a) pore size distribution evaluated by BJH method from N₂ sorption isotherms; b) SAXS pattern with Miller indexed peaks; c) XPS full spectrum with relative surface elemental composition; d) high resolution C 1s peak; e) high resolution N 1s peak and f) high resolution O 1 s peak.*[142]

The ordered mesoporous carbons were studied in a half-cell configuration *vs.* Li metal. Figure 43a reports the voltage profiles *vs.* the specific capacity of the N-CMK-8. The material shows very high irreversible charging capacity associated with electrolyte decomposition at the surface of the active material and formation of a solid electrolyte interface (SEI)[155]. The presence of edges and defects in high surface area materials provides many sites for the electrolyte decomposition, which explains the large irreversible capacity. The introduction of nitrogen and formation of the pyridinic and pyrrolic sites further increases the side reactions and Li-ion trapping, resulting in an even higher irreversible capacity compared to the CMK-8 without nitrogen, see section 5.1.3. However, the presence of nitrogen has also a very beneficial effect in terms of electrochemical performance. As

seen in Figure 43a, the N-CMK-8 can reversibly store ~1000 mAh·g$^{-1}$, which is more than double than the available reversible capacity of the CMK-8. The numerous nitrogen defects at the high surface area act as Li insertion sites, enhancing the storage capability. Moreover, the low energy barrier for Li insertion and adsorption to the pyridinic and pyrrolic defects provides a higher specific capacity.[156]

Figure 43b reports the charge and discharge capacities *vs.* cycle number at 0.1 A g$^{-1}$. The N-CMK-8 shows very good reversible performance and stability for 200 cycles. The charge-discharge rate performance of the N-CMK-8 is reported in Figure 43c. The electrode shows good behaviour at high-rate, delivering ~200 mAh·g$^{-1}$ at 5 A g$^{-1}$ and showing a nearly unaltered performance when cycled again at 0.1 A g$^{-1}$. The mesoporous structure provides short diffusion paths for the Li ions penetration and a desirable high surface to volume ratio. Besides, the low adsorption energies for Li of the nitrogen functionalities presumably enhance the charge transfer reactions.

Finally, the N-CMK-8 anode was tested in combination with a LiFePO$_4$ cathode in a full cell. LiFePO$_4$ is typically used in laboratory studies as a cathode because of its environmental friendliness, but it has a lower specific capacity compared to NMC (Lithium Nickel Manganese Cobalt Oxide) cathodes used nowadays in commercial applications [157,158]. Figure 43d shows that the Li-ion cell has stable performance over 100 cycles (> 90 % capacity retention[159]) with high coulombic efficiency, demonstrating the feasibility of using nitrogen functionalized ordered mesoporous carbons as anodes for practical applications in LIBs.
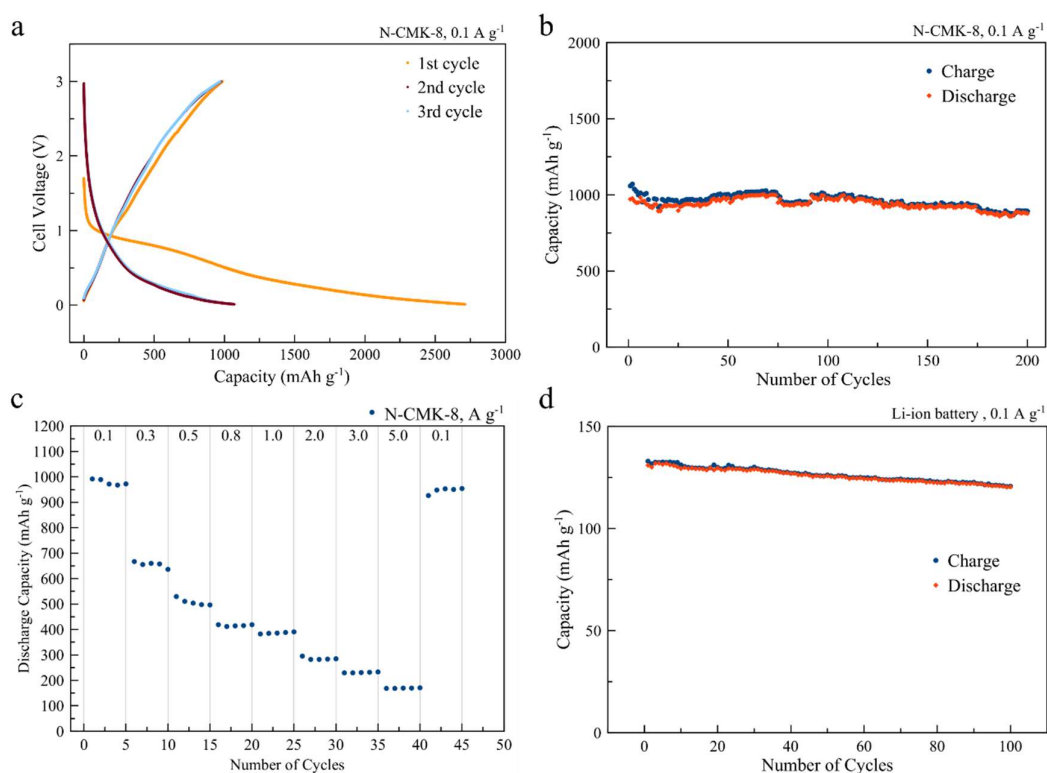


***Figure 43****: N-CMK-8 electrochemical characterization: a) voltage profiles for the 1$^{st}$, 2$^{nd}$ and 3$^{rd}$ cycles; b) stability of charge and discharge specific capacities during cycling; c) rate capability and d) specific capacity stability over 100 cycles for a Li-ion battery.*[142]

### 5.3.2  CMK-8 Carbon for Redox-enhanced Electrochemical Capacitors

CMK-8 carbon was used as active material for the conductive electrode in redox enhanced ECs based on the pentyl viologen / bromide redox couple. The cubic 3D pore structure of CMK-8 provides access from all orientations, which is desirable for efficient molecular diffusion into its pores.

To better understand the dual redox processes taking place inside the pores and improve the performance of the final device, three-electrode fundamental studies were performed at both a glassy carbon electrode and the CMK-8 carbon electrode. While the bromine electrochemistry is more known, understanding the pentyl viologen redox reaction require more focus.[160,161] Compton *et al.* studied the electrochemistry of methyl viologen and described a two-peak process with three oxidation states $MV^{2+} \leftrightarrow MV^{+} \leftrightarrow MV^{0}$ and the formation of a surface layer of $MV^{0}$.[162] Besides, it is well established that viologen molecules with large alkane groups from pentyl and upwards can produce stable films with the participation of several anions including bromide and sulphate.[163] Three-electrode cyclic voltammetry tests were performed at 5 mV s$^{-1}$ with 100 mM pentyl viologen in 0.5 M Na$_2$SO$_4$ on both the glassy carbon and CMK-8 carbon electrodes. Figure 44a reports the sweep rate dependence on glassy carbon, which indicates that the electron transfer reaction involves both dissolved and adsorbed species.
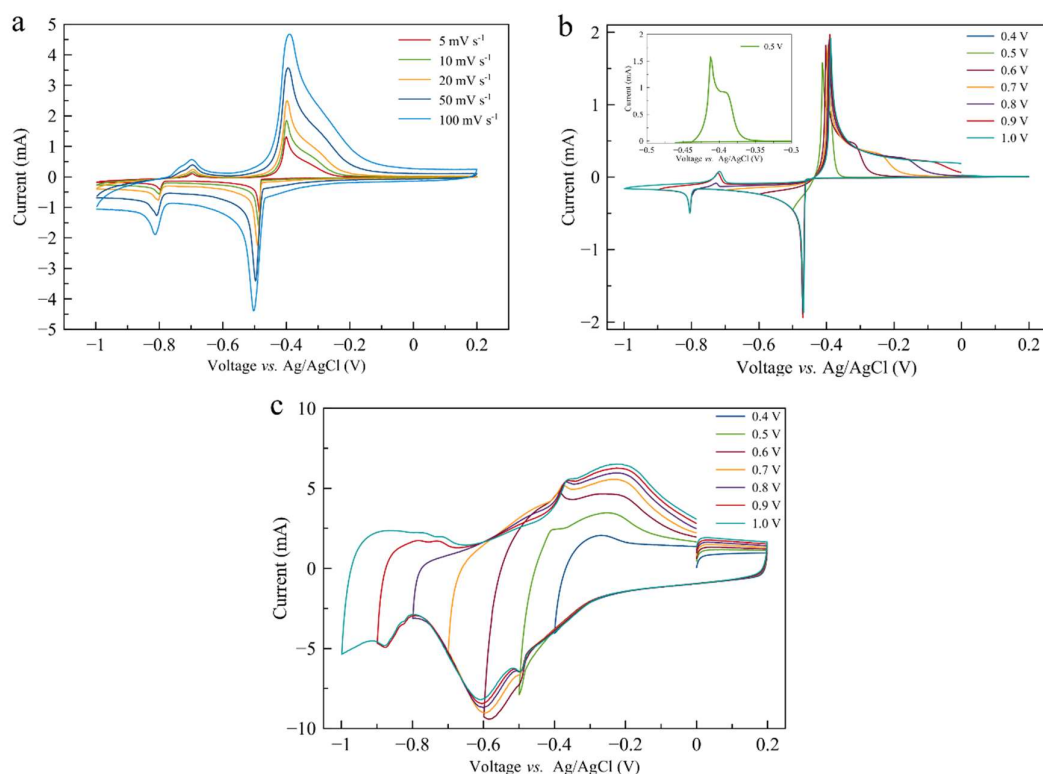


***Figure 44****: Cyclic voltammetry curves in three-electrode configuration vs. Ag/AgCl: a) sweep rate dependence; curves at 5 mV s$^{-1}$ with different switching potentials on b) a glassy carbon electrode and c) CMK-8 carbon electrode. Electrolyte: 100 mM PVBr$_2$ and 0.5 M Na$_2$SO$_4$.*

The cathodic scan shows two peaks, one at -0.5 V, resembling an adsorption peak, and the second at -0.8 V. The anodic scan shows a stripping peak on the oxidation in the potential range between -0.4 V and -0.39 V depending on sweep rate, and a shoulder peak. There is also an adsorption peak at -0.7 V less dependent on sweep rate. Following the conclusions from Compton, we propose that pentyl viologen also adsorbs on the glassy carbon surface as both $PV^+$ and $PV^0$, and the adsorbed, or deposited layer (*i.e.* more than a monolayer) is electroactive together with the reduction of species in solution at yet uncovered surfaces. To further understand the deposition process, Figure 44b reports CV curves at 5 mV s$^{-1}$. As the switching potential gets more negative, an electrodeposition process is clearly evident. When the amount of deposited material increases, the sharp oxidation peak moves to less negative potentials and the shoulder peak gets broader. This observation implies that it becomes more difficult to strip the deposited layer from the electrode. In Figure 44c, the pentyl viologen response on the CMK-8 carbon shows similar behaviour to the glassy carbon, with a combination of faradaic and adsorption phenomena. The high surface area of the material is responsible for the broad CV curve. The shape of the curve confirms that the solution process gives the biggest contribution to the charge storage, however, there exists also a contribution from adsorption. Specifically, the small peaks attached to the broad reduction and oxidation peaks indicate the electrodeposition of $PV^+$ and $PV^0$, but it seems that only a small part of the surface is subject to the layer formation. Compton *et al.* also observed that no extensive adsorption peaks were visible at gold electrodes when coated with multi walled carbon nanotubes.[162] In accordance, we suggest that, in the case of the CMK-8 highly porous carbon, the viologen adsorbs and forms a layer on the carbon particles outer surface, while in the mesopores the layer formation is hindered and the solution behaviour becomes dominant. The more negative switching potentials allow for an increase in deposition and the reduction peaks over -0.8 V. The redox activity in this potential range is probably related to electron transfer within the film. The curves show a high degree of reversibility. Therefore, the extension of the voltage window allows for a large reduction and subsequent oxidation of the pentyl viologen in $PV^+$ and $PV^0$. It should be noted that the presence of $SO_4^{2-}$ (of concentration higher than Br$^-$), which can also act as counter-ion together with Br$^-$, can influence the positions of the peaks for the viologen film formation.

Following the investigation about the pentyl viologen electrochemistry, GCPL and CV measurements were performed in a three-electrode configuration *vs.* Ag/AgCl, as reference electrode and 1 M PVBr$_2$ / 3 M NaBr electrolyte, in operating conditions resembling that of a redox-enhanced ECs. The voltage was varied between the positive and negative electrodes while the potential profiles were simultaneously recorded with respect to the reference electrode. Figure 45 shows the GCPL curves at 0.1 A g$^{-1}$ and 1 A g$^{-1}$ and CV curves at 5 mV s$^{-1}$ when different voltage limits are used (1.2 V, 1.5 V and 1.7 V).

It is clear from Figure 45a that the cell voltage limit of 1.2 V prevents the full reduction of viologen as well as the full oxidation of bromine during charging and therefore the storable charge is not fully utilized. In Figure 45d, the negative electrode shows a broad reduction peak at around -0.5 V, which becomes fully developed when the cell voltage limit increases further to 1.7 V, see Figure 45g. The anodic scan of this electrode is characterized by one peak at approximately -0.3 V, which becomes broader as the cell voltage limit increases. The positive electrode shows instead a reduction peak around 0.53 V and an oxidation peak around 0.78 V, related to the bromine system. This peak is not fully developed when the cell limit is 1.2 V, but a clear peak is observed at a cell limit of 1.5 V. Since the peak does not develop further for the limit of 1.7 V, this suggests that the difference in cell performance

between the 1.5 V and 1.7 V limits mostly relates to the negative electrode and the viologen reactions. Similarly, in the GCPL curves, the positive electrode, involving the bromine redox reaction, shows low polarization, whereas the polarization of the negative electrode (viologen redox reaction) dictates the overall cell profile. At 0.1 A g$^{-1}$ (Figure 45b, e and h) the coulombic efficiency of the cells is lower than 50%, while it is much higher at 1 A g$^{-1}$ (Figure 45c, f and i).
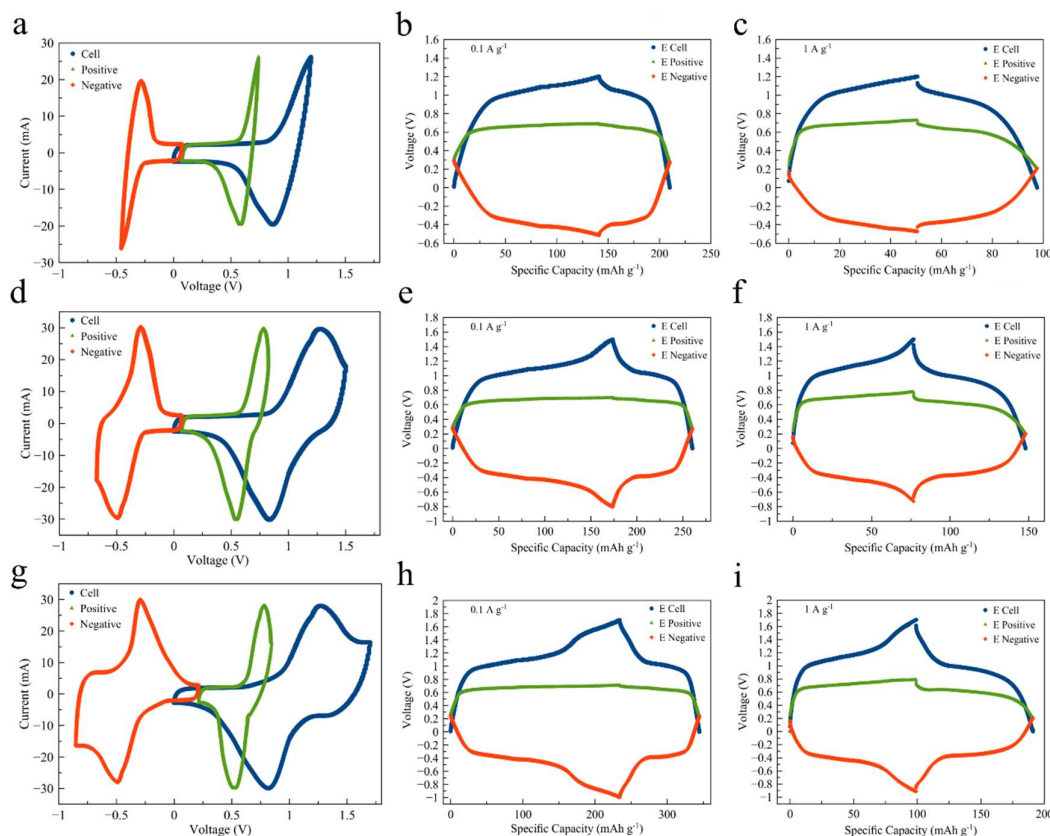


*Figure 45: Three-electrode configuration curves vs. Ag/AgCl with single electrodes contributions when different cell voltage limits are used: cyclic voltammetry curves to a) 1.2 V, d) 1.5 V and g) 1.7 V; galvanostatic charging/discharging curves at 0.1 A g$^{-1}$ to b) 1.2 V, e) 1.5 V and h) 1.7 V; galvanostatic charging/discharging curves at 1 A g$^{-1}$ to c) 1.2 V, f) 1.5 V and i) 1.7 V. Electrolyte: 1M PVBr$_2$ and 3M NaBr.*

The low efficiency at low rate can be explained by the cross-diffusion of the redox species, which becomes more relevant at low rates. Moreover, the excess volume of electrolyte used for the three-electrode configuration seems likely to facilitate the cross-diffusion. The higher reversibility of the cells at 1 A g$^{-1}$, instead, suggests a hindrance for the cross-diffusion probably due to the counterion-induced solid complexation. In addition, a second charging plateau in the negative electrode profile is gradually appearing with increasing cut-off voltage. The extent of the plateau is reduced at a higher rate due to the plateau displacement originated by the increased ohmic drop. The appearance of the plateau is matched by an increase of the discharge specific capacity at 1 A g$^{-1}$ from 49 mAh g$^{-1}_{dry}$ (45 Wh kg$^{-1}_{dry}$) at 1.2 V to 70 mAh g$^{-1}_{dry}$ (62 Wh kg$^{-1}_{dry}$) at 1.5V and to 90 mAh g$^{-1}_{dry}$ (75 Wh kg$^{-1}_{dry}$) at 1.7 V.

To evaluate the pentyl viologen / bromide in a prototype full cell, without excess electrolyte and reference electrode, GCPL tests in two-electrode configuration were performed at different rates and are reported in Figure 46. Panel a depicts the potential profile with respect to the gravimetric capacity at 0.5 A g$^{-1}$ and 5 A g$^{-1}$. At 0.5 A g$^{-1}$, the cell voltage shows an almost symmetric shape, suggesting a high degree of reversibility, with 99.9% coulombic efficiency. The initial linear increase in voltage during charge, from 0 to 0.9 V, is associated with the formation of a double layer. The subsequent plateau represents the redox reactions of the redox-active molecules happening at the electrode/electrolyte interface. At the higher rate of 5 A g$^{-1}$ test, the ohmic drop becomes more relevant and the plateaus for charging and discharging are displaced to more positive and less positive potentials, respectively. Figure 46b shows that the cell can discharge 48 Wh kg$^{-1}_{dry}$ at 0.5 A g$^{-1}$ with capacity retention > 93 % over 200 cycles and > 99.5 % coulombic efficiency. The rate performance of the cell is reported in Figure 46c. Two different sets of data are presented, referring to the charging current used. The orange points are correlated to the obtainable discharge energies when the applied charge and discharge currents were the same, while for the blue points a constant charging current of 0.5 A g$^{-1}$ was used during the rate test. The plateaus' displacements at high rates reduce the available discharge energy and energy efficiency. On the other hand, by charging at lower rate, the system has enough time to overcome the limitations for the oxidation and reduction reactions as well as for the transport to the electrode of the electrolyte's additives, resulting in improved discharge performance. Finally, the cell retained around 75 % of its energy after 6h resting time at open circuit conditions. The cell shows reasonably similar performance compared to the cells based on activated carbon from DONA used in the study by Stucky *et al.*[109]

As proved before, the extension of the voltage window affects the performance of a PV/Br cell by allowing an increased use of the viologen redox activity. To quantify this effect, Figure 46d, e and f report the discharge energy for 1000 cycles at the fast rate of 5 A g$^{-1}$, which is a target rate for this type of device. With increasing potential window, the cell delivers higher discharge energies, from about 12 Wh kg$^{-1}_{dry}$ at 1.2 V to about 20 Wh kg$^{-1}_{dry}$ at 1.5 V and to 23 Wh kg$^{-1}_{dry}$ at 1.7 V. The energy efficiency of the cell is, however, reduced along with the increase of the potential window. Moreover, the cell charged at 1.7 V shows lower stability compared to the other two, suggesting the onset of some degradation mechanism. The cell charged at 1.5 V, seems on the other hand, very stable as in the case of the 1.2 V and delivers better performance with its 20 Wh kg$^{-1}_{dry}$ and a peak power density of 2.8 kW kg$^{-1}_{dry}$. If the cell would be charged at the lower current of 0.5 A g$^{-1}$, the specific discharge energy would reach > 50 Wh kg$^{-1}_{dry}$ at similar peak power density.
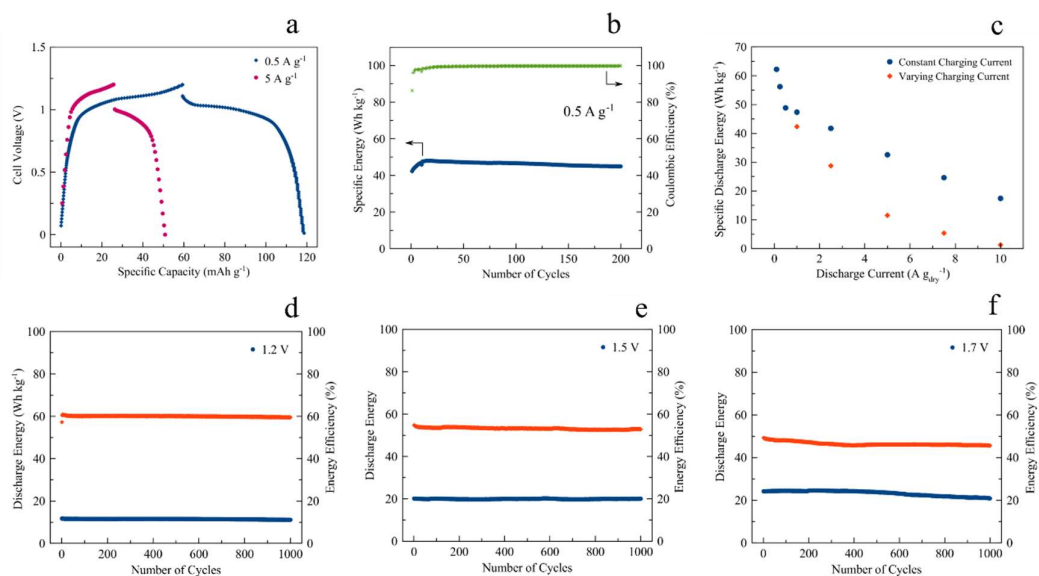
***Figure 46***: *Galvanostatic charging/discharging with potential limitations investigation of two-electrode cells: a) voltage profile at 0.5 A g⁻¹ and 5 A g⁻¹ to 1.2 V; b) specific capacity stability for 200 cycles at 0.5 A g⁻¹ and associated coulombic efficiency; c) discharge energy at 0.1, 0.2, 0.5, 1, 2.5, 5, 7.5 and 10 A g⁻¹, with constant charging current of 0.5 A g⁻¹ (blue dots) and the same charging and discharging currents (orange dots); specific discharge energy (blue) and energy efficiency (orange) at 5 A g⁻¹ to d) 1.2 V, e) 1.5 V and f) 1.7 V Electrolyte: 1M PVBr₂ and 3M NaBr.*

# 6.    Conclusions and Outlook

The charge storage mechanisms of ordered mesoporous titanium dioxide, mesoporous anatase beads and ordered mesoporous carbon materials synthetized in-house have been investigated in both lithium ion battery and hybrid supercapacitor conditions.

The ordered mesoporous titania stores a high initial capacity of 680 mAh g$^{-1}$ in the first cycle at C/2, which quickly fades to ~170 mAh g$^{-1}$ after 50 cycles. The voltage profiles show a quasi-linear relationship between potential and capacity, typical of pseudocapacitive material. The material can deliver 83 mAh g$^{-1}$ at 10C. The large irreversibility of the material was investigated by cyclic voltammetry, TEM and XAS. The CV revealed that the irreversibility occurs already at 1.7 V due to the formation of crystalline lithium titanate (LiTiO$_2$). XAS measurements showed that irreversibly and reversibly inserted lithium affect the scattering phenomena in the NEXAFS region. The material, being mainly amorphous titania, contains a high number of defects near the surface. It is suggested that the presence of such defects leads to the formation of irreversible lithium rich phases mainly located at the surface of the material.

Mesoporous anatase bead electrodes, cycled in standard organic LP30 electrolyte, showed extended plateaus in the voltage profiles, associated with the insertion of Li$^+$ ions and phase separation. Analytical calculations reveal that a high percentage of charge is stored by an extrinsic insertion pseudocapacitance. Half-cell measurements show that the electrodes deliver high specific capacities (200 mAh g$^{-1}$ at C/2), with more than 90 % capacity retention over 200 cycles and very good rate capabilities (100 mAh g$^{-1}$ at 10C). In addition, the mesoporous beads electrode was investigated as negative electrode in a hybrid asymmetric supercapacitor, with commercial activated carbon as positive electrode and LP30 as electrolyte. This configuration allowed to modify the potential window of the titania electrode to avoid a high initial capacity fade. The device delivered 37 Wh kg$^{-1}$ at 0.5 A g$^{-1}$ (100 W kg$^{-1}$) and ~10 Wh kg$^{-1}$ at the very high current of 20 A g$^{-1}$ (3 kW kg$^{-1}$). The device showed no decrease in specific energy over 10000 cycles, involving a gradual shift to higher potentials counterbalancing a gradual decrease in capacity. This effect was attributed to the formation of cubic Li$_1$TiO$_2$ at the surface of the material, as shown by TEM analysis.

Mesoporous anatase beads electrodes were doped with niobium at different concentrations (0.1, 1 and 10 at.%) and the influence of niobium doping on high-rate Li-ion storage was analysed. It is found that the Nb-doping is a substitutional process inducing donor-type levels next to the conduction band, developing a metallic-like behaviour. Moreover, computational and experimental data concluded that a 0.1 at.% doping level improves the charge transfer kinetics without interfering with the Li$^+$ insertion/desertion mechanism. The 0.1 at.% Nb-doped TiO$_2$ electrodes deliver 180 mAh g$^{-1}$ at 1C after 500 cycles and 110 mAh g$^{-1}$ at 10C after 1000 cycles. 10 at.% Nb-doping showed a deleterious effect in terms of achievable capacities. In presence of an ionic liquid electrolyte, the Nb-doped TiO$_2$ forms an SEI layer that stabilizes the performance and avoids initial capacity loss.

Nitrogen functionalized CMK-8 carbons were analysed in connection to their ability to intercalate/de-intercalate Li$^+$ ions. N$_2$ sorption showed a trimodal pore size distribution, likely a result of the structural relaxation upon silica removal during the synthesis of the material. High resolution XPS analysis confirmed the doping of the carbon framework and the presence of differently bound nitrogen atoms. These nitrogen defects have a low energy

barrier for lithium adsorption, determining an improved Li storage capability. A nitrogen doped CMK-8 electrode is able to deliver ~1000 mAh $g^{-1}$ at 0.1 A $g^{-1}$ and 200 mAh $g^{-1}$ at 5 A $g^{-1}$.

A pentyl viologen (PV)/sodium bromide (NaBr) redox-enhanced electrochemical capacitor based on ordered mesoporous carbons, of CMK-8 type, was investigated by electrochemical methods. Three-electrodes cyclic voltammetry tests were performed at 100 mM pentyl viologen in 0.5 M $Na_2SO_4$ on a glassy carbon electrode and on the CMK-8 porous carbon electrode. It is suggested that pentyl viologen adsorbs on the outer surface of the carbon particles as both $PV^+$ and $PV^0$, and the adsorbed layer is electroactive together with the reduction of solution-based species within the mesopores. Galvanostatic charging discharging curves in a three-electrode setup *vs.* Ag/AgCl show that the cells can reversibly store more charge by extending the voltage window to 1.5 V and 1.7 V. With increasing potential window, a two-electrode cell charged at 5 A $g^{-1}$ delivers increasingly higher discharge energies, from 12 Wh $kg^{-1}$ at 1.2 V to around 20 Wh $kg^{-1}$ at 1.5 V and to 23 Wh $kg^{-1}$ at 1.7 V, but at the expense of reduced energy efficiencies. A two-electrode cell charged to 1.5 V at 0.5 A $g^{-1}$ and discharged at 5 A $g^{-1}$, delivers > 50 Wh $kg^{-1}$ for 1000 cycles at the peak power of 2.8 kW $kg^{-1}$. Combining fundamental and applied studies allowed for a significant improvement of the performance of prototype devices.

# Acknowledgements

Thanks to my supervisor Prof. Anders Palmqvist, for trusting me 4 years and a half ago. Thanks for always being open minded about my ideas, for all the useful advices and great discussions. It has been an amazing journey!

Thanks to my co-supervisor Prof. Aleksandar Matic, for making me feel part of the KMF family and for all the opportunities and advices. Thanks to all KMF for the very nice time.

Thanks to my examiner Prof. Magnus Skoglundh for the very useful advices. Thanks to my studierektors, Prof. Hanna Härelind and Prof. Lars Nordstierna for being very supportive.

Thanks to Prof. Galen D. Stucky, Prof. Seung Joon Yoo and Dr. Brian Evanko from the University of Santa Barbara California. I have learned a lot during the time there. It has been an unforgettable experience.

Thanks to Prof. Elisabet Ahlberg for the guidance, support and scientifically passionate discussions.

Thanks to Dr. Gunnar Simonarson and Dr. Antiope Lotsari, for the patience and the successful collaboration.

A special thanks to Dr. Carmen Cavallo for being my partner in crime. We rock!

Thanks to the Diamond Division for being so diverse, interesting and funny. Thanks to all of you for the super cool time :)

Thanks to all my friends and to my family for always supporting me.

Thanks, Andrea, for your love.

# References

(1) Goal 7: Energy. *United Nations Sustainable Development*.

(2) Gur, T. M. Review of Electrical Energy Storage Technologies, Materials and Systems: Challenges and Prospects for Large-Scale Grid Storage. *Environmental Science* **2018**, 72.

(3) Kyriakopoulos, G. L.; Arabatzis, G. Electrical Energy Storage Systems in Electricity Generation: Energy Policies, Innovative Technologies, and Regulatory Regimes. *Renewable and Sustainable Energy Reviews* **2016**, *56*, 1044–1067. https://doi.org/10.1016/j.rser.2015.12.046.

(4)The Nobel Prize in Chemistry 2019 https://www.nobelprize.org/prizes/chemistry/2019/summary/ (accessed Oct 15, 2020).

(5) Tarascon, J.-M.; Armand, M. Issues and Challenges Facing Rechargeable Lithium Batteries. *Nature* **2001**, *414* (6861), 359. https://doi.org/10.1038/35104644.

(6) Simon, P.; Gogotsi, Y.; Dunn, B. Where Do Batteries End and Supercapacitors Begin? *Science* **2014**, *343* (6176), 1210–1211. https://doi.org/10.1126/science.1249625.

(7) Shao, Y.; El-Kady, M. F.; Sun, J.; Li, Y.; Zhang, Q.; Zhu, M.; Wang, H.; Dunn, B.; Kaner, R. B. Design and Mechanisms of Asymmetric Supercapacitors. *Chem. Rev.* **2018**, *118* (18), 9233–9280. https://doi.org/10.1021/acs.chemrev.8b00252.

(8) Larcher, D.; Tarascon, J.-M. Towards Greener and More Sustainable Batteries for Electrical Energy Storage. *Nature Chemistry* **2015**, *7* (1), 19–29. https://doi.org/10.1038/nchem.2085.

(9) Pomerantseva, E.; Bonaccorso, F.; Feng, X.; Cui, Y.; Gogotsi, Y. Energy Storage: The Future Enabled by Nanomaterials. *Science* **2019**, *366* (6468). https://doi.org/10.1126/science.aan8285.

(10) Li, W.; Liu, J.; Zhao, D. Mesoporous Materials for Energy Conversion and Storage Devices. *Nat Rev Mater* **2016**, *1* (6), 16023. https://doi.org/10.1038/natrevmats.2016.23.

(11) Sun, H.; Zhu, J.; Baumann, D.; Peng, L.; Xu, Y.; Shakir, I.; Huang, Y.; Duan, X. Hierarchical 3D Electrodes for Electrochemical Energy Storage. *Nature Reviews Materials* **2019**, *4* (1), 45–60. https://doi.org/10.1038/s41578-018-0069-9.

(12) Berger, T.; Monllor-Satoca, D.; Jankulovska, M.; Lana-Villarreal, T.; Gómez, R. The Electrochemistry of Nanostructured Titanium Dioxide Electrodes. *Chemphyschem* **2012**, *13* (12), 2824–2875. https://doi.org/10.1002/cphc.201200073.

(13) Pseudocapacitance: From Fundamental Understanding to High Power Energy Storage Materials | Chemical Reviews https://pubs.acs.org/doi/10.1021/acs.chemrev.0c00170 (accessed Sep 29, 2020).

(14) Gogotsi, Y.; Penner, R. M. Energy Storage in Nanomaterials – Capacitive, Pseudocapacitive, or Battery-Like? *ACS Nano* **2018**, *12* (3), 2081–2083. https://doi.org/10.1021/acsnano.8b01914.

(15) Encyclopedia of Electrochemical Power Sources | ScienceDirect https://www.sciencedirect.com/referencework/9780444527455/encyclopedia-of-electrochemical-power-sources (accessed Sep 16, 2019).

(16) Dell, R. M. Batteries: Fifty Years of Materials Development. *Solid State Ionics* **2000**, *134* (1), 139–158. https://doi.org/10.1016/S0167-2738(00)00722-0.

(17) Whittingham, M. S. Electrical Energy Storage and Intercalation Chemistry. *Science* **1976**, *192* (4244), 1126–1127.

(18) Mizushima, K.; Jones, P. C.; Wiseman, P. J.; Goodenough, J. B. LixCoO2 (0. *Materials Research Bulletin* **1980**, *15* (6), 783–789. https://doi.org/10.1016/0025-5408(80)90012-4.

(19) Yoshino, A. The Birth of the Lithium-Ion Battery. *Angewandte Chemie International Edition* **2012**, *51* (24), 5798–5800. https://doi.org/10.1002/anie.201105006.

(20) Peled, E. The Electrochemical Behavior of Alkali and Alkaline Earth Metals in Nonaqueous Battery Systems—The Solid Electrolyte Interphase Model. *J. Electrochem. Soc.* **1979**, *126* (12), 2047. https://doi.org/10.1149/1.2128859.

(21) Fong, R.; Sacken, U. von; Dahn, J. R. Studies of Lithium Intercalation into Carbons Using Nonaqueous Electrochemical Cells. *J. Electrochem. Soc.* **1990**, *137* (7), 2009. https://doi.org/10.1149/1.2086855.

(22) Nitta, N.; Wu, F.; Lee, J. T.; Yushin, G. Li-Ion Battery Materials: Present and Future. *Materials Today* **2015**, *18* (5), 252–264. https://doi.org/10.1016/j.mattod.2014.10.040.

(23) Liu, J.; Kopold, P.; van Aken, P. A.; Maier, J.; Yu, Y. Energy Storage Materials from Nature through Nanotechnology: A Sustainable Route from Reed Plants to a Silicon Anode for Lithium-Ion Batteries. *Angewandte Chemie International Edition* **2015**, *54* (33), 9632–9636. https://doi.org/10.1002/anie.201503150.

(24) Zhang, W.-M.; Hu, J.-S.; Guo, Y.-G.; Zheng, S.-F.; Zhong, L.-S.; Song, W.-G.; Wan, L.-J. Tin-Nanoparticles Encapsulated in Elastic Hollow Carbon Spheres for High-Performance Anode Material in Lithium-Ion Batteries. *Advanced Materials* **2008**, *20* (6), 1160–1165. https://doi.org/10.1002/adma.200701364.

(25) Zuo, X.; Zhu, J.; Müller-Buschbaum, P.; Cheng, Y.-J. Silicon Based Lithium-Ion Battery Anodes: A Chronicle Perspective Review. *Nano Energy* **2017**, *31*, 113–143. https://doi.org/10.1016/j.nanoen.2016.11.013.

(26) Armand, M.; Tarascon, J.-M. Building Better Batteries. *Nature* **2008**, *451*, 652–657. https://doi.org/10.1038/451652a.

(27) Battery Requirements for Future Automotive Applications. *EUCAR*, 2020.

(28) Betz, J.; Bieker, G.; Meister, P.; Placke, T.; Winter, M.; Schmuch, R. Theoretical versus Practical Energy: A Plea for More Transparency in the Energy Calculation of Different Rechargeable Battery Systems. *Advanced Energy Materials* **2019**, *9* (6), 1803170. https://doi.org/10.1002/aenm.201803170.

(29) Conway, B. E. *Electrochemical Supercapacitors: Scientific Fundamentals and Technological Applications*; Springer US, **1999**.

(30) Simon, P.; Gogotsi, Y. Materials for Electrochemical Capacitors. *Nature Materials* **2008**, *7* (11), 845–854. https://doi.org/10.1038/nmat2297.

(31) Stern, O. Zur Theorie Der Elektrolytischen Doppelschicht. *Zeitschrift für Elektrochemie und angewandte physikalische Chemie* **1924**, *30* (21–22), 508–516. https://doi.org/10.1002/bbpc.192400182.

(32) Bolt, G. H. Analysis of the Validity of the Gouy-Chapman Theory of the Electric Double Layer. *Journal of Colloid Science* **1955**, *10* (2), 206–218. https://doi.org/10.1016/0095-8522(55)90027-1.

(33) Grahame, D. C. Diffuse Double Layer Theory for Electrolytes of Unsymmetrical Valence Types. *J. Chem. Phys.* **1953**, *21* (6), 1054–1060. https://doi.org/10.1063/1.1699109.

(34) Frackowiak, E. Carbon Materials for Supercapacitor Application. *Phys. Chem. Chem. Phys.* **2007**, *9* (15), 1774–1785. https://doi.org/10.1039/B618139M.

(35) Zhong, C.; Deng, Y.; Hu, W.; Qiao, J.; Zhang, L.; Zhang, J. A Review of Electrolyte Materials and Compositions for Electrochemical Supercapacitors. *Chem. Soc. Rev.* **2015**, *44* (21), 7484–7539. https://doi.org/10.1039/C5CS00303B.

(36) Chmiola, J.; Yushin, G.; Gogotsi, Y.; Portet, C.; Simon, P.; Taberna, P. L. Anomalous Increase in Carbon Capacitance at Pore Sizes Less than 1 Nanometer. *Science* **2006**, *313* (5794), 1760–1763. https://doi.org/10.1126/science.1132195.

(37) Trasatti, S.; Buzzanca, G. Ruthenium Dioxide: A New Interesting Electrode Material. Solid State Structure and Electrochemical Behaviour. *Journal of Electroanalytical Chemistry and Interfacial Electrochemistry* **1971**, *29* (2), A1–A5. https://doi.org/10.1016/S0022-0728(71)80111-0.

(38) Toupin, M.; Brousse, T.; Bélanger, D. Charge Storage Mechanism of MnO2 Electrode Used in Aqueous Electrochemical Capacitor. *Chem. Mater.* **2004**, *16* (16), 3184–3190. https://doi.org/10.1021/cm049649j.

(39) Sathiya, M.; Prakash, A. S.; Ramesha, K.; Tarascon, J.; Shukla, A. K. V2O5-Anchored Carbon Nanotubes for Enhanced Electrochemical Energy Storage. *J. Am. Chem. Soc.* **2011**, *133* (40), 16291–16299. https://doi.org/10.1021/ja207285b.

(40) Come, J.; Augustyn, V.; Kim, J. W.; Rozier, P.; Taberna, P.-L.; Gogotsi, P.; Long, J. W.; Dunn, B.; Simon, P. Electrochemical Kinetics of Nanostructured Nb2O5 Electrodes. *J. Electrochem. Soc.* **2014**, *161* (5), A718. https://doi.org/10.1149/2.040405jes.

(41) Ryu, K. S.; Kim, K. M.; Park, N.-G.; Park, Y. J.; Chang, S. H. Symmetric Redox Supercapacitor with Conducting Polyaniline Electrodes. *Journal of Power Sources* **2002**, *103* (2), 305–309. https://doi.org/10.1016/S0378-7753(01)00862-X.

(42) Laforgue, A.; Simon, P.; Sarrazin, C.; Fauvarque, J.-F. Polythiophene-Based Supercapacitors. *Journal of Power Sources* **1999**, *80* (1), 142–148. https://doi.org/10.1016/S0378-7753(98)00258-4.

(43) Augustyn, V.; Come, J.; Lowe, M. A.; Kim, J. W.; Taberna, P.-L.; Tolbert, S. H.; Abruña, H. D.; Simon, P.; Dunn, B. High-Rate Electrochemical Energy Storage through $Li^+$ Intercalation Pseudocapacitance. *Nature Materials* **2013**, *12* (6), 518. https://doi.org/10.1038/nmat3601.

(44) Augustyn, V.; Simon, P.; Dunn, B. Pseudocapacitive Oxide Materials for High-Rate Electrochemical Energy Storage. *Energy Environ. Sci.* **2014**, *7* (5), 1597–1614. https://doi.org/10.1039/C3EE44164D.

(45) Opitz, M.; Yue, J.; Wallauer, J.; Smarsly, B.; Roling, B. Mechanisms of Charge Storage in Nanoparticulate TiO2 and Li4Ti5O12 Anodes: New Insights from Scan Rate-Dependent Cyclic Voltammetry. *Electrochimica Acta* **2015**, *168*, 125–132. https://doi.org/10.1016/j.electacta.2015.03.186.

(46) Okubo, M.; Hosono, E.; Kim, J.; Enomoto, M.; Kojima, N.; Kudo, T.; Zhou, H.; Honma, I. Nanosize Effect on High-Rate Li-Ion Intercalation in LiCoO2 Electrode. *J. Am. Chem. Soc.* **2007**, *129* (23), 7444–7452. https://doi.org/10.1021/ja0681927.

(47) Ruiz-Rosas, R. Design of Hybrid Asymmetric Capacitors in Aqueous Electrolyte Using ZTC and Ultraporous Activated Carbons. *Diseño de condensadores asimétricos híbridos en electrolito acuso mediante ZTC y carbones activados utraporosos* **2015**.

(48) Evanko, B.; Boettcher, S. W.; Yoo, S. J.; Stucky, G. D. Redox-Enhanced Electrochemical Capacitors: Status, Opportunity, and Best Practices for Performance Evaluation. *ACS Energy Lett.* **2017**, *2* (11), 2581–2590. https://doi.org/10.1021/acsenergylett.7b00828.

(49) Khomenko, V.; Raymundo-Piñero, E.; Frackowiak, E.; Béguin, F. High-Voltage Asymmetric Supercapacitors Operating in Aqueous Electrolyte. *Appl. Phys. A* **2006**, *82* (4), 567–573. https://doi.org/10.1007/s00339-005-3397-8.

(50) Gogotsi, Y.; Simon, P. True Performance Metrics in Electrochemical Energy Storage. *Science* **2011**, *334* (6058), 917–918. https://doi.org/10.1126/science.1213003.

(51) Li, B.; Zheng, J.; Zhang, H.; Jin, L.; Yang, D.; Lv, H.; Shen, C.; Shellikeri, A.; Zheng, Y.; Gong, R.; Zheng, J. P.; Zhang, C. Electrode Materials, Electrolytes, and Challenges in Nonaqueous Lithium-Ion Capacitors https://onlinelibrary.wiley.com/doi/abs/10.1002/adma.201705670 (accessed Jul 23, 2019). https://doi.org/10.1002/adma.201705670.

(52) Ding, J.; Hu, W.; Paek, E.; Mitlin, D. Review of Hybrid Ion Capacitors: From Aqueous to Lithium to Sodium. *Chem. Rev.* **2018**, *118* (14), 6457–6498. https://doi.org/10.1021/acs.chemrev.8b00116.

(53) Amatucci, G. G.; Badway, F.; Pasquier, A. D.; Zheng, T. An Asymmetric Hybrid Nonaqueous Energy Storage Cell. *J. Electrochem. Soc.* **2001**, *148* (8), A930. https://doi.org/10.1149/1.1383553.

(54) Lee, J.; Srimuk, P.; Fleischmann, S.; Su, X.; Hatton, T. A.; Presser, V. Redox-Electrolytes for Non-Flow Electrochemical Energy Storage: A Critical Review and Best Practice. *Progress in Materials Science* **2019**, *101*, 46–89. https://doi.org/10.1016/j.pmatsci.2018.10.005.

(55) Gorska, B.; Frackowiak, E.; Beguin, F. Redox Active Electrolytes in Carbon/Carbon Electrochemical Capacitors. *Current Opinion in Electrochemistry* **2018**, *9*, 95–105. https://doi.org/10.1016/j.coelec.2018.05.006.

(56) Frackowiak, E.; Fic, K.; Meller, M.; Lota, G. Electrochemistry Serving People and Nature: High-Energy Ecocapacitors Based on Redox-Active Electrolytes. *ChemSusChem* **2012**, *5* (7), 1181–1185. https://doi.org/10.1002/cssc.201200227.

(57) Ren, L.; Zhang, G.; Yan, Z.; Kang, L.; Xu, H.; Shi, F.; Lei, Z.; Liu, Z.-H. High Capacitive Property for Supercapacitor Using $Fe^{3+}/Fe^{2+}$ Redox Couple Additive Electrolyte. *Electrochimica Acta* **2017**, *231*, 705–712. https://doi.org/10.1016/j.electacta.2017.02.056.

(58) Abbas, Q.; Fitzek, H.; Pavlenko, V.; Gollas, B. Towards an Optimized Hybrid Electrochemical Capacitor in Iodide Based Aqueous Redox-Electrolyte: Shift of Equilibrium Potential by Electrodes Mass-Balancing. *Electrochimica Acta* **2020**, *337*, 135785. https://doi.org/10.1016/j.electacta.2020.135785.

(59) T. Senthilkumar, S.; Kalai Selvan, R.; S. Melo, J. Redox Additive/Active Electrolytes: A Novel Approach to Enhance the Performance of Supercapacitors. *Journal of Materials Chemistry A* **2013**, *1* (40), 12386–12394. https://doi.org/10.1039/C3TA11959A.

(60) Roldán, S.; Blanco, C.; Granda, M.; Menéndez, R.; Santamaría, R. Towards a Further Generation of High-Energy Carbon-Based Capacitors by Using Redox-Active Electrolytes. *Angewandte Chemie International Edition* **2011**, *50* (7), 1699–1701. https://doi.org/10.1002/anie.201006811.

(61) Lee, J.; Krüner, B.; Tolosa, A.; Sathyamoorthi, S.; Kim, D.; Choudhury, S.; Seo, K.-H.; Presser, V. Tin/Vanadium Redox Electrolyte for Battery-like Energy Storage Capacity Combined with Supercapacitor-like Power Handling. *Energy Environ. Sci.* **2016**, *9* (11), 3392–3398. https://doi.org/10.1039/C6EE00712K.

(62) Akinwolemiwa, B.; Peng, C.; Chen, G. Z. Redox Electrolytes in Supercapacitors. *J. Electrochem. Soc.* **2015**, *162* (5), A5054. https://doi.org/10.1149/2.0111505jes.

(63) Luo, H.; Wang, Y.; Wang, G.; Xiao, L.; Lu, J.; Zhuang, L. A High-Performance Dual-Redox Electrochemical Capacitor Using Stabilized $Zn^{2+}/Zn$ Anolyte and $Br_3^-/Br^-$ Catholyte. *Journal of Power Sources* **2019**, *436*, 226843. https://doi.org/10.1016/j.jpowsour.2019.226843.

(64) Lee, J.; Choudhury, S.; Weingarth, D.; Kim, D.; Presser, V. High Performance Hybrid Energy Storage with Potassium Ferricyanide Redox Electrolyte. *ACS Appl. Mater. Interfaces* **2016**, *8* (36), 23676–23687. https://doi.org/10.1021/acsami.6b06264.

(65) Wang, X.; Chandrabose, R. S.; Chun, S.-E.; Zhang, T.; Evanko, B.; Jian, Z.; Boettcher, S. W.; Stucky, G. D.; Ji, X. High Energy Density Aqueous Electrochemical Capacitors with a KI-KOH Electrolyte. *ACS Appl. Mater. Interfaces* **2015**, *7* (36), 19978–19985. https://doi.org/10.1021/acsami.5b04677.

(66) Platek, A.; Piwek, J.; Fic, K.; Frackowiak, E. Ageing Mechanisms in Electrochemical Capacitors with Aqueous Redox-Active Electrolytes. *Electrochimica Acta* **2019**, *311*, 211–220. https://doi.org/10.1016/j.electacta.2019.04.117.

(67) Przygocki, P.; Abbas, Q.; Babuchowska, P.; Béguin, F. Confinement of Iodides in Carbon Porosity to Prevent from Positive Electrode Oxidation in High Voltage Aqueous Hybrid Electrochemical Capacitors. *Carbon* **2017**, *125*, 391–400. https://doi.org/10.1016/j.carbon.2017.09.060.

(68) Yamazaki, S.; Ito, T.; Murakumo, Y.; Naitou, M.; Shimooka, T.; Yamagata, M.; Ishikawa, M. Hybrid Capacitors Utilizing Halogen-Based Redox Reactions at Interface between Carbon Positive Electrode and Aqueous Electrolytes. *Journal of Power Sources* **2016**, *326*, 580–586. https://doi.org/10.1016/j.jpowsour.2016.04.021.

(69) Yan, L.; Li, D.; Yan, T.; Chen, G.; Shi, L.; An, Z.; Zhang, D. Confining Redox Electrolytes in Functionalized Porous Carbon with Improved Energy Density for Supercapacitors. *ACS Appl. Mater. Interfaces* **2018**, *10* (49), 42494–42502. https://doi.org/10.1021/acsami.8b16642.

(70) Lee, J.; Srimuk, P.; Fleischmann, S.; Ridder, A.; Zeiger, M.; Presser, V. Nanoconfinement of Redox Reactions Enables Rapid Zinc Iodide Energy Storage with High Efficiency. *J. Mater. Chem. A* **2017**, *5* (24), 12520–12527. https://doi.org/10.1039/C7TA03589F.

(71) Lutterotti, L.; Vasin, R.; Wenk, H.-R. Rietveld Texture Analysis from Synchrotron Diffraction Images. I. Calibration and Basic Analysis. *Powder Diffraction* **2014**, *29* (1), 76–84. https://doi.org/10.1017/S0885715613001346.

(72) Klementiev, K.; Norén, K.; Carlson, S.; Clauss, K. G. V. S.; Persson, I. The BALDER Beamline at the MAX IV Laboratory. *J. Phys.: Conf. Ser.* **2016**, *712*, 012023. https://doi.org/10.1088/1742-6596/712/1/012023.

(73) Bard, A. J.; Faulkner, L. R. *Electrochemical Methods: Fundamentals and Applications*, 2nd ed.; Wiley: New York, 2001.

(74) Chen, X.; Mao, S. S. Titanium Dioxide Nanomaterials: Synthesis, Properties, Modifications, and Applications. *Chem. Rev.* **2007**, *107* (7), 2891–2959. https://doi.org/10.1021/cr0500535.

(75) Moellmann, J.; Ehrlich, S.; Tonner, R.; Grimme, S. A DFT-D Study of Structural and Energetic Properties of TiO2modifications. *J. Phys.: Condens. Matter* **2012**, *24* (42), 424206. https://doi.org/10.1088/0953-8984/24/42/424206.

(76) Madian, M.; Eychmüller, A.; Giebeler, L. Current Advances in TiO2-Based Nanostructure Electrodes for High Performance Lithium Ion Batteries. *Batteries* **2018**, *4* (1), 7. https://doi.org/10.3390/batteries4010007.

(77) Kavan, L.; Kratochvilová, K.; Grätzel, M. Study of Nanocrystalline TiO2 (Anatase) Electrode in the Accumulation Regime. *Journal of Electroanalytical Chemistry* **1995**, *394* (1), 93–102. https://doi.org/10.1016/0022-0728(95)03976-N.

(78) Lafont, U.; Carta, D.; Mountjoy, G.; Chadwick, A. V.; Kelder, E. M. In Situ Structural Changes upon Electrochemical Lithium Insertion in Nanosized Anatase TiO2. *J. Phys. Chem. C* **2010**, *114* (2), 1372–1378. https://doi.org/10.1021/jp908786t.

(79) Gentili, V.; Brutti, S.; Hardwick, L. J.; Armstrong, A. R.; Panero, S.; Bruce, P. G. Lithium Insertion into Anatase Nanotubes. *Chem. Mater.* **2012**, *24* (22), 4468–4476. https://doi.org/10.1021/cm302912f.

(80) Ren, Y.; Hardwick, L. J.; Bruce, P. G. Lithium Intercalation into Mesoporous Anatase with an Ordered 3D Pore Structure. *Angew. Chem. Int. Ed.* **2010**, *49* (14), 2570–2574. https://doi.org/10.1002/anie.200907099.

(81) Liu, Y.; Yang, Y. Recent Progress of TiO2-Based Anodes for Li Ion Batteries https://www.hindawi.com/journals/jnm/2016/8123652/ (accessed Jul 28, 2019). https://doi.org/10.1155/2016/8123652.

(82) Lindström, H.; Södergren, S.; Solbrand, A.; Rensmo, H.; Hjelm, J.; Hagfeldt, A.; Lindquist, S.-E. Li $^+$ Ion Insertion in TiO $_2$ (Anatase). 1. Chronoamperometry on CVD Films and Nanoporous Films. *J. Phys. Chem. B* **1997**, *101* (39), 7710–7716. https://doi.org/10.1021/jp970489r.

(83) Lindström, H.; Södergren, S.; Solbrand, A.; Rensmo, H.; Hjelm, J.; Hagfeldt, A.; Lindquist, S.-E. Li $^+$ Ion Insertion in TiO $_2$ (Anatase). 2. Voltammetry on Nanoporous Films. *J. Phys. Chem. B* **1997**, *101* (39), 7717–7722. https://doi.org/10.1021/jp970490q.

(84) Shen, K.; Chen, H.; Klaver, F.; Mulder, F. M.; Wagemaker, M. Impact of Particle Size on the Non-Equilibrium Phase Transition of Lithium-Inserted Anatase TiO2. *Chem. Mater.* **2014**, *26* (4), 1608–1615. https://doi.org/10.1021/cm4037346.

(85) Morgan, B. J.; Watson, G. W. Role of Lithium Ordering in the LixTiO2 Anatase → Titanate Phase Transition. *J. Phys. Chem. Lett.* **2011**, *2* (14), 1657–1661. https://doi.org/10.1021/jz200718e.

(86) Wagemaker, M.; Borghols, W. J. H.; Mulder, F. M. Large Impact of Particle Size on Insertion Reactions. A Case for Anatase Li $_x$ TiO $_2$. *J. Am. Chem. Soc.* **2007**, *129* (14), 4323–4327. https://doi.org/10.1021/ja067733p.

(87) Belak, A. A.; Wang, Y.; Ven, A. V. D. *Kinetics of Anatase Electrodes: The Role of Ordering, Anisotropy, and Shape Memory Effects* **2012**

(88) H. Borghols, W. J.; Lützenkirchen-Hecht, D.; Haake, U.; Eck, E. R. H. van; M. Mulder, F.; Wagemaker, M. The Electronic Structure and Ionic Diffusion of

Nanoscale LiTiO 2 Anatase. *Physical Chemistry Chemical Physics* **2009**, *11* (27), 5742–5748. https://doi.org/10.1039/B823142G.

(89) de Klerk, N. J. J.; Vasileiadis, A.; Smith, R. B.; Bazant, M. Z.; Wagemaker, M. Explaining Key Properties of Lithiation in ${\mathrm{TiO}}_{2}$-Anatase Li-Ion Battery Electrodes Using Phase-Field Modeling. *Phys. Rev. Materials* **2017**, *1* (2), 025404. https://doi.org/10.1103/PhysRevMaterials.1.025404.

(90) Madej, E.; La Mantia, F.; Mei, B.; Klink, S.; Muhler, M.; Schuhmann, W.; Ventosa, E. Reliable Benchmark Material for Anatase TiO2 in Li-Ion Batteries: On the Role of Dehydration of Commercial TiO2. *Journal of Power Sources* **2014**, *266*, 155–161. https://doi.org/10.1016/j.jpowsour.2014.05.018.

(91) Kubiak, P.; Fröschl, T.; Hüsing, N.; Hörmann, U.; Kaiser, U.; Schiller, R.; Weiss, C. K.; Landfester, K.; Wohlfahrt-Mehrens, M. TiO2 Anatase Nanoparticle Networks: Synthesis, Structure, and Electrochemical Performance. *Small* **2011**, *7* (12), 1690–1696. https://doi.org/10.1002/smll.201001943.

(92) Ventosa, E.; Madej, E.; Zampardi, G.; Mei, B.; Weide, P.; Antoni, H.; La Mantia, F.; Muhler, M.; Schuhmann, W. Solid Electrolyte Interphase (SEI) at TiO2 Electrodes in Li-Ion Batteries: Defining Apparent and Effective SEI Based on Evidence from X-Ray Photoemission Spectroscopy and Scanning Electrochemical Microscopy. *ACS Appl Mater Interfaces* **2017**, *9* (3), 3123–3130. https://doi.org/10.1021/acsami.6b13306.

(93) Zec, N.; Cvjetićanin, N.; Bešter-Rogač, M.; Vraneš, M.; Gadžurić, S. Electrochemical Performance of Anatase TiO2 Nanotube Arrays Electrode in Ionic Liquid Based Electrolyte for Lithium Ion Batteries. *J. Electrochem. Soc.* **2017**, *164* (8), H5100. https://doi.org/10.1149/2.0051708jes.

(94) Wang, J.; Polleux, J.; Lim, J.; Dunn, B. Pseudocapacitive Contributions to Electrochemical Energy Storage in TiO2 (Anatase) Nanoparticles. *J. Phys. Chem. C* **2007**, *111* (40), 14925–14931. https://doi.org/10.1021/jp074464w.

(95) Shin, J.-Y.; Joo, J. H.; Samuelis, D.; Maier, J. Oxygen-Deficient TiO2−δ Nanoparticles via Hydrogen Reduction for High Rate Capability Lithium Batteries. *Chem. Mater.* **2012**, *24* (3), 543–551. https://doi.org/10.1021/cm2031009.

(96) Petkovich, N. D.; Wilson, B. E.; Rudisill, S. G.; Stein, A. Titania–Carbon Nanocomposite Anodes for Lithium Ion Batteries— Effects of Confined Growth and Phase Synergism. *ACS Appl. Mater. Interfaces* **2014**, *6* (20), 18215–18227. https://doi.org/10.1021/am505210c.

(97) Cai, Y.; Wang, H.-E.; Zhao, X.; Huang, F.; Wang, C.; Deng, Z.; Li, Y.; Cao, G.; Su, B.-L. Walnut-like Porous Core/Shell TiO2 with Hybridized Phases Enabling Fast and Stable Lithium Storage. *ACS Appl. Mater. Interfaces* **2017**, *9* (12), 10652–10663. https://doi.org/10.1021/acsami.6b16498.

(98) Yang, S.; Feng, X.; Müllen, K. Sandwich-Like, Graphene-Based Titania Nanosheets with High Surface Area for Fast Lithium Storage. *Advanced Materials* **2011**, *23* (31), 3575–3579. https://doi.org/10.1002/adma.201101599.

(99) Liu, H.; Bi, Z.; Sun, X.-G.; Unocic, R. R.; Paranthaman, M. P.; Dai, S.; Brown, G. M. Mesoporous TiO2–B Microspheres with Superior Rate Performance for Lithium Ion Batteries. *Advanced Materials* **2011**, *23* (30), 3450–3454. https://doi.org/10.1002/adma.201100599.

(100) Moitzheim, S.; Gendt, S. D.; Vereecken, P. M. Investigation of the Li-Ion Insertion Mechanism for Amorphous and Anatase TiO2 Thin-Films. *J. Electrochem. Soc.* **2019**, *166* (2), A1–A9. https://doi.org/10.1149/2.1091816jes.

(101) Ryu, W.-H.; Nam, D.-H.; Ko, Y.-S.; Kim, R.-H.; Kwon, H.-S. Electrochemical Performance of a Smooth and Highly Ordered TiO2 Nanotube Electrode for Li-Ion Batteries. *Electrochimica Acta* **2012**, *61*, 19–24. https://doi.org/10.1016/j.electacta.2011.11.042.

(102) Borghols, W. J. H.; Lützenkirchen-Hecht, D.; Haake, U.; Chan, W.; Lafont, U.; Kelder, E. M.; Eck, E. R. H. van; Kentgens, A. P. M.; Mulder, F. M.; Wagemaker, M. Lithium Storage in Amorphous TiO2 Nanoparticles. *J. Electrochem. Soc.* **2010**, *157* (5), A582. https://doi.org/10.1149/1.3332806.

(103) Bi, Z.; Paranthaman, M. P.; Guo, B.; Unocic, R. R.; Iii, H. M. M.; Bridges, C. A.; Sun, X.-G.; Dai, S. High Performance Cr, N-Codoped Mesoporous TiO2 Microspheres for Lithium-Ion Batteries. *J. Mater. Chem. A* **2014**, *2* (6), 1818–1824. https://doi.org/10.1039/C3TA14535B.

(104) Fehse, M.; Cavaliere, S.; Lippens, P. E.; Savych, I.; Iadecola, A.; Monconduit, L.; Jones, D. J.; Rozière, J.; Fischer, F.; Tessier, C.; Stievano, L. Nb-Doped TiO2 Nanofibers for Lithium Ion Batteries. *J. Phys. Chem. C* **2013**, *117* (27), 13827–13835. https://doi.org/10.1021/jp402498p.

(105) Körner, W.; Elsässer, C. Density Functional Theory Study of Dopants in Polycrystalline TiO${}_{2}$. *Phys. Rev. B* **2011**, *83* (20), 205315. https://doi.org/10.1103/PhysRevB.83.205315.

(106) Sheppard, L. R.; Bak, T.; Nowotny, J. Electrical Properties of Niobium-Doped Titanium Dioxide. 1. Defect Disorder. *J. Phys. Chem. B* **2006**, *110* (45), 22447–22454. https://doi.org/10.1021/jp0637025.

(107) Yue, J.; Suchomski, C.; Voepel, P.; Ellinghaus, R.; Rohnke, M.; Leichtweiss, T.; Elm, M. T.; Smarsly, B. M. Mesoporous Niobium-Doped Titanium Dioxide Films from the Assembly of Crystalline Nanoparticles: Study on the Relationship between the Band Structure, Conductivity and Charge Storage Mechanism. *J. Mater. Chem. A* **2017**, *5* (5), 1978–1988. https://doi.org/10.1039/C6TA06840E.

(108) Cavallo, C.; Salleo, A.; Gozzi, D.; Di Pascasio, F.; Quaranta, S.; Panetta, R.; Latini, A. Solid Solutions of Rare Earth Cations in Mesoporous Anatase Beads and Their Performances in Dye-Sensitized Solar Cells. *Scientific Reports* **2015**, *5*, 16785. https://doi.org/10.1038/srep16785.

(109) Evanko, B.; Yoo, S. J.; Chun, S.-E.; Wang, X.; Ji, X.; Boettcher, S. W.; Stucky, G. D. Efficient Charge Storage in Dual-Redox Electrochemical Capacitors through

Reversible Counterion-Induced Solid Complexation. *J. Am. Chem. Soc.* **2016**, *138* (30), 9373–9376. https://doi.org/10.1021/jacs.6b05038.

(110) Calcagno, G.; Lotsari, A.; Dang, A.; Lindberg, S.; Palmqvist, A. E. C.; Matic, A.; Cavallo, C. Fast Charging Negative Electrodes Based on Anatase Titanium Dioxide Beads for Highly Stable Li-Ion Capacitors. *Materials Today Energy* **2020**, *16*, 100424. https://doi.org/10.1016/j.mtener.2020.100424.

(111) Henderson, G. S.; Groot, F. M. F. de; Moulton, B. J. A. X-Ray Absorption Near-Edge Structure (XANES) Spectroscopy. *Reviews in Mineralogy and Geochemistry* **2014**, *78* (1), 75–138. https://doi.org/10.2138/rmg.2014.78.3.

(112) Cabaret, D.; Bordage, A.; Juhin, A.; Arfaoui, M.; Gaudry, E. First-Principles Calculations of X-Ray Absorption Spectra at the K-Edge of 3d Transition Metals: An Electronic Structure Analysis of the Pre-Edge. *Phys. Chem. Chem. Phys.* **2010**, *12* (21), 5619–5633. https://doi.org/10.1039/B926499J.

(113) Luca, V.; Djajanti, S.; Howe, R. F. Structural and Electronic Properties of Sol−Gel Titanium Oxides Studied by X-Ray Absorption Spectroscopy. *J. Phys. Chem. B* **1998**, *102* (52), 10650–10657. https://doi.org/10.1021/jp981644k.

(114) Símonarson, G.; Calcagno, G.; Lotsari, A.; C. Palmqvist, A. E. Electrochemical and Structural Characterization of Lithiation in Spray Deposited Ordered Mesoporous Titania as an Anode for Li Ion Batteries. *RSC Advances* **2020**, *10* (34), 20279–20287. https://doi.org/10.1039/D0RA02687E.

(115) Pfanzelt, M.; Kubiak, P.; Jacke, S.; Dimesso, L.; Jaegermann, W.; Wohlfahrt-Mehrens, M. SEI Formation on TiO2 Rutile. *J. Electrochem. Soc.* **2012**, *159* (6), A809. https://doi.org/10.1149/2.085206jes.

(116) Leitzke, F. P.; Fonseca, R. O. C.; Göttlicher, J.; Steininger, R.; Jahn, S.; Prescher, C.; Lagos, M. Ti K-Edge XANES Study on the Coordination Number and Oxidation State of Titanium in Pyroxene, Olivine, Armalcolite, Ilmenite, and Silicate Glass during Mare Basalt Petrogenesis. *Contributions to Mineralogy and Petrology* **2018**, *173*, 103. https://doi.org/10.1007/s00410-018-1533-7.

(117) Jalilehvand, F. Structure of Hydrated Ions and Cyano Complexes by X-Absorption Spectroscopy. **2000**.

(118) Rehr, J. J.; Ankudinov, A. L. Progress in the Theory and Interpretation of XANES. *Coordination Chemistry Reviews* **2005**, *249* (1), 131–140. https://doi.org/10.1016/j.ccr.2004.02.014.

(119) Simonarson, G. Ö. Development of Syntheses for Nanostructured Titania and Silica, Chalmers University of Technology, 2019.

(120) Matic, A.; Lindberg, S.; Cavallo, C.; Calcagno, G.; Navarro-Suárez, A. M.; Johansson, P. Electrochemical Behaviour of Nb-Doped Anatase TiO2 Microbeads in an Ionic Liquid Electrolyte. *Batteries & Supercaps* **2020**, *n/a* (n/a). https://doi.org/10.1002/batt.202000076.

(121) Xiong, S.; Xie, K.; Blomberg, E.; Jacobsson, P.; Matic, A. Analysis of the Solid Electrolyte Interphase Formed with an Ionic Liquid Electrolyte for Lithium-Sulfur Batteries. *Journal of Power Sources* **2014**, *252*, 150–155. https://doi.org/10.1016/j.jpowsour.2013.11.119.

(122) Preibisch, Y.; Horsthemke, F.; Winter, M.; Nowak, S.; Best, A. S. Is the Cation Innocent? An Analytical Approach on the Cationic Decomposition Behavior of N-Butyl-N-Methylpyrrolidinium Bis(Trifluoromethanesulfonyl)Imide in Contact with Lithium Metal. *Chem. Mater.* **2020**, *32* (6), 2389–2398. https://doi.org/10.1021/acs.chemmater.9b04827.

(123) Kaleji, B. K.; Sarraf-Mamoory, R.; Fujishima, A. Influence of Nb Dopant on the Structural and Optical Properties of Nanocrystalline TiO2 Thin Films. *Materials Chemistry and Physics* **2012**, *132* (1), 210–215. https://doi.org/10.1016/j.matchemphys.2011.11.034.

(124) Qu, D.; Shi, H. Studies of Activated Carbons Used in Double-Layer Capacitors. *Journal of Power Sources* **1998**, *74* (1), 99–107. https://doi.org/10.1016/S0378-7753(98)00038-X.

(125) Brousse, T.; Marchand, R.; Taberna, P.-L.; Simon, P. TiO2 (B)/Activated Carbon Non-Aqueous Hybrid System for Energy Storage. *Journal of Power Sources* **2006**, *158* (1), 571–577. https://doi.org/10.1016/j.jpowsour.2005.09.020.

(126) Kim, J. H.; Choi, H. J.; Kim, H.-K.; Lee, S.-H.; Lee, Y.-H. A Hybrid Supercapacitor Fabricated with an Activated Carbon as Cathode and an Urchin-like TiO2 as Anode. *International Journal of Hydrogen Energy* **2016**, *41* (31), 13549–13556. https://doi.org/10.1016/j.ijhydene.2016.06.018.

(127) Li, S.; Wang, T.; Zhu, W.; Lian, J.; Huang, Y.; Yu, Y.-Y.; Qiu, J.; Zhao, Y.; Yong, Y.-C.; Li, H. Controllable Synthesis of Uniform Mesoporous H-Nb 2 O 5 /RGO Nanocomposites for Advanced Lithium Ion Hybrid Supercapacitors. *Journal of Materials Chemistry A* **2019**, *7* (2), 693–703. https://doi.org/10.1039/C8TA10239B.

(128) Sun, C.; Zhang, X.; Li, C.; Wang, K.; Sun, X.; Ma, Y. High-Efficiency Sacrificial Prelithiation of Lithium-Ion Capacitors with Superior Energy-Storage Performance. *Energy Storage Materials* **2020**, *24*, 160–166. https://doi.org/10.1016/j.ensm.2019.08.023.

(129) Hirsch, A. The Era of Carbon Allotropes. *Nature Materials* **2010**, *9* (11), 868–871. https://doi.org/10.1038/nmat2885.

(130) Atkins, P.; Overton, T. *Shriver and Atkins' Inorganic Chemistry*; OUP Oxford, **2010**.

(131) Shu, Z. X.; McMillan, R. S.; Murray, J. J. Electrochemical Intercalation of Lithium into Graphite. *J. Electrochem. Soc.* **1993**, *140* (4), 922. https://doi.org/10.1149/1.2056228.

(132) Roselin, L. S.; Juang, R.-S.; Hsieh, C.-T.; Sagadevan, S.; Umar, A.; Selvin, R.; Hegazy, H. H. Recent Advances and Perspectives of Carbon-Based Nanostructures as

Anode Materials for Li-Ion Batteries. *Materials* **2019**, *12* (8), 1229. https://doi.org/10.3390/ma12081229.

(133) Sonia, F. J.; Aslam, M.; Mukhopadhyay, A. Understanding the Processing-Structure-Performance Relationship of Graphene and Its Variants as Anode Material for Li-Ion Batteries: A Critical Review. *Carbon* **2020**, *156*, 130–165. https://doi.org/10.1016/j.carbon.2019.09.026.

(134) Zhong, S.; Liu, H.; Wei, D.; Hu, J.; Zhang, H.; Hou, H.; Peng, M.; Zhang, G.; Duan, H. Long-Aspect-Ratio N-Rich Carbon Nanotubes as Anode Material for Sodium and Lithium Ion Batteries. *Chemical Engineering Journal* **2020**, *395*, 125054. https://doi.org/10.1016/j.cej.2020.125054.

(135) Yu, K.; Wang, J.; Wang, X.; Liang, J.; Liang, C. Sustainable Application of Biomass By-Products: Corn Straw-Derived Porous Carbon Nanospheres Using as Anode Materials for Lithium Ion Batteries. *Materials Chemistry and Physics* **2020**, *243*, 122644. https://doi.org/10.1016/j.matchemphys.2020.122644.

(136) Czerw, R.; Terrones, M.; Charlier, J. C.; Blase, X.; Foley, B.; Kamalakaran, R.; Grobert, N.; Terrones, H.; Tekleab, D.; Ajayan, P. M.; Blau, W.; Rühle, M.; Carroll, D. L. Identification of Electron Donor States in N-Doped Carbon Nanotubes. *Nano Letters* **2001**, *1* (9), 457–460. https://doi.org/10.1021/nl015549q.

(137) Wang, H.; Zhang, C.; Liu, Z.; Wang, L.; Han, P.; Xu, H.; Zhang, K.; Dong, S.; Yao, J.; Cui, G. Nitrogen-Doped Graphene Nanosheets with Excellent Lithium Storage Properties. *J. Mater. Chem.* **2011**, *21* (14), 5430. https://doi.org/10.1039/c1jm00049g.

(138) Frackowiak, E.; Béguin, F. Carbon Materials for the Electrochemical Storage of Energy in Capacitors. *Carbon* **2001**, *39* (6), 937–950. https://doi.org/10.1016/S0008-6223(00)00183-4.

(139) Yang, Z.; Tian, J.; Yin, Z.; Cui, C.; Qian, W.; Wei, F. Carbon Nanotube- and Graphene-Based Nanomaterials and Applications in High-Voltage Supercapacitor: A Review. *Carbon* **2019**, *141*, 467–480. https://doi.org/10.1016/j.carbon.2018.10.010.

(140) Eftekhari, A. Ordered Mesoporous Materials for Lithium-Ion Batteries. *Microporous and Mesoporous Materials* **2017**, *243*, 355–369. https://doi.org/10.1016/j.micromeso.2017.02.055.

(141) Saikia, D.; Wang, T.-H.; Chou, C.-J.; Fang, J.; Tsai, L.-D.; Kao, H.-M. A Comparative Study of Ordered Mesoporous Carbons with Different Pore Structures as Anode Materials for Lithium-Ion Batteries. *RSC Adv.* **2015**, *5* (53), 42922–42930. https://doi.org/10.1039/C5RA05168A.

(142) Calcagno, G.; Agostini, M.; Xiong, S.; Matic, A.; Palmqvist, A. E. C.; Cavallo, C. Effect of Nitrogen Doping on the Performance of Mesoporous CMK-8 Carbon Anodes for Li-Ion Batteries. *Energies* **2020**, *13* (19), 4998. https://doi.org/10.3390/en13194998.

(143) Béguin, F.; Presser, V.; Balducci, A.; Frackowiak, E. Carbons and Electrolytes for Advanced Supercapacitors. *Advanced Materials* **2014**, *26* (14), 2219–2251. https://doi.org/10.1002/adma.201304137.

(144) Kleitz, F.; Choi, S. H.; Ryoo, R. Cubic Ia3d Large Mesoporous Silica: Synthesis and Replication to Platinum Nanowires, Carbon Nanorods and Carbon Nanotubes. *Chem. Commun.* **2003**, No. 17, 2136–2137. https://doi.org/10.1039/B306504A.

(145) Vix-Guterl, C.; Frackowiak, E.; Jurewicz, K.; Friebe, M.; Parmentier, J.; Béguin, F. Electrochemical Energy Storage in Ordered Porous Carbon Materials. *Carbon* **2005**, *43* (6), 1293–1302. https://doi.org/10.1016/j.carbon.2004.12.028.

(146) Lee, J.; Yoon, S.; Hyeon, T.; Oh, S. M.; Kim, K. B. Synthesis of a New Mesoporous Carbon and Its Application to Electrochemical Double-Layer Capacitors. *Chem. Commun.* **1999**, No. 21, 2177–2178. https://doi.org/10.1039/A906872D.

(147) Li, Q.; Haque, M.; Kuzmenko, V.; Ramani, N.; Lundgren, P.; Smith, A. D.; Enoksson, P. Redox Enhanced Energy Storage in an Aqueous High-Voltage Electrochemical Capacitor with a Potassium Bromide Electrolyte. *Journal of Power Sources* **2017**, *348*, 219–228. https://doi.org/10.1016/j.jpowsour.2017.02.082.

(148) Chun, S.-E.; Evanko, B.; Wang, X.; Vonlanthen, D.; Ji, X.; Stucky, G. D.; Boettcher, S. W. Design of Aqueous Redox-Enhanced Electrochemical Capacitors with High Specific Energies and Slow Self-Discharge. *Nature Communications* **2015**, *6* (1), 7818. https://doi.org/10.1038/ncomms8818.

(149) Tian, B.; Liu, X.; Solovyov, L. A.; Liu, Z.; Yang, H.; Zhang, Z.; Xie, S.; Zhang, F.; Tu, B.; Yu, C.; Terasaki, O.; Zhao, D. Facile Synthesis and Characterization of Novel Mesoporous and Mesorelief Oxides with Gyroidal Structures. *J. Am. Chem. Soc.* **2004**, *126* (3), 865–875. https://doi.org/10.1021/ja037877t.

(150) Kaneda, M.; Tsubakiyama, T.; Carlsson, A.; Sakamoto, Y.; Ohsuna, T.; Terasaki, O.; Joo, S. H.; Ryoo, R. Structural Study of Mesoporous MCM-48 and Carbon Networks Synthesized in the Spaces of MCM-48 by Electron Crystallography. *J. Phys. Chem. B* **2002**, *106* (6), 1256–1266. https://doi.org/10.1021/jp0131875.

(151) Ryoo, R.; Joo, S. H.; Jun, S. Synthesis of Highly Ordered Carbon Molecular Sieves via Template-Mediated Structural Transformation. *J. Phys. Chem. B* **1999**, *103* (37), 7743–7746. https://doi.org/10.1021/jp991673a.

(152) Powell, C. X-Ray Photoelectron Spectroscopy Database XPS,Version 4.1, NIST Standard Reference Database 20, **1989**. https://doi.org/10.18434/T4T88K.

(153) Kapteijn, F.; Moulijn, J. A.; Matzner, S.; Boehm, H.-P. The Development of Nitrogen Functionality in Model Chars during Gasification in CO2 and O2. *Carbon* **1999**, *37* (7), 1143–1150. https://doi.org/10.1016/S0008-6223(98)00312-1.

(154) Figueiredo, J. L.; Pereira, M. F. R. The Role of Surface Chemistry in Catalysis with Carbons. *Catalysis Today* **2010**, *150* (1), 2–7. https://doi.org/10.1016/j.cattod.2009.04.010.

(155) Chang, P. Y.; Bindumadhavan, K.; Doong, R. A. Size Effect of Ordered Mesoporous Carbon Nanospheres for Anodes in Li-Ion Battery. *Nanomaterials* **2015**, *5* (4), 2348–2358. https://doi.org/10.3390/nano5042348.

(156) Wang, H.; Zhang, C.; Liu, Z.; Wang, L.; Han, P.; Xu, H.; Zhang, K.; Dong, S.; Yao, J.; Cui, G. Nitrogen-Doped Graphene Nanosheets with Excellent Lithium Storage Properties. *Journal of Materials Chemistry* **2011**, *21* (14), 5430–5434. https://doi.org/10.1039/c1jm00049g.

(157) Zhang, W. J. Structure and Performance of LiFePO4 Cathode Materials: A Review. *Journal of Power Sources*. Elsevier March 15, 2011, pp 2962–2970. https://doi.org/10.1016/j.jpowsour.2010.11.113.

(158) Analysis of Scale-up Parameters in 3D Silicon-Nanowire Lithium-Battery Anodes. **2020**. https://doi.org/10.1021/acs.nanolett.8b05127.

(159) Chen, L.; Fan, X.; Hu, E.; Ji, X.; Chen, J.; Hou, S.; Deng, T.; Li, J.; Su, D.; Yang, X.; Wang, C. Achieving High Energy Density through Increasing the Output Voltage: A Highly Reversible 5.3 V Battery. *Chem* **2019**, *5* (4), 896–912. https://doi.org/10.1016/j.chempr.2019.02.003.

(160) Takahashi, M.; Nakamura, K.; Jin, J. Study on the Indirect Electrochemical Detection of Ammonium Ion with In Situ Electrogenerated Hypobromous Acid. *Electroanalysis* **2008**, *20* (20), 2205–2211. https://doi.org/10.1002/elan.200804311.

(161) Zhao, Y.; Ding, Y.; Song, J.; Peng, L.; Goodenough, J. B.; Yu, G. A Reversible Br2/Br− Redox Couple in the Aqueous Phase as a High-Performance Catholyte for Alkali-Ion Batteries. *Energy Environ. Sci.* **2014**, *7* (6), 1990–1995. https://doi.org/10.1039/C4EE00407H.

(162) Xiao, L.; Wildgoose, G. G.; Compton, R. G. Investigating the Voltammetric Reduction of Methylviologen at Gold and Carbon Based Electrode Materials. Evidence for a Surface Bound Adsorption Mechanism Leading to Electrode 'Protection' Using Multi-Walled Carbon Nanotubes. *New J. Chem.* **2008**, *32* (9), 1628–1633. https://doi.org/10.1039/B804842H.

(163) Bird, C. L.; Kuhn, A. T. Electrochemistry of the Viologens. *Chem. Soc. Rev.* **1981**, *10* (1), 49–82. https://doi.org/10.1039/CS9811000049.